A dissertation submitted for the degree of Master of Science

School of Physics

University of Witwatersrand

Braamfontein, Johannesburg

The Variability of Cosmic Methanol Masers in Massive Star Forming Regions

Author: Maswanganye Jabulani P.[1]

Supervisors: Booth Roy S.[2]

and

Gaylard Michael J.[1]

October 2012

[1]Hartebeesthoek Radio Astronomy Observatory, P O Box 443, Krugersdorp 1740, South Africa.
[2]SKA/MeerKAT, 3rd floor the Park, Park road, Pinelands, Cape town, South Africa

Declaration

I declare that this Dissertation is my own, unaided work. It is being submitted for the Degree of Master of Science in the University of the Witwatersrand, Johannesburg. It has not been submitted for any degree or examination in any other university.

_____

(Signature of candidate)

_____ day of _____ 20____ in _____

Acknowledgement

The work presented in this Master thesis was made possible by some individuals' time dedicated in advancing my understanding and by two institutions, and I would like to dedicate this chapter to all the contributors both financially and academically.

- I would like to thanks my supervisor Prof. Roy Booth. He accepted me as his student and had given me the time to do what I enjoy most. Thank you for your time in shaping my future. I highly appreciate it and it was a wonderful experience.

- I am very thankful of Dr. Michael (Mike) Gaylard (co-supervisor) at Hartebeesthoek Radio Astronomy Observatory (HartRAO). He guided me through and helped me to understand most of the concept better. He reasoned with me, he shared his skills, intellectual, knowledge, etc. He gave me exposure by sending me to the conferences. He helped me a lot even in writing this thesis.

- My thanks also goes to Dr. Sharmila Goedhart. She helped me a lot in time series analysis methods. She helped me even in the python script which was used for time series analysis.

- My gratitude also goes to Dr. Jonathan Quick and Mr. Ronnie Myataza. They were very helpful in explaining the procedure for the receiver calibration and laboratory radiometer testing. Ronnie also helped me in sketching the blueprint of the 2.5-cm and 4.5-cm receivers.

- I would not forget the effort of my colleague Ms. Sunelle Otto. She helped me with some of the proof readings and with ideas. Thanks you very much.

It was a wonderful experience working with her.

- I am very thankful for a thoroughly proof reading of my thesis to Marion West and Ludwig Schwardt. Marion questioned where she thought I was not clear enough and she shared her knowledge with me. She helped me a lot and I appreciate every second she had spent on my thesis.

- Thanks to National Astrophysics and Space Science Programme (NASSP). They helped me financially. It was through NASSP that I get to know about methanol masers. Thanks to Nicky Walker, Peter Dunsby and the rest of the NASSP committee.

- HartRAO hosted my project and added a top up to my bursary. Many thanks to all the staff. They made me feel at home and every one helped a lot. I also want to thank National Research Foundation (NRF) for funding HartRAO to fix the bearing in the 26-m telescope. All data were collected with the 26-m telescope at HartRAO. The staff helped a lot in running the telescope, finance office processing purchases for tools to run the telescope. They did a very good job.

- I would like to thank my parents (Mr. S. M. Maswanganye and Mrs. M. N. Maswanganyi), my brothers and Ms. T. Netshifhefhe for boosting my confidence by believing in me.

- Thanks to God for creating this complex universe so that I can explore. I found joy in exploring his wonders.

Abstract

In this thesis, the background and technical theory of the receivers are discussed. Methods used to search for periods, correlations, and delays in the time series of class II methanol masers at 6668 MHz and 12178 MHz are presented together with the observed variability of these sources. Background theory is given on, the processes by which massive stars are formed. The theory of astronomical masers and methanol maser excitation is given in detail.

The receiver testing and observation technique chapters describe: the results and methods used to calibrate the two receivers, namely 2.5-cm and 4.5-cm, with central frequencies of 6668 MHz and 12178 MHz respectively, as well as data capture methods for spectroscopic observations. The laboratory square law detector or radiometer was also calibrated to ensure that the noise diode temperature was accurately determined. There is 8.3 per cent deviation from an ideal square law detector.

The time series and spectra for one methanol source, G351.42+0.64 which serves as a control source at 6668 MHz and 12178 MHz, one irregularly varying methanol source G351.78-0.54 at 6668 MHz, seven known quasi-periodic and periodic sources (G9.62+0.20E, G12.89+0.49, G188.95+0.89 and G328.24-0.55, at both 6668 MHz and 12178 MHz, and G331.13-0.24, G338.93-0.06, and G339.62-0.12, at 6668 MHz), and seven new methanol maser source regions (G0.092+0.663, G6.189-0.358, G8.832-0.028, G8.872-0.493, G348.617-1.162, G351.688+0.171 and G358.460-0.391, at both 6668 MHz and 12178 MHz) are shown and discussed. The seven new sources were from the 6668-MHz Methanol Multi-Beam (MMB) survey Catalogues I and II. Pe-

riods were searched for using the Lomb-Scargle and epoch-folding methods. The quasi-periodic and periodic sources show diverse waveforms and diverse periods between 29 and 511 days. From the seven new methanol maser sources, G8.872-0.493 (76 day period) and G358.460-0.391 (187 day period) both at 6668 MHz, were found to be variable and they are possible new candidates for the periodic or quasi-periodic group of sources.

The Colliding Wind Binary (CWB) model is proposed by van der Walt (2011) as the source of the observed periodic variability in these regions. The properties of the binary systems using the 29 and 511 day period are discussed as well as the common features in the time series, such as long-term variations and flares. The source of the periodicities has not been finally determined but the foundation has been laid.

Contents

List of Figures

List of Tables

Chapter 1

Introduction

1.1 Background

MASER is an acronym for **M**icrowave **A**mplification by **S**timulated **E**mission of **R**adiation. There are a small number of astronomical (naturally occurring) maser species and among them are methanol masers. The two brightest methanol maser emission lines (12178-MHz and 6668-MHz) are found in massive star forming regions and serve as a useful tool for probing these environments. The 12178-MHz line was found by Batrla et al. (1987) and the 6668-MHz line was discovered by Menten (1991).

Methanol is formed in the molecular cloud via grain surface reactions (Das et al., 2008). In this process: hydrogen (H), carbon monoxide (CO) and oxygen (O) are accreted onto the surface of the grain. These species will react with one another based on their electro-negativity and electron affinity. A methanol molecule can be formed in the process ($H + H_3CO \longrightarrow CH_3OH$). Studying methanol maser lines at 6668-MHz and 12178-MHz is an indirect way of studying the dynamics of these massive star forming regions. Probing the interior of these molecular clouds directly is hard due to the high optical depth at optical wavelengths, resulting from dust which absorbs most of the radiation emitted by the young stellar object.

1.2 Motivation

Goedhart et al. (2003) reported periodic flares in masers associated with G9.62+0.20E. Goedhart et al. (2004) at Hartebeesthoek Radio Astronomy Observatory (HartRAO) monitored a sample of 54 methanol maser sources at 6668-MHz. These were found in massive star forming regions and it was found that seven of these showed regular (periodic) variability. Since then, HartRAO has continued monitoring these sources to try to explain such behaviour.

There is a two year gap in the monitoring programme due to the 26-m HartRAO radio telescope bearing having failed in 2008. After repairing the bearing and the receivers in 2010, the monitoring programme was resumed. Seven new methanol emission regions from the 6668-MHz Methanol Multi-Beam (MMB) survey catalogue I (Caswell et al., 2010) and catalogue II (Green et al., 2010) were considered for a new monitoring programme to search for more periodic masers.

There are a lot of questions to be answered in this field, but in this thesis we want to set up a foundation for study of the variability of cosmic methanol masers in massive star forming regions to see whether these periodic (quasi-periodic) masers evolve and if so, how they evolve. New sources are considered to try to find out how many different waveforms can be observed. We also want to see whether there are other periodic sources (e.g. Szymczak et al. (2011) found a new periodic source). It might not be possible to find conclusive evidence of periodicity because periods can be of the order of hundreds of days.

1.3 Overview

The thesis comprises seven chapters, including the introduction.

In chapter 2, the star formation processes, formation of a multiple star system, the definition of a maser, methanol spectroscopy and selected methanol maser sources (irregular, periodic and quasi-periodic) are discussed.

In chapter 3, the method used to calibrate the noise diode of the 2.5-cm receiver, 4.5-cm receiver and laboratory radiometer used for receiver testing, and the data collection techniques and calibration technique are discussed. The results for each receiver noise diode calibration, radiometer calibration and telescope calibration are shown and discussed.

In chapter 4, four time series analysis methods are discussed. Three of these methods are used to determine and test the significance of the period in a time series - (i) the Lomb-Scargle, (ii) Phase Dispersion Minimisation and (iii) epoch-folding methods. The fourth method is used to study the correlations and phase lags (time delays) between two time series.

In chapter 5, the results for the control source, irregularly varying source, periodic or quasi-periodic sources, and seven new methanol sources are shown.

Chapter 6 discusses the results for the irregularly varying sources, periodic or quasi-periodic sources, and seven new methanol maser sources.

In chapter 7, the results and discussions are summarised and the future prospects are presented.

Chapter 2

Star formation and maser theory

2.1 Introduction

This chapter gives the background theory about massive star forming processes, competing models on the possibility of forming a multiple star system, and astronomical maser and methanol maser sources which were considered for the investigation of the observed variability.

2.2 Star formation processes

High mass star formation occurs in four stages (Zinnecker & Yorke, 2007). First, a giant molecular cloud forms dense cold molecular cores or filaments due to gravo-turbulence in the **compression stage**. The second stage is a non-homologous **collapse** of the core into an optically thick, pressure-supported protostellar embryo. The non-homologous collapse occurs when the density distribution in the molecular cloud is uneven. Shu (1992) gives the density ρ of the inner region of the molecular cloud to be $\rho \propto r^{-\frac{3}{2}}$ and $\rho \propto r^{-2}$ for the outer region in the non-homologous collapse. During the collapse, the inner region will be in free fall whereas the outer region will be almost static. Third, the giant molecular cloud material falls into

the protostellar embryo undergoing **Accretion via a disk**. Fourth: In **disruption** phase, the interaction between the jets, HII gas pressure, and radiation pressure disrupts the clouds (Murray et al., 2010). Below, the details of the collapsing and accretion phase are given.

After the compression stage, a sufficiently perturbed giant molecular cloud will collapse. This collapse occurs in isothermal conditions which are best described by the Bonner-Ebert sphere (Foster, 1994). The perturbation could be caused by the shock wave from a supernova explosion, which results from star death or from star birth, or from stellar winds. This will result in a supersonic flow in the interior of the giant molecular cloud. As the supersonic flow propagates in the inter-cloud medium there will be a strong density perturbation, which is due to the fact that the inter-cloud medium is highly compressible (Mac Low & Klessen, 2004). The giant molecular cloud contracts under gravity and the turbulent flow, together with the magnetic field, generates the outward pressure. As clumps collapse, the radiated energy dissociates H_2 instead of increasing the temperature of the dense core. The magnetic field in the core produce Lorentz force which is exerted on the ions. The ions are pushed out of the high gas density region. The magnetic field is dragged out together with the ions. This is called *ion-neutral or ambipolar diffusion* (Nunez, 2006; Pudritz, 2002). The thermal pressure can be ignored because the molecular cloud is cold. Clumps will self-gravitate to form a protostar.

Due to the protostar's high density, the surrounding clumps will fall into the protostar. The clumps with large angular momentum will spiral into the protostar, resulting in the formation of a circumstellar accretion disk. This process serves as an angular momentum reduction mechanism for the infalling clumps. The proto-

star's internal thermal pressure will increase during the accretion and force its way out via the rotational axis, this is called 'bipolar molecular outflow'. The protostar will then follow the Pre-Main Sequence (PMS) path for a high mass star in the Hertzsprung-Russell (HR) diagram (Prialnik, 2000). In the PMS, the protostar will be burning hydrogen and still accreting its envelope. The protostar will eventually enter the Zero Age Main Sequence (ZAMS) on the HR diagram, where the interactions of jets, HII gas pressure and radiation pressure destroy the accretion disk (Zinnecker & Yorke, 2007).

2.2.1 Star cluster formation

Perhaps the observed regular variability of class II methanol masers can be explained by binary or multiple star systems. It was suggested by van der Walt (2011) that the colliding winds from a binary system could explain the observed periodic flare from one of the methanol maser sources called G9.62+0.20E.

In most cases, stars are found in groups. Kraus (2010) listed four possible mechanisms in which a binary or multiple star system could be formed. They are:

- tidal capture in a dense stellar cluster,
- splitting of a protostar to form a binary companion,
- formation of a binary companion from a circumstellar accretion disk, or
- fragmentation during core formation.

Shu et al. (1987) suggest fragmentation of the giant molecular cloud by shock compression or catastrophic cooling (Woodward, 1953) as another possible way of

forming a multiple star system. The shock front initiates the implosion of a cloud so that it collapses to form two or more dense cores. Each of these dense cores will evolve to form a star.

Press & Teukolsky (1977) give detailed calculations of the two-tidal capture mechanism of Fabian et al. (1975). In this mechanism, the stars close together are captured by tidal forces. This formation mechanism does not concern us much because we are interested in the early stages of massive star formation.

The splitting of a protostar or young stellar object to form a binary companion falls within the region of our interest. In this mechanism, if the core has enough angular momentum it experiences stress. The amount of angular momentum will determine the future of the core. For small angular momenta, the shear force will just deform the core. For stronger angular momenta, this will result in the formation of a tri-axial bar shape, which could be further split into multi-system cores provided that it has enough angular momentum (Kraus, 2010). These multi-system cores can accrete more matter to become a binary or multiple star system. One of the big challenges with this mechanism is that particles with high angular momentum and low total mass would move to the edge of the bar. This would result in a quick reduction of angular momentum in the tri-axial bar before it splits into dense multiple cores (Boss, 1988). Each of the separated dense cores would accrete to form a star which would be part of a multiple star system.

In the splitting of a circumstellar accretion disk to form a companion star, the rate of infall onto a circumstellar accretion disk and the transfer rate of matter from the accretion disk to the protostar are unbalanced. This causes instability in the disk. The unstable disk splits to form a dense core, which could also form a star.

During the formation of the core, there are two possible collapse mechanisms, namely homologous (when all parts of the molecular cloud collapse at the same rate due to the uniform density distribution) and non-homologous (Kraus, 2010). Homologous collapse occurs when the thermal energy is less than the gravitational energy. Non-homologous collapse occurs when the core is rotating slowly which results in a significant density difference between the central core and the edge of the core. The difference in density results in a split of the core to form a primary star and its companion.

2.3 Astronomical masers

In order for astronomical masers to form, population inversion and velocity coherence are required. Population inversion means that the upper energy level must be more populated than the lower energy level. Velocity coherence means that the Doppler shift difference along the line of sight is small.

Before the description of a maser, it vital to describe how the particles in the energy levels are distributed in thermodynamic equilibrium. These particles are described by the Boltzmann equation of thermodynamic equilibrium (Osterbrock & Ferland, 2006; Rybicki & Lightman, 2004).

To better understand a maser, a two-energy-level population model (Figure 2.1) will be used. In Figure 2.1, the particles can be moved from the upper (lower) to the lower (upper) energy level. This is based on the principle of detailed balance which states that *for every microscopic process there is a reverse counterpart and the rate of these processes takes place in such a way that if they were the only process*

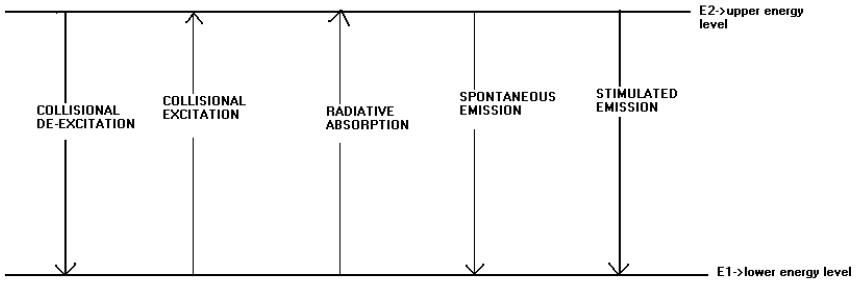

Figure 2.1: The diagram shows two energy levels for a system. There are processes which can populate and de-populate the energy levels. These processes are either collisional or radiative.

in the system, then the resulting population distribution would be in thermodynamic equilibrium (Elitzur, 1992).

There are three possible outcome which can occur when matter interact with radiation; absorption, represented by Einstein B-coefficient B_{ij}. The subscript ij means the transition is from i energy level to j, spontaneous emission, represented by *Einstein A-coefficient* A_{ij}, and Induced or stimulated emission, which was found by Einstein (1917) (ter Haar, 1967, English version) and represented by the Einstein B-coefficient given by B_{ji}. When the principle of detail balance and the Boltzmann equation of thermodynamic equilibrium assumption are used in the two-energy-level population model, the Einstein coefficients related by

$$A_{ji} = \frac{2h\nu^3 B_{ji}}{c^2}; B_{ij} = \frac{g_j B_{ji}}{g_i} \tag{2.1}$$

where c is the speed of light in the vacuum, ν is the frequency and g_i is the statistical weight. Equation 2.1 shows that Einstein's coefficients are independent of the thermal equilibrium because they are temperature independent but they are dependent on the microscopic quantities of the system.

In our two-energy-level model, the statistical weight for all levels will be considered to be the same ($g_1 = g_2 = g$) and the dumping rate will also be the same ($\Gamma_1 = \Gamma_2 = \Gamma$). The dumping term arises in the system due to the fact that particles can decay to the non-masing levels. So the resulting set of steady state equations will be

$$0 = p_{1\nu} - \Gamma n_{1\nu} + B_{12\nu} J_\nu n_{2\nu} - B_{12\nu} J_\nu n_{1\nu} + A_{21\nu} n_{2\nu} - n_{1\nu} C_{12} + n_{2\nu} C_{21} \quad (2.2)$$

and

$$0 = p_{2\nu} - \Gamma n_{2\nu} - B_{12\nu} J_\nu n_{2\nu} + B_{12\nu} J_\nu n_{1\nu} - A_{21\nu} n_{2\nu} - n_{2\nu} C_{21} + n_{1\nu} C_{12}. \quad (2.3)$$

In Equation 2.2 and Equation 2.3, $J_\nu = \frac{1}{4\pi} \int I_\nu d\Omega$ is an angle-averaged intensity which is the strength of the radiation field, p_i is the pumping rate, n_i is the population per sub-level and C_{ij} is the collision rate (defined by the product of the overall system density number and collisional rate coefficient).

If Equation 2.3 is subtracted from Equation 2.2, the population difference $\Delta n_\nu = n_{2\nu} - n_{1\nu}$, can be determined and as

$$\begin{aligned} \Delta n_\nu &= \frac{\Delta p}{\Gamma + 2B_{21} J_\nu}, \\ \Delta n_\nu &= \frac{\Delta n_o}{1 + \frac{J_\nu}{J_s}} \phi(\nu), \end{aligned} \quad (2.4)$$

where $\Delta n_o = \frac{p_2 - p_1}{\Gamma}$, $\phi(\nu)$ is the line profile of the emission, and the *saturation intensity* $J_s = \frac{\Gamma}{2B_{21}}$. Elitzur (1992) has shown that the detailed behaviour of masers is still valid even if collisional terms and spontaneous decay terms are neglected. The

collisional term is ignored, based on the fact that the radiated energy ($\Delta E = h\nu$) during masing is far less than the energy associated with the kinetic temperature (T_k) of the system. Another factor is that masers cannot occur in high density regions, as this implies that the collision rate will be less than the decay rate in the energy level. The spontaneous decay can be ignored because it occurs at a much lower rate when compared to the decay rate Γ, which represents energy losses to energy levels other than maser energy levels. So neglecting the collision and spontaneous decay terms, the population inversion efficiency is

$$\eta = \frac{p_2 - p_1}{p_1 + p_2}. \tag{2.5}$$

In Equations 2.5 and 2.4, $p_2 > p_1$ is a non-thermal population inversion ($n_2 > n_1$) and maser action can occur ($\eta > 0$), but when $p_2 \leq p_1$ (*anti-inversion*) maser action cannot occur ($\eta \leq 0$) because there will be no population inversion.

The pumping mechanism in a maser excites the system to a higher state which then cascades down to the masing level. The pumping mechanism is important in order for the maser to occur more than once. There are two known possible pumping mechanisms for masers, namely radiative and collisional pumping. The pumping rate terms are $p_{1\nu}$ and $p_{2\nu}$, in Equations 2.2 and 2.3 respectively.

Another factor in an astronomical maser is radiation amplification. The emission of radiation is studied using quantum mechanics but the radiation transfer from a source is studied using electromagnetism. So the radiated photons are carried through the medium by the mechanism called radiative transfer. The rate of change of the emitted intensity I_ν over the path which the radiation uses is defined by the radiation source (S_ν) minus the radiation intensity. The source function is defined

by the ratio of the emissivity coefficient (ξ_ν) and the absorption coefficient (κ_ν). This is a *radiative transfer equation*. The equation for the absorption coefficient is given by Elitzur (1992) and also by Lo (2005) as

$$\kappa_\nu = \frac{h\nu}{4\pi} n_1 B_{12} \left(1 - \frac{n_2/g_2}{n_1/g_1}\right) \phi(\nu). \tag{2.6}$$

Masers occur when the absorption coefficient is negative, which implies that as the radiation moves through the cloud or media it will be amplified. This occurs when the medium is not in the thermal equilibrium which is when $\left(1 - \frac{n_2/g_2}{n_1/g_1}\right) > 1$, $\implies \exp\left(-\frac{h\nu}{kT}\right) > 1$. In a molecular cloud, a long path length L along which the stimulation radiation has to travel is required. The radiation is amplified by a factor of $\exp\left(-\int \kappa_\nu dL\right)$ (Lo, 2005). An example of where masers can be formed is the region of molecular gas near the star, where this region is not in thermal equilibrium. In this region, the density of the gas is below the critical density for the collisional de-excitation and this results in the radiative decay of the excitation state which causes the population inversion and masers to form (Lo, 2005). When $\frac{J_\nu}{J_s} \ll 1$, the maser population difference Δn_ν does not interact with maser radiation and it is called an *unsaturated* maser. In the unsaturated maser case, particles are pumped with rate p and leaves with rate Γ before interacting with radiation (Elitzur, 1992). The unsaturated masing implies exponential amplification as explained above, so the spectral and spatial Full Width Half Maximum (FWHM) becomes narrower; hence, masers are very bright and very compact. On the other hand, the saturated maser occurs when $\frac{J_\nu}{J_s} \gg 1$, where the maser radiations will affect the population inversion (see equations 2.4 and 2.5). This will decrease maser growth (the absorption coefficient will decrease too), increase photon production rate, re-broaden the

line profile and FWHM will get more narrower (Elitzur, 1992).

The overall population of the maser system is defined by n_ν and $n_\nu = n\phi(\nu)$, with $\phi(\nu)$ being the line profile of the emission. The line profile holds information about broadening or narrowing of the emission (see Section 4.5 in: Elitzur, 1992).

2.4 Methanol maser excitation

The structure of the methanol molecule is shown Figure 2.2a. The hydroxyl group is asymmetric to the methyl group. There is a mutual interaction between these two groups which hinders the rotation of methyl relative to hydroxyl. This results in torsional oscillation due to the methyl and hydroxyl bond, and it produces angular momentum about the internal rotation axis defined by the methyl group (de Buizer, 2000). This angular momentum is strongly coupled with the overall or total angular momentum to produce the two torsional symmetry states of the methanol molecule, namely A-type and E-type symmetry. Their main difference is the alignment of the nuclear spin (Cragg et al., 2005). The quantum mechanics selection rule for transitions between two energy states requires the conservation of symmetry. This means that transitions between E-type and A-type methanol symmetry are forbidden and only E-type to E-type and A-type to A-type transitions are allowed.

Molecules have rotational, vibrational and electronic eigenstates which are characterised by quantum numbers. These quantum numbers are the total angular momentum quantum number ($\vec{L}$), the total angular spin momentum quantum number ($\vec{S}$), the overall total angular momentum quantum number ($\vec{J}$) and the K-quantum number, which is the projection of total angular momentum onto the nuclear symme-

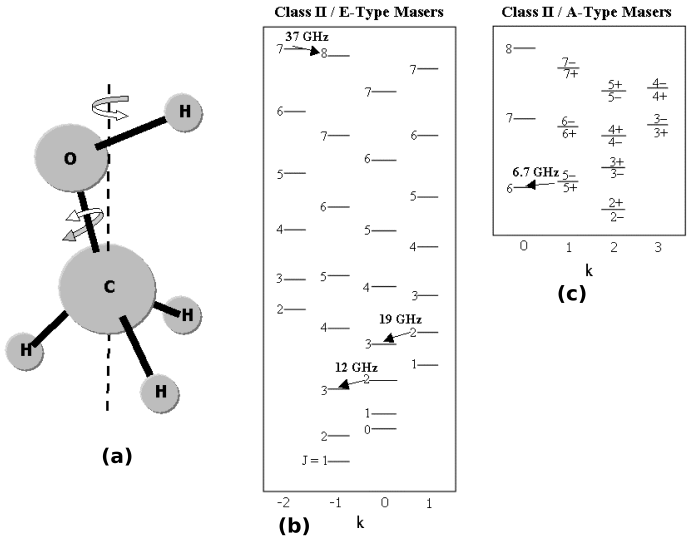

Figure 2.2: (a): Model of the methanol maser with the dashed line being the axis of symmetry. The double headed arrow in the methanol molecular structure shows the hindered internal rotation by the OH group. (b) and (c): Energy levels of A-type and E-type class II methanol transitions. The + and − are used to show the split in the energy levels (de Buizer, 2000).

try axis. The quantum number which characterises the torsional vibrational energy state is v. The rotational eigenstate is characterised by $\vec{J_K}$. $\vec{J}$ is found by adding $\vec{L}$ and $\vec{S}$ using the **LS**-coupling scheme ($\vec{J} = \vec{L} + \vec{S}$) (Foot, 2005). The energy state of the molecule can also be described by the K quantum number which is not a strict quantum number, but it can be considered as a quantum number due to asymmetry and internal rotation of the methanol molecule (Cragg et al., 2005). The A-type symmetry methanol has torsional degeneracy which splits $K > 0$ quantum numbers into a pair of degenerate energy levels labelled by A^+ and A^-, but the E-type symmetry has double degeneracy (de Buizer, 2000). As shown in Figure 2.2 (b) and (c), the values of the K quantum numbers for E-type symmetry are both negative and positive in the methanol energy level diagram. The energy levels for A-type methanol occur for the non-negative integers in the K quantum numbers. The tor-

sional degeneracy splitting only occurs when the K quantum number is positive. All the transitions in an atom or a molecule are governed by the quantum mechanics selection rules.

There are two classes of methanol masers, namely class I (MMI) and Class II (MMII). These classes are distinguished by their transitions and surrounding environments. MMII appears to be projected on ultra-compact ionised hydrogen (UCHII) regions in massive star forming regions. They serve as an indirect way of studying the dynamics of massive star forming regions. On the other hand, MMI are off-set from the UCHII regions and they are often associated with hydroxyl (OH) masers and water vapour (H_2O) masers (Menten, 1991).

For the A-type state, ΔK is positive and an example is the 6668-MHz MMII emission line which is between the 5_1 and 6_0 levels. For the E-type state, ΔK is negative, and the 12178-MHz MMII emission line is an example. This is the transition between 2_0 and 3_{-1} levels (Cragg et al., 2005). In the above example, the numbers in the radiative transition states are total angular momentum and the subscript is the K quantum number, which has been defined as the projection of the total angular momentum ($\vec{J_k}$). These radiative transitions can be simplified in this form $5_1 - 6_0$ A^+ at 6668-MHz and $2_0 - 3_{-1}$ E at 12178-MHz.

The population inversion will only occur if the spontaneous decay to the masing level is faster than the decay rate of the maser level, or the spontaneous decay from the maser level is slower than the decay to the maser level. For an example, see Figure 2.1. The rate at which particles move from the n_2 population should be less than the rate at which particle move to n_2. It implies that the end result will be that $n_2 > n_1$ (population inversion). The A_{ij} coefficient of spontaneous decay is directly

proportional to the cube of the frequency ($A_{ij} \propto \nu^3$): see Equation 2.1 in Section 2.3 (Elitzur, 1992). The spontaneous decay is strong at high frequencies and weak at low frequencies. By studying the Einstein coefficient, Cragg et al. (1992) came to the conclusion that for the E-type methanol, K = 2 is favoured over K = 1 and 3, and K = -1 is favoured over K = 0 and 3. For the A-type, K=0 is favoured over K = 1, and K = 1 and 3 are favoured over K = 3. Our interest is mostly in the pumping mechanism for MMII and to be more direct, the $2_0 - 3_{-1}$ E and $5_1 - 6_0$ A^+ transitions which form maser emission lines.

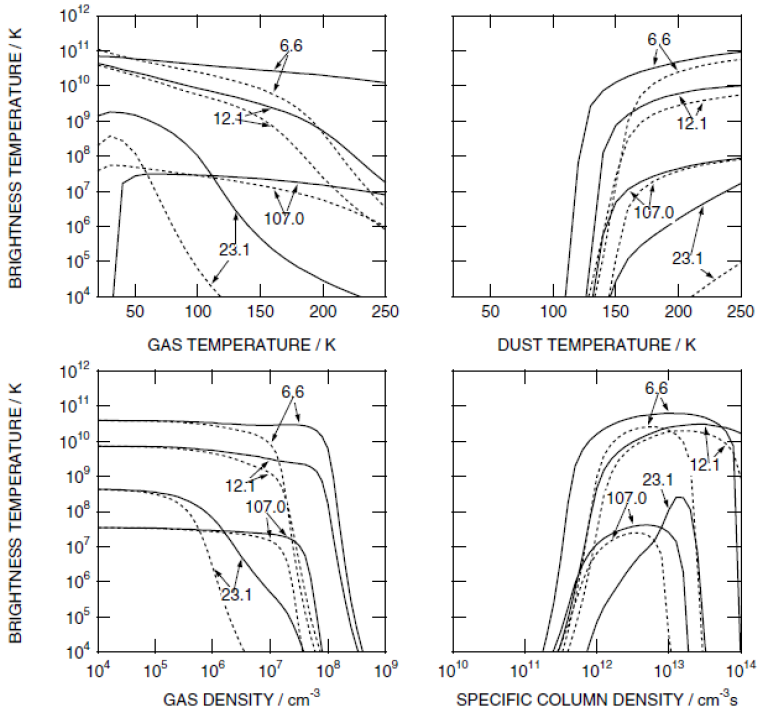

Figure 2.3: The results for the brightness temperature for the four class II methanol masers (6668-MHz, 12178-MHz, 23121-MHz and 107013-MHz), modelled by Cragg et al. (2005) with the new collision data. The T_k, T_d, n_H and $\frac{N_M}{\Delta V}$ were fixed at 150 K, 175 K, 10^7 cm^{-3} and $10^{12.2}$ cm^{-3}s respectively. The solid line is for the new Pottage et al. (2001, 2002, 2004a,b) collision data, and the dashed line is for the collision rate coefficients determined by the propensity rule (Fano, 1985), which was based on the double resonance experiments by Lees & Haque (1974). The energy levels used were up to J = 18 and v_t = 3.

Cragg et al. (1992) have shown that MMI are collisionally pumped while MMII are radiatively pumped, where the collisional excitation is important for keeping the system in quasi-equilibrium from the radiation field. This argument follows the principle of detailed balance. MMII are likely to be found in the moderate dense ($10^5 < n_H < 10^{8.3}$ cm^{-3}) but cooler (< 100 K) environments and they are pumped by the warm infrared dust (> 100 K) Cragg et al. (2002). For the $2_0 - 3_{-1}$ E maser emission line, the system is radiatively pumped to a higher energy level, then decays spontaneously. The 3_{-1} energy level is favoured over 2_0 during the spontaneous decay, making it more populated than 2_0, but the loss rate for 3_{-1} is higher than 2_0, therefore there will be a population inversion between 2_0 and 3_{-1} E-type states. If a photon stimulates this population inversion, maser radiation will occur as shown in Figure 2.2(c). The formation process for the $5_1 - 6_0$ A^+ maser line is similar to that for the $2_0 - 3_{-1}$ E maser line.

Figure 2.3 show the results from modelling four class II methanol masers (6668-MHz, 12178-MHz, 23121-MHz and 107013-MHz). The dust temperature (T_d), the kinetic temperature (T_k), the specific column density ($\frac{N_M}{\Delta V}$), which is the ratio of the column density of A- or E-species methanol tangential to the line of sight (N_M) and the line width (ΔV), and the gas density (n_H) were kept constant in the model. Cragg et al. (2005) found that at low gas density (10^4 cm^{-3}) both collisional models are irrelevant and masers are formed by radiative effects. At high density (10^9 cm^{-3}), collisions are very important in balancing the effect of the pumping mechanism and all masers are rapidly cooled down.

The 6668-MHz and 12178-MHz emission lines show weak or strong correlation from one condition to another (see Figure 2.3). This shows that these two emission

lines are found in slightly different conditions. For an example, at high brightness temperature ($> 10^{10}$ K) and low gas temperature (< 100 K), there is a strong correlation. For the high gas temperature (> 100 K) and a lower brightness temperature ($< 10^{10}$ K), there is a weaker correlation between the 6668-MHz and 12178-MHz emission lines (see Figure 2.3). The rapid cooling of these two emission lines are also observed at different conditions. For an example, 6668-MHz line cools rapidly between 10^{13} and 10^{14} $cm^{-13}.s^{-1}$ specific column density, but 12178-MHz emission line quenches at higher specific column density ($> 10^{14}$).

2.5 Monitored methanol maser regions

Methanol masers show different types of variability. Goedhart et al. (2003) monitored 54 methanol maser sources with the 26-m HartRAO telescope, and noticed that one of the methanol maser regions shows periodic flares. Later it was shown that seven sources were periodic or quasi-periodic (Goedhart et al., 2004).

The 26-m HartRAO radio telescope bearing failed in 2008 and the telescope was recommissioned after it was repaired in 2010. The monitoring programme was resumed for some of the periodic, quasi-periodic and episodic methanol sources. Seven new methanol maser source regions were added as a new monitoring programme. Our samples of methanol maser sources for single dish radio astronomy monitoring programmes were arranged in four groups.

The first group only has one source and it is a control source, G351.42+0.64. A map of this region with maser spot maps (OH masers of Forster & Caswell (1989) and Gaume & Mutel (1987), H_2O masers of Forster & Caswell (1989) and CH_3OH

masers), the ultra-compact ionised hydrogen region, mid-infrared sources, and the 6668-MHz radio continuum image (Caswell, 1997) was given by de Buizer et al. (2000). The time series of the masers show small irregular variations and it is a bright source, so it can be observed in a short time (Goedhart et al., 2009). It is important to check if the determined Point Source Sensitivity (PSS) from the continuum calibrators is correct for spectroscopy. An incorrect PSS value will result in artificial variations in the time series and the masers in this source provide a good continuity check.

The second group also has one source, G351.78-0.54. This source has shown strong random variations in both hydroxyl (1665 MHz) and methanol (6668 MHz) masers (Macleod & Gaylard, 1996). Macleod & Gaylard (1996) attempted to explain the observed variability as being caused by either the variations in the pumping mechanism which could be non-thermal radio emission, irregularly varying ionised jets and dense, ionised stellar winds or fluctuation in the masing gas.

The third group of masers comprises the seven sources identified by Goedhart et al. (2004, 2009, 2003) as periodic or quasi-periodic sources. These sources are G9.62+0.20E, G12.89+0.49, G188.95+0.89, G328.24-0.55, G331.13-0.24, G338.93-0.06 and G339.62-0.12.

- G9.62+0.20 is a complex massive star forming region. It has several different types of HII regions and Garay et al. (1993) labelled them from A to E according to their increase in compactness. The methanol masing region is found in front of the E region (Goedhart et al., 2005). The time series at both 6668 MHz and 12178 MHz show a 246 day period (Goedhart et al., 2003).

- G12.89+0.49 is a massive star forming region found in the Carina Sagittar-

ius spiral arm and it shows strong emission in water vapour, hydroxyl and methanol masers (Xu et al., 2011). It has a period of 29.5 days for both 6668 MHz and 12178 MHz, which is the shortest known period in periodic methanol maser sources (Goedhart et al., 2009).

- G188.95+0.89 is considered to be a complex massive star forming region. Minier et al. (2005) made a multi-wavelength study of this region. It was found to be projected near Sh 2-247 (which is part of the Gem OB1 complex molecular cloud complex). It has two regions, namely G188.95-MM1 (emits from mid-infrared to mm) and G188.95-MM2 (which shows strong sub-mm and mm emission). Studies of the spectral energy distribution (SED) of this region gave a mass limit and luminosity limit for the source. The 6668-MHz and 12178-MHz maser lines have a period of 416 days (Goedhart et al., 2004).

- The G328.24-0.55 methanol source region shows two groups of maser spots both at 12178 MHz and 6668 MHz. It has a radio continuum source with an integrated flux density of 27.7 mJy (Phillips et al., 1998). Norris et al. (1993) found that these maser spots are not linearly distributed and it was suggested that these maser spot groups are on the opposite sides of the UCHII region (which may be on the opposite edges of the circumstellar accretion disc). Another possibility is that each group could have its own star, meaning that it could be a binary system. Masers were considered to be moderately variable with a 216 day period (Goedhart et al., 2004).

- The G331.13-0.24 interferometric maser spot maps show a linear morphology but with an additional weak maser some distance away (Phillips et al., 1998). It was also suggested that this region could be a multiple star forming region.

The maser line at 6668 MHz show quasi-periodic variations - some time series have a 572 day period and some a 472 day period (Goedhart et al., 2004).

- The masers in G338.93-0.06 show strong periodicity at 6668 MHz with a 132 day period (Goedhart et al., 2004).

- G339.62-0.12 interferometric maser spot maps show two groups (Walsh et al., 1998). This source was monitored at 6668-MHz. The time series for the spread out maser spot group has shown irregular variations and the other group showed regularly varying behaviour with a 202 day period (Goedhart et al., 2004).

The fourth group comprised seven of the brightest methanol maser source regions selected from the 6668-MHz Methanol Multi-Beam (MMB) survey Catalogue I (Caswell et al., 2010) and Catalogue II (Green et al., 2010). These emission regions are G0.092+0.663, G6.189-0.358, G8.832-0.028, G8.872-0.493, G348.617-1.162, G351.688+0.171 and G358.460-0.391. These source regions have been previously monitored in two epochs, first with the 64-m Parkes radio telescope, followed by the Australia Telescope Compact Array (ATCA) for accurate position measurements.

2.6 Possible explanation for periodic behaviour

In an attempt to explain the source of the periodic variability, van der Walt (2011) proposed a model which could reproduce the periodic flares seen in G9.62+0.20E and the periodic variations of G188.95+0.89. The theory for the model is illustrated in Figure 2.4.

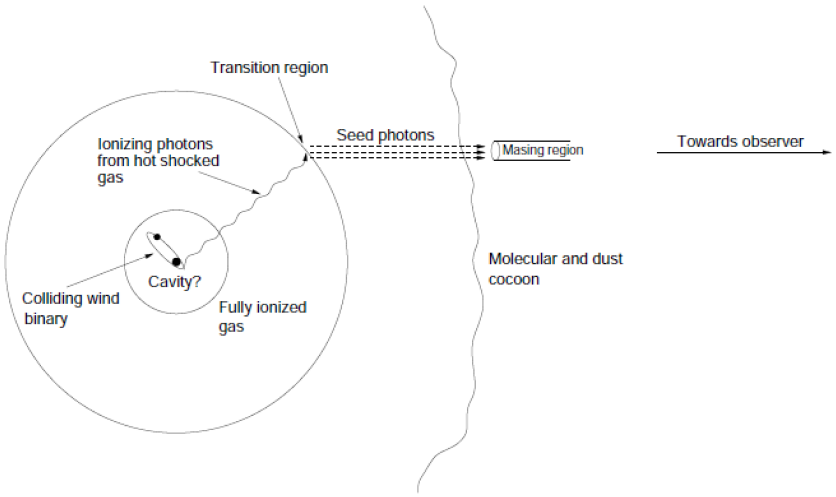

Figure 2.4: Toy model for Colliding Wind Binary (CWB) which produce seed photons to cause masing (van der Walt, 2011).

In the model, two protostars (or a protostar and protoplanet) orbiting each other in an elliptic orbit produce a shock wave front which is due to the colliding wind from the binary system. This process is called Colliding Wind Binary (CWB). A CWB produces an ionisation photon which travels in an ionised hydrogen region without attenuation. When it reaches the partially ionised or unionised region, the photon is absorbed and produces a seed photon which forms a maser.

The pitfall of this model is that there is no direct observational evidence of the binary system in either G9.62+0.20E or G188.95+0.89.

Sobolev et al. (2007) proposed that the dust temperature variations are the source of the observed periodicity in the methanol maser sources. This is due due to the brightness of Young Stellar Object (YSO) or protostar variations due to accretion processes.

Chapter 3

Receiver testing and Observation techniques

3.1 Introduction

The noise diodes for the 2.5-cm and 4.5-cm receivers were calibrated using the hot-cold load Y-factor method. Before receiver calibration, the laboratory radiometer was tested for any deviations from the ideal square-law detector. The test was conducted by sending the signal to the radiometer, and varying the attenuation by the precision attenuator.

In the observation techniques, detailed explanations of the drift scan method (used to collect calibration data), frequency switching method (used to collect spectroscopic data), and the radio astronomical spectroscopic data reduction technique are given.

3.2 HartRAO radio telescope basic details

The 26-m HartRAO radio telescope is an equatorial mounted 25.908-m Cassegrain design built by Blaw Knox in 1961. The telescope is located at 25 53′ 14″.4 (25.887°)

South and 27 41′ 05″.2 (27.685°) East. The basic specifications of the telescope are given in Table 3.1 and Figure 3.1 shows the elevation limit of the telescope.

Diameter	25.9 m
Focal Ratio (f/D)	0.424
Surface Tolerance	0.5-mm rms
Wavelength Limit	1.3-cm
Feed System	Cassegrain
Pointing Resolution	0.001°
Repeatability	0.004°
Slew Rate on each axis	0.5° s^{-1}

Table 3.1: Basic specifications for the 26-m HartRAO radio telescope.

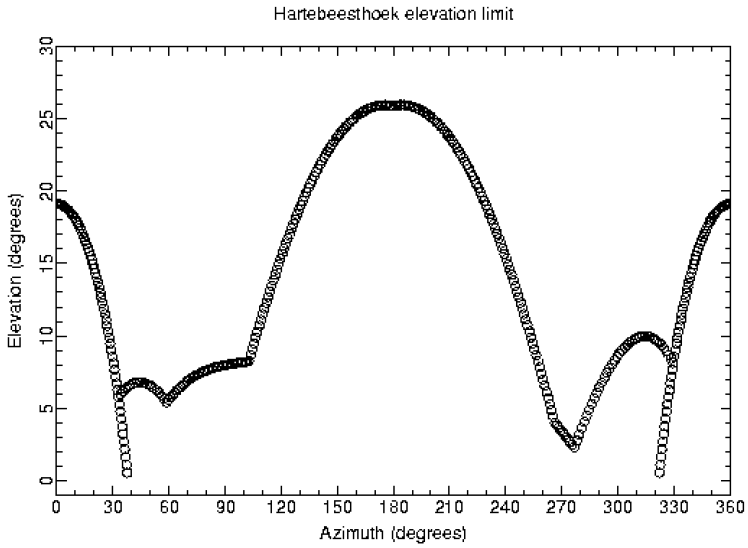

Figure 3.1: Elevation limit as a function of azimuth (Gaylard, 2012).

3.3 Laboratory radiometer calibration

The laboratory radiometer was calibrated to check whether its response followed the ideal "square-law" detector, that is $V_{out} \propto P_{in}$.

For this calibration experiment, the square law detector, signal generator and precision attenuator were used. The signal produced by the signal generator was transmitted to the radiometer by coaxial cable. The radiometer calibration data were obtained by setting the highest attenuation in the precision attenuator in order to set a reference level of the detector's output. The detector output was measured for each attenuation value from 0 to 11 dB in steps of 1 dB. The reference level was subtracted from the voltage measured by the square law detector and the minimum voltage V_m was set to be the detector's output at 11 dB. This was the highest attenuation level of the experiment. The square law detector radiometer output V_o is given by

$$V_o = V_m \exp\left(\frac{(\text{Attenuation in dB})\ln(10)}{10}\right). \tag{3.1}$$

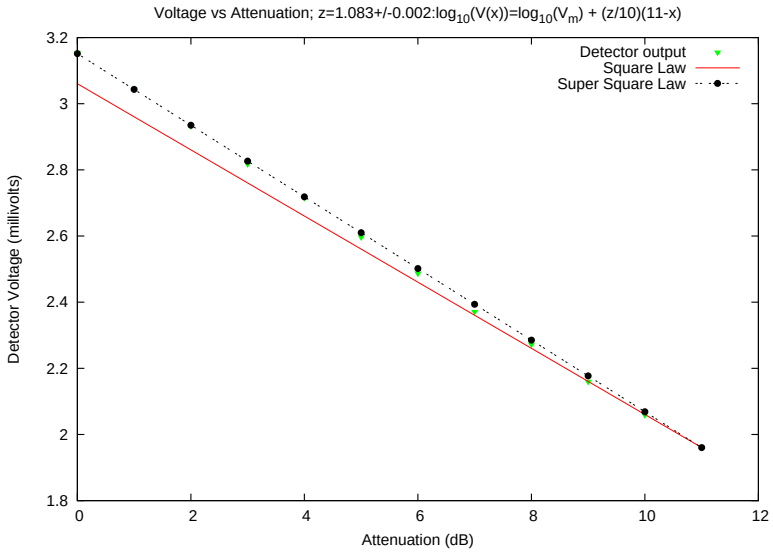

Figure 3.2: Graph of the power output of the square law detector output versus the attenuation (shown by the symbol). The dashed line is the fitted curve to the detector output.

If the attenuation and V_m of the experiment are used to calculate V_o in equation 3.1, the calculated V_o does not fit the output of the radiometer. The results of the experiment are shown in Figure 3.2. The discrepancy between the radiometer output and the expected square law detector output suggest a distortion in Equation 3.1. We therefore introduced an empirical scaling factor β. The new equation can be defined as the output of a super square law detector V_{os} and it is given by:

$$V_{os} = V_m \exp\left(\beta \frac{(\text{Attenuation in dB}) \ln(10)}{10}\right). \tag{3.2}$$

The correction factor in Equation 3.2 was determined using the Gnuplot programme. Equation 3.2 was linearised by $\log_{10}$, fitted to the linearised detector output and the attenuation values from the precision attenuator. The results of the fit are shown by the dash dotted line in Figure 3.2. The best fit produced $\beta = 1.083 \pm 0.002$ (about 8.3 per cent deviation). The deviation is due to the diode in the detector.

3.4 Hot-cold load calibration theory

The method used for the ground-based calibration of the receiver is called the hot-cold load Y-factor method (Sinclair & Gough, 1991). For this method, a cold and hot load is required. Ideally, a square law radiometer would have noise power (P) per frequency bandwidth ($\Delta\nu$) proportional to the system temperature as described by Kraus (1986). To determine the temperature of the noise diode, four different total power output values were measured by a radiometer. The mathematical

representations of these values are shown by the following equations:

$$P_{cold} = \Upsilon \left(T_r + T_{cold} \right), \tag{3.3}$$

$$P_{hot} = \Upsilon \left(T_r + T_{hot} \right), \tag{3.4}$$

$$P_{ND\_cold} = \Upsilon \left(T_r + T_{cold} + T_{ND} \right) \tag{3.5}$$

and

$$P_{ND\_hot} = \Upsilon \left(T_r + T_{hot} + T_{ND} \right). \tag{3.6}$$

Equations 3.3, 3.4, 3.5 and 3.6 have Υ which is the proportionality constant. In Equations 3.5 and 3.6, T_{ND} is the noise diode temperature contribution to the system temperature. Equations 3.3, 3.4, 3.5 and 3.6 illustrate how the calibration of a noise diode is carried out. The frequency is varied across the receiver frequency band while the feedhorn is pointed at a cold or hot load with and without firing the noise diode. The Y-factor term is the ratio of the power output per bandwidth of either $Y = P_{hot}/P_{cold}$ or $Y = P_{ND\_hot}/P_{cold}$. The RCP and LCP Y-factor terms are mathematically equal but the values are not the same due to the fact that each polarisation has its own detector. This implies that the gains will be different, owing to the different component gains in each radiometer.

3.5 The 2.5-cm receiver calibration

The 2.5-cm receiver is shown schematically in Figure 3.3. When the signal enters the polariser, it is split into its left and right circular components.

The signal passes through the noise diode coupler. The low and high noise diode is coupled with the signal, then transmitted into a Low Noise Block (LNB) converter, where the signal is amplified and converted to a lower frequency, which helps reduce the attenuation in the transmission cables. The local oscillator for the LNB is a Dielectric Resonator Oscillator (DRO) locked at 5 MHz standard frequency. The signal from the LNB will then be attenuated before and after going into the post-amplifier. When this receiver is on the 26-m HartRAO radio telescope, the signal from both the left circular polariser (LCP) and right circular polariser (RCP) will be transported to the pre-selector which is in the Dec room. In the Dec room, there is a mixer drawer and filter. From the Dec room the signal is transported to the back-ends (radiometer, spectrometer) in the control room whose output goes to the control computer where it is captured by the observing program.

To calibrate the 2.5-cm receiver with the hot-cold load Y-factor method when the receiver was not installed on the telescope, the sky served as the cold load and Eccosorb material served as the hot load when placed over the feed. The Eccosorb material is a microwave frequency absorber and therefore also acts as a blackbody microwave radiator. The measurement steps followed were sky, sky with noise diode, Eccosorb and Eccosorb with noise diode. Since the output is distorted, the Y-factors (Y_1 and Y_2) need correction for the deviation from the square law. The corrected Y-values are given by $Y_1 = \left(\frac{P_{hot}}{P_{cold}}\right)^{\frac{1}{\beta}}$ and $Y_2 = \left(\frac{P_{ND\_hot}}{P_{cold}}\right)^{\frac{1}{\beta}}$.

Figure 3.4 shows the averages of the low and high noise diode for both LCP

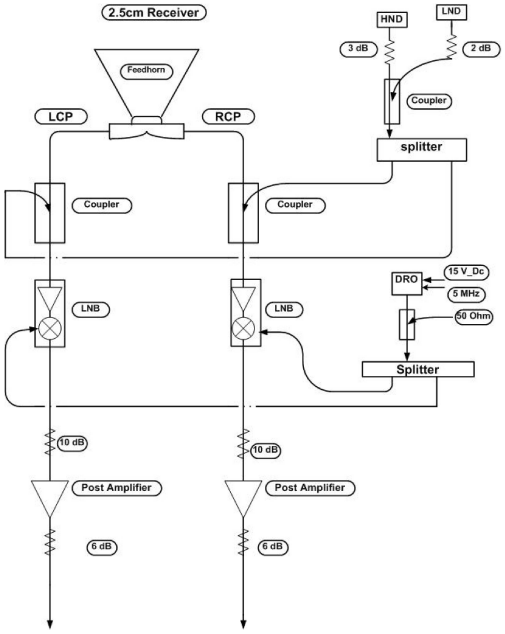

Figure 3.3: Schematic diagram for 12178-MHz (2.5-cm) HartRAO telescope receiver.

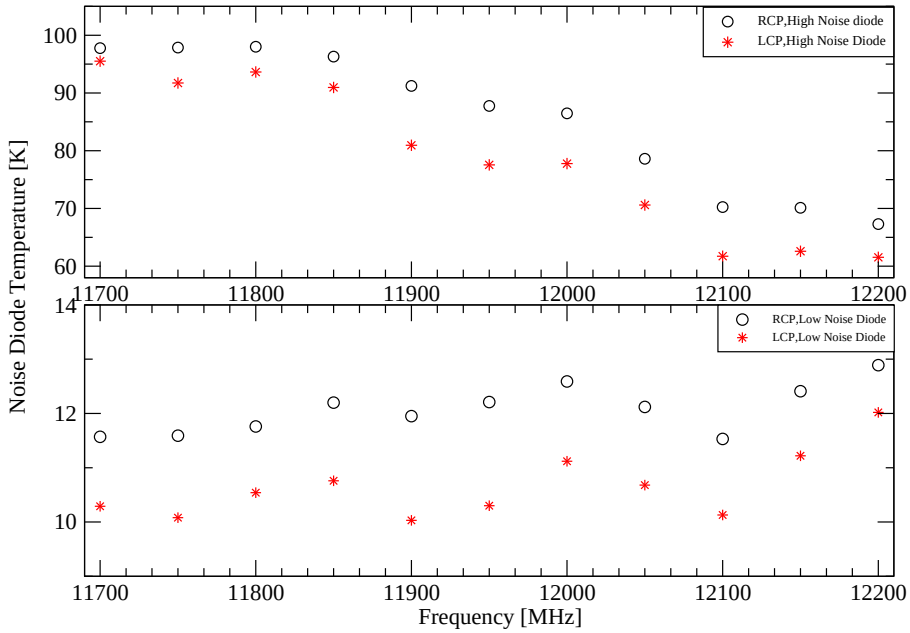

Figure 3.4: The average noise temperature at LCP and RCP of the high and low level noise diode as a function of frequency for the 2.5-cm receiver.

and RCP. The low noise diode shows very small variations across receiver frequency band. On the other hand, the high noise diode starts to decrease as the frequency is increased.

3.6 The 4.5-cm receiver calibration

The 4.5-cm HartRAO receiver was also calibrated using the hot-cold load Y-factor method. The block diagram for this receiver is shown in Figure 3.5. The design is similar to the 2.5-cm receiver but the significant difference is that it has a cryogenic refrigerator. The cryogenic refrigerator minimises the noise contribution from the Low Noise Amplifier (LNA) and other components. The isolator confines the signal to one direction, which implies that there will be no additional noise due to the signal reflection during transmission.

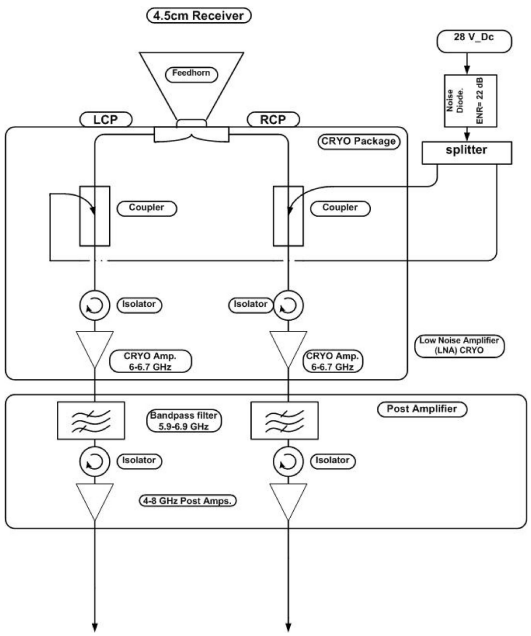

Figure 3.5: Schematic diagram for 6668-MHz (4.5-cm) HartRAO radio telescope receiver.

The apparatus used for the 4.5-cm receiver calibration experiment in the laboratory consisted of liquid nitrogen, an AIL7009 Hot-Cold Standard Noise Generator, the 4.5-cm receiver and a radiometer. The AIL7009 has a built-in heater compartment which is at 100° C ($\sim$ 373.2 K) and also has a compartment to hold the liquid nitrogen. Liquid nitrogen ($\sim$ 77.3 K) was poured into the AIL7009. It was allowed to reach thermal equilibrium by waiting for at least an hour. The heater and liquid nitrogen served as hot and cold load respectively.

The measurements were done as in the 2.5-cm receiver, where the coaxial cable was connected to the liquid nitrogen and the heater compartment, and the computer was used to scan through the receiver frequency band, and the output from the laboratory radiometer was recorded onto disk.

The temperatures for the hot and cold load have to be corrected for RF losses. To correct for RF losses in the AIL7009, the internal RF losses graph from the manual was used. The hot load temperature (T_H) is defined as $T_H = 373.2 + \Delta T_H$ K, where ΔT_H is the internal RF loss correction for the hot load. Since ΔT is a function of frequency for both the hot (ΔT_H) and cold (ΔT_C) loads, a second-order polynomial was fitted to both hot and cold load RF internal losses diagram which was found in the receiver manual. From the fitted second-order polynomial, the corresponding RF temperature corrections (ΔT_H and ΔT_C) were determined for each frequency. The cold load temperature was $T_C = 77.3 + \Delta T_C - 1.4$ K, where 1.4 K allows for the 1400-meter altitude of the observatory where the experiment was conducted.

The noise diode temperature for both RCP and LCP across the receiver frequency band are shown in Figure 3.6.

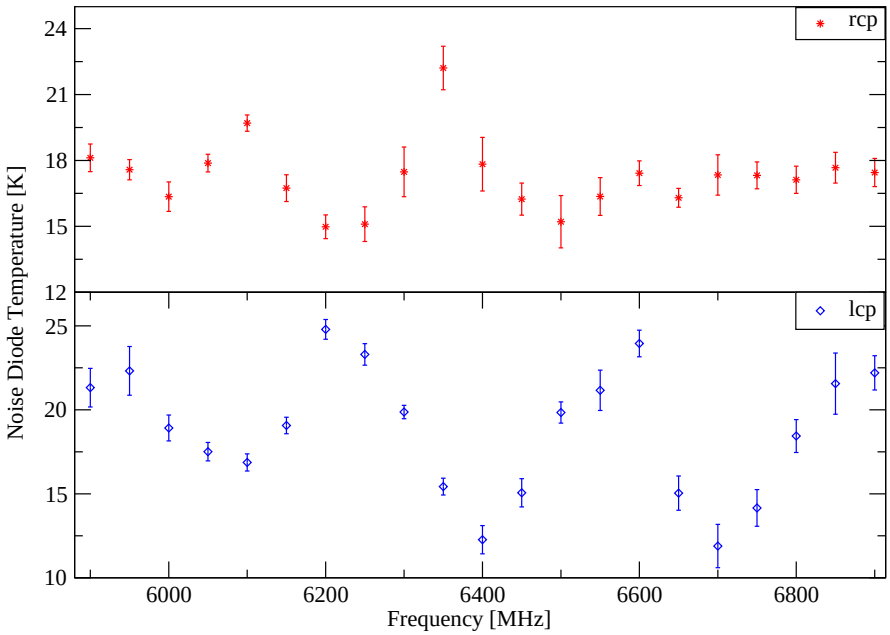

Figure 3.6: Variations of the LCP and RCP noise diode temperature as a function of frequency across the frequency band of the 4.5-cm HartRAO receiver. The ripples indicate some mismatch in system components.

3.7 The drift scan

The calibration data were captured randomly every one to three days depending on the telescope availability, using a drift scan. In this method, the telescope is parked ahead of the source's path so that the source moves across the telescope beam (Figure 3.7). The raw light curve does not have a flat baseline due to noise and sidelobes. Three raw drift scans were taken, one nominally through the center of the beam and each through the north and south half-power points, respectively. From each of these three drift scans, the amplitude was calculated by fitting a second-order polynomial to the peak of the source in the drift scan. For the purpose of determining the pointing error, each scan's amplitude can be characterised by a Gaussian function profile, $P_\theta = P_o \exp\left(-\ln(2)(\delta\theta/b)^2\right)$. These three scans can be

mathematically defined as

$$T_n = T \exp\left(-\ln(2)\left(\frac{\delta\theta + b}{b}\right)^2\right), \tag{3.7}$$

$$T_s = T \exp\left(-\ln(2)\left(\frac{\delta\theta - b}{b}\right)^2\right) \tag{3.8}$$

and

$$T_{on} = T \exp\left(-\ln(2)\left(\frac{\delta\theta}{b}\right)^2\right). \tag{3.9}$$

What is required from the drift scan is the true antenna temperature which is T in Equations 3.7, 3.8 and 3.9. The offset between the source and center of the beam is $\delta\theta$ and the beamwidth at the half power point is b. The offset $\delta\theta$ can be determined from either $\ln(T_n/T_s)$ or $\ln(T_n/T_{on})$ or $\ln(T_s/T_{on})$. For each case, T can be determined. The pointing error will be the exponential term after making T the subject of the formula in either Equation 3.7 or 3.8 or 3.9.

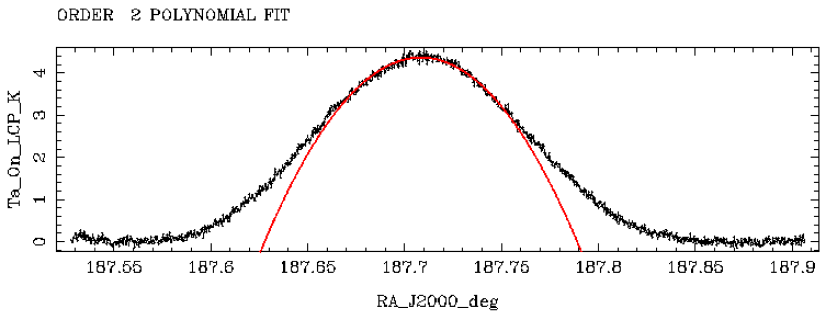

Figure 3.7: The light curve for a drift scan on the calibrator after correcting for the baseline flatness. It was produced by spectral analysis application called Lines developed by Dr. M. J. Gaylard at HartRAO.

The corrected antenna temperature (T) is used to determine the Point Source

Sensitivity (PSS), defined as the number of Kelvins of antenna temperature produced by one Jy of flux density in each polarisation. For a small antenna the inverse of PSS may be used to convert the flux density from Kelvin to Jansky (Condon & Ransom, 2010). Since electromagnetic radiation is polarised and radio astronomy receivers are sensitive to the polarisation, it implies that each circular polarisation receives half of the total flux density (for an unpolarised emitter). For each polarisation the PSS is given by:

$$PSS = \frac{S}{2K_s T_A}, \tag{3.10}$$

where K_s is the correction factor for the source ($K_s = 1$ for a point source). Once the PSS has been determined from radio source calibrators, it is used to convert the spectrum intensity (measured in antenna temperature, in Kelvin) into a flux density (measured in Jansky).

Three sources were used to calibrate both the 4.5-cm (6668-MHz) and 2.5-cm (12178-MHz) receivers on the 26-m HartRAO radio telescope. These were 3C123, Hydra A and Virgo A. Virgo A is the brightest calibrator of the three, but it is not an ideal calibrator for determining the point source sensitivity of the telescope at 6668-MHz and 12178-MHz as it not a point source in the beam. So 3C123 and Hydra A were used for determining the point source sensitivity. Virgo A was used as a consistency check (with high signal to noise ratio) on the point source sensitivity. Their flux densities were found from Ott et al. (1994).

3.7.1 The 26-m HartRAO telescope calibration

If there are changes in the Point Source Sensitivity (PSS) values, there will be changes in the time series of the raw concatenated spectra but these changes can be corrected for by scaling the spectra by the PSS values.

Figures 3.8, 3.9 and 3.12 show step changes in the PSS at 6668 MHz. The first step change is due to a shift in the position of the 26-m telescope subreflector, owing to a malfunctioning readout. This means that the signal was not properly focused onto the receiver.

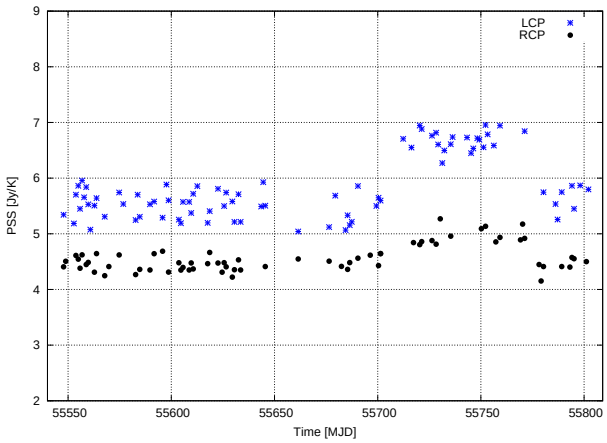

Figure 3.8: PSS for the 3C123 calibrator for the LCP and RCP at 6668 MHz.

The step changes are also observed in Figures 3.10, 3.11 and 3.13 at 12178 MHz. The data points before the first step change (from 55430 to 55542 MJD) results from using the ratio of the high and low noise diodes to scale the drift scans. The rest of the step changes are due to a change in the position of the subreflector. The last step change in all PSS figures for 3C123, Hydra A and Virgo A is when the subreflector was set back to its original position.

In Figures 3.8, 3.9, 3.10, 3.11, 3.12 and 3.13, the LCP and RCP PSS values are

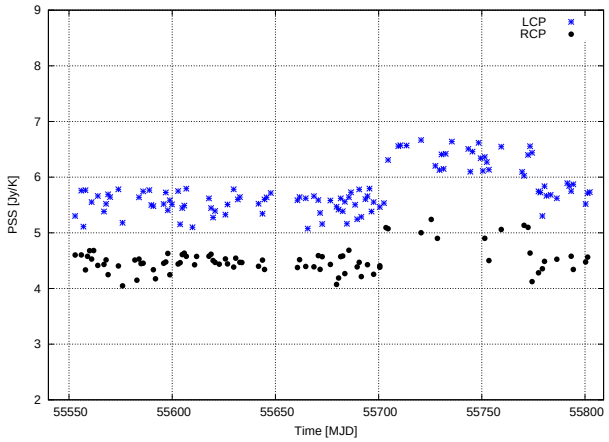

Figure 3.9: The LCP and RCP PSS for the Hydra A calibration source at 6668 MHz.

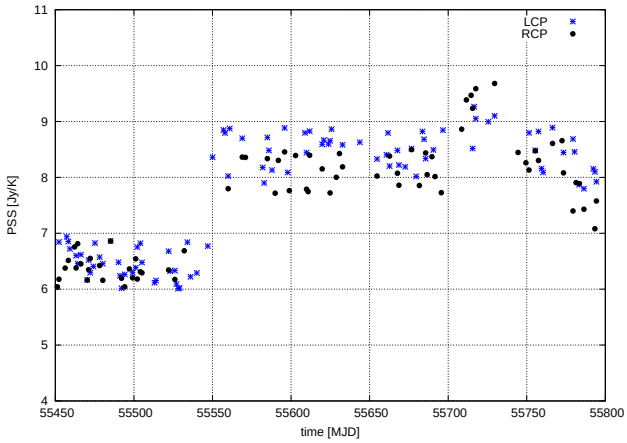

Figure 3.10: The 3C123 calibrator PSS for both LCP and RCP at 12178 MHz.

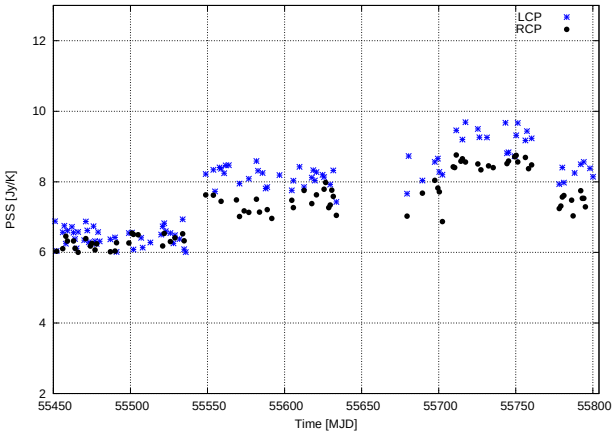

Figure 3.11: Hydra A PSS for both LCP and RCP at 12178 MHz.

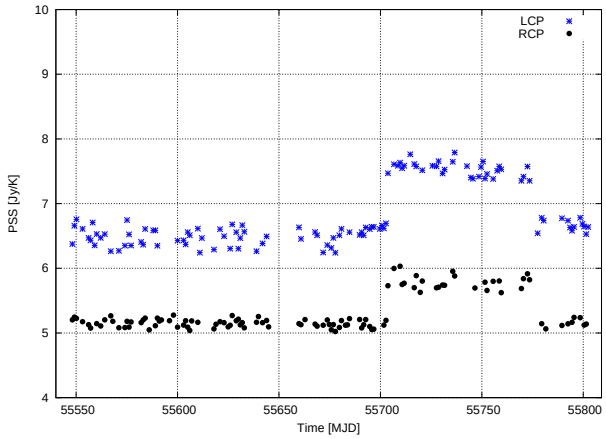

Figure 3.12: The Virgo A calibration source PSS for both LCP and RCP at 6668 MHz.

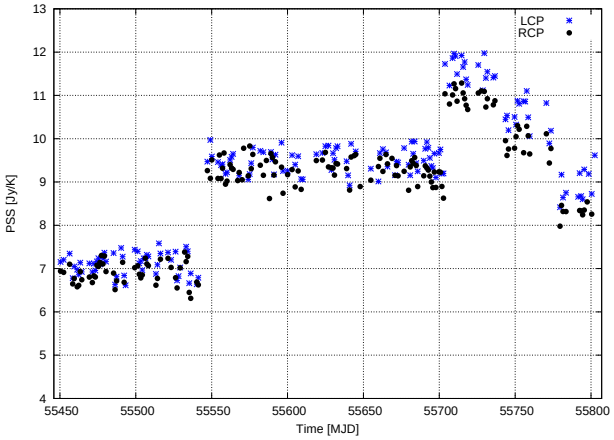

Figure 3.13: The Virgo A PSS for LCP and RCP at 12178 MHz.

Start Day (MJD)	End Day (MJD)	PSS_{lcp} (Jy/K)	$\Delta(PSS_{lcp})$ (Jy/K)	PSS_{rcp} (Jy/K)	$\Delta(PSS_{rcp})$ (Jy/K)
55548.136	55702.720	5.495	0.036	4.447	0.032
55703.701	55742.655	6.542	0.032	5.012	0.039
55744.591	55773.516	6.478	0.033	4.920	0.037
55777.500	55802.446	5.682	0.035	4.423	0.036

Table 3.2: Table of PSS values at 6668 MHz. The start and end dates are measured in Modified Julian Date (MJD). The third and fifth column are the PSS values for RCP and LCP, respectively. The uncertainty of the LCP and RCP are shown in the fourth and sixth columns, and they were determined by calculating the sample standard deviation.

Start Day (MJD)	End Day (MJD)	PSS_{lcp} (Jy/K)	$\Delta(PSS_{lcp})$ (Jy/K)	PSS_{rcp} (Jy/K)	$\Delta(PSS_{rcp})$ (Jy/K)
55430.000	55541.170	6.455	0.026	6.326	0.029
55547.157	55702.741	8.343	0.029	7.788	0.039
55703.740	55736.648	9.134	0.021	8.940	0.037
55743.623	55773.544	8.843	0.025	8.477	0.033
55779.528	55802.467	8.119	0.020	7.492	0.036

Table 3.3: This table shows the values of the average PSS and their uncertainty at 12178 MHz. The start date (column one) and end date (column two) for each PSS value were all measured in Modified Julian Date (MJD).

different. The difference is due to the different radiometers used for each polarisation which implies that the gains will be different.

Virgo A has a good signal-to-noise ratio at both 6668 MHz (Figure 3.12) and 12178 MHz (Figure 3.13).

For each period, the PSS was determined by taking the average PSS from the Hydra A and 3C123 calibrators, and the error of the PSS was determined from the standard deviation (Tables 3.2 and 3.3). Since the final PSS value is defined as: $PSS = \frac{\left(PSS_{hyd}+PSS_{3c1}\right)}{2}$, the uncertainty in the final PSS value was determined using error propagation (Taylor, 1997). The uncertainty is given by

$$\Delta(PSS) = \frac{1}{2}\sqrt{\left[\Delta(PSS_{3c1})\right]^2 + \left[\Delta(PSS_{hyd})\right]^2}, \tag{3.11}$$

where $\Delta(PSS_{hyd})$ is the standard deviation for the Hydra A PSS and $\Delta(PSS_{3c1})$ is the standard deviation of 3C123 PSS value.

After reducing all spectra for each source, the antenna temperatures were converted to flux densities using the PSS values in Tables 3.2 and 3.3.

The PSS values used for the data before the 26-m HartRAO bearing failure were

found from Dr. S. Goedhart. The bearing can affect observations during source tracking because the telescope does not move smoothly. The drive motor on the 26-m HartRAO telescope is powerful enough to track the source but it was damaging the bearing more and more as it was tracking. Other than this, it was unlikely that it affected the data provided the pointing was corrected for. The pointing started to deteriorate as the bearing became more damaged. Pointing corrections are done regularly at the observatory which implies that the artificial variations in the time series were nullified.

3.8 Observing method: Spectroscopy

3.8.1 Frequency to velocity conversion

The spectra in the spectrometer are corrected for some of the Doppler shift effects of the Earth's motion around the Earth-Moon barycenter, the Earth's motion around the Sun and the Sun's motion with respect to the local standard of rest (Shu, 1982). The resultant velocity is called the velocity with respect to the local standard of rest (V_{lsr}). The Doppler shift due to galactic rotation (e.g. peculiar motions for stellar objects with respect to their surroundings) is not corrected in V_{lsr}.

In radio astronomy, the spectrum units are converted from frequency into V_{lsr}. The frequency shift due to the velocity along the line of sight is defined by the ratio of the Line Rest Frequency (LRF) and the speed of light in the vacuum (c). In our studies, two Line Rest Frequencies were used and their Doppler conversion factors are: 22226.7 Hz/km.s^{-1} (for 6668-MHz LRF) and 40593.3 Hz/km.s^{-1} (for 12178-MHz LRF). Dividing the bandwidth by the Doppler shift conversion factor

gives the velocity range (measured in km.s^{-1}) covered by the receiver.

3.8.2 Single-dish observing techniques

Mangum (2006) has given short notes on the observing technique used in radio astronomy. These include position switching, frequency switching and beam switching. With the position switching technique, the spectrum from the on-source (B_{on}) position and off-source (B_{off}) position are taken. The total power will be given by the following equation:

$$Total\_Power = \left[\frac{B_{N_{on}} - B_{N_{off}}}{B_{N_{off}}}\right] T_{sys_{on}}, \tag{3.12}$$

where $T_{sys_{on}}$ is the on-source system temperature, $B_{N_{on}} = B_{on}/T_{sys_{on}}$ and $B_{N_{off}} = B_{off}/T_{sys_{off}}$, are both normalized. Equation 3.12 eliminates almost all the instrumental bandpass response. The position switching technique is useful when observing complex emission regions.

For monitoring methanol maser source regions with the 26-m HartRAO radio telescope, the frequency switching technique was used. In this method, the Local Oscillator (LO) frequency is changed to shift the spectrum to the left and right in the passband. It can be outside the receiver band or inside the receiver band. When the shift is within the bandwidth then the signal will appear twice and this is called the in-band frequency switching technique. Since the spectrum appears twice, it implies that the signal-to-noise ratio will be improved by the square root of two ($\sqrt{2}$). The total power spectrum may not have a flat baseline. To correct for this problem, a first-order polynomial function is fitted to the baseline which does

not have line emission(s). The total power in the frequency switching technique is measured in a similar way to the position switching given in equation 3.12, with just two changes in the labelling of the variables:

$$Total\_Power = \left[\frac{A_{N_{sig}} - A_{N_{ref}}}{A_{N_{ref}}}\right] T_{sys_{sig}}. \tag{3.13}$$

In equation 3.13, both $A_{N_{sig}} = A_{sig}/T_{sys_{sig}}$ and $A_{N_{ref}} = A_{sig}/T_{sys_{ref}}$, are normalized. When the spectrum is shifted out of the bandwidth, A_{ref} will not contain the spectrum, but for the in-band frequency switching technique, there will be a signal in both A_{ref} and A_{sig}.

The spectra were observed using the 26-m HartRAO radio telescope. The data were collected at irregular intervals. The overall total power for the spectrum is the sum of the power from both LCP and RCP, because the radio telescope detectors are sensitive to the polarization of the radiation.

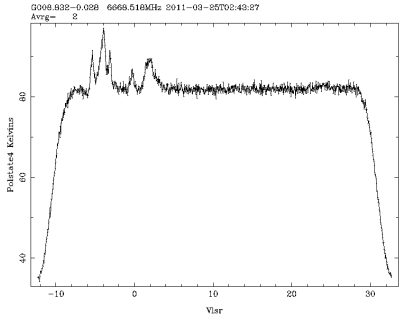

Figure 3.14: Sample raw spectrum from the 1024 channel spectrometer of the 26-m HartRAO radio telescope which has been shifted by a quarter of the bandwidth to the left.

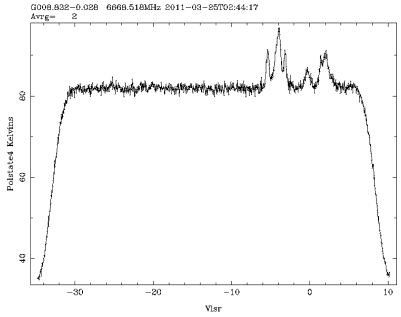

Figure 3.15: Sample raw spectrum from the 1024 channel spectrometer of the 26-m HartRAO radio telescope. The spectrum has been shifted to the right by a quarter of the bandwidth.

Figure 3.14 and 3.15 show the in-band frequency switching technique. Figure 3.14 has been shifted to the left and Figure 3.15 has been shifted to the right. In

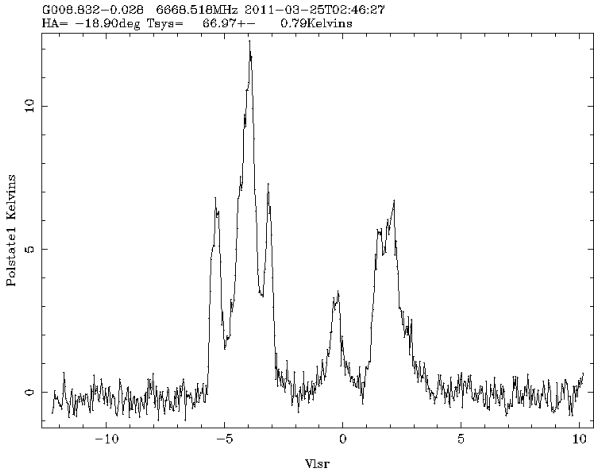

Figure 3.16: This difference spectrum intensity measured in antenna temperature (units are Kelvin). The spectrum was obtained from the spectra shifted to the left and right by a quarter of the bandwidth shown in Figures 3.14 and 3.15.

order to determine the spectrum measured in Kelvins, equation 3.13 was used. The result of equation 3.13 is shown in Figure 3.16, where Figures 3.14 and 3.15 were combined using the Lines program (application developed by Dr. M. J. Gaylard at HartRAO).

The peaks in the spectrum (Figure 3.16) are the masers. When the interferometric observations of the maser source regions are made using a network of radio telescopes, the maser spot sizes and their locations can be determined.

The methanol maser sources monitoring programme at HartRAO with the 26-m radio telescope were first monitored using the HP1000 minicomputer with a 256 channel single polarisation spectrometer. It was the original control system which lasted until the year 2003. This was then replaced by a Linux-based New Control Computer System (NCCS) from the year 2003 to date. The new system has a 1024 channel spectrometer for each polarisation. The monitoring programme dates back to the time when the 26-m HartRAO radio telescope was using the HP1000

minicomputer and the data of that time is often referred to as HP data. The data from the NCCS computer is called NCCS data.

The control system accepts the executable file compiled using the Parser. The file has observational information about the sources to be observed. For bright sources, pointing corrections were determined. To calculate for pointing corrections, four spectra offset by a half power beamwidth were taken at North, East, West and South.

3.9 Data capture and reduction uncertainties

There are many variables which can contribute in the uncertainty in the flux density measurements. These factors can introduce some variabilities in the measured methanol maser flux densities and are:

Pointing error was calculated and corrected in most of our methanol maser sources. Pointing uncertainties arise due to deformation of the radio telescope, Which could be the contraction and expansion of the telescope as the temperature varies across the day, night or season. It could be also due to earth gravitational force as telescope points away from zenith. Data with large pointing values were discarded or considered as bad data. Pointing error had a strong contribution to the sources which had no pointing observations.

The amplitude calibration of the spectra comes from the system temperature measurement done with each spectrum, as shown in equations 3.12 and 3.13 (section 3.8). The normalised spectra are scaled by multiplying by system temperature. This means that the system temperature can introduce the uncertainty in the flux density

measurements. The part of the system temperature is due to atmospheric conditions which affect the propagation of electromagnetic radiation (Karmakar et al., 2010). The electronics also contribute to the system temperature. The atmospheric corrections were not calculated in our spectra since atmospheric effects are negligible at low frequency compare to masers provided there was no rain (Karmakar et al., 2010). The spectra with high system temperatures were not included in our data.

The uncertainty in Kelvin to Jansky conversion comes from how the calibrator data was processed. Tables 3.2 and 3.3 show standard deviations or standard errors of the measured Point Source Sensitivity (PSS). The standard errors in the PSS ranges from 0.020 - 0.039 Jy.K^{-1} which implies that the variations contribution from the spectra scaling factor (PSS) is less than four per cent (4.0 %). So the uncertainty in Jy to K conversion is negligible.

No correction has been made for atmospheric absorption, but the observations are always made in a small hour angle range ($\sim$ 3 hours) near zenith meridian transit. This will reduce the gain-elevation effect, atmospheric absorption path, and the effects of deformation due to earth gravity. The masers which were observed for this thesis are bright - implying we were far from the limiting sensitivity.

Chapter 4

Time series analysis methods

4.1 Introduction

In astronomy, it is very hard to get data that are evenly sampled. There are many contributing factors - the availability of telescope time, environmental factors (such as bad weather), telescope maintenance, etc. If evenly sampled data were easy to obtain then searching for periodicity would require classic period search methods.

Three methods which can be used to search for periods in the evenly sampled data are discussed. These are: the Lomb-Scargle, Phase Dispersion Minimization (PDM) and epoch-folding methods. The discussion presented for the Lomb-Scargle and epoch-folding methods was translated into Python script, and periodic data were created to test the Python script.

The correlations and time delays between two time series were determined using the z-transform Discrete Correlation Function (ZDCF) method and the description of this method is also given in this chapter.

4.2 The Lomb-Scargle period search method

A periodogram is the best tool for studying spectral statistics. Lomb (1976) derived an equation for the periodogram for unevenly spaced data. The method is based on a least-squares frequency analysis (Vaníček, 1971). It uses the least-squares procedure which fits a series of harmonic waves to the time series. The efficiency and reliability of Lomb's periodogram has been studied by Scargle (1982).

Astronomical data are noisy and the classical periodogram will have peaks due to noise. To deal with this challenge, large data samples ($N_o >> 1$) should be taken which will increase the signal to noise ratio.

Another challenge in the periodogram frequency analysis is the spectral leakage which is the power spectral leakage. It can be solved by smoothening the periodogram (e.g. using a data windowing or tapering method (Harris, 1978; Scargle, 1982)).

Since it is possible to have peaks due to noise in the periodogram, it is important to do a significance test on the period determined. The false alarm probability method was used (Scargle, 1982). This method uses the Cumulative Distribution Function (CDF) (Scargle, 1982). In order to get a false alarm probability for the existence of a period, the power level limit z_o which corresponds to the false alarm probability p_o must be set. So the false alarm probability p_o is given by the probability of getting powers greater than the power level limit which is $Pr(Z > z_o)$. $Pr(Z > z_o)$ is one minus the cumulative distribution function (CDF) for an exponentially distributed power Z of the power level limit $F_Z(z_o)$ (Scargle, 1982). So $p_o = Pr(Z > z_o) = 1 - F_Z(z_o)$. The desired power limit for N frequencies can be

derived by making z_o the subject in equation 4.1.

$$p_o = 1 - \{1 - \exp(-z_o)\}^N. \tag{4.1}$$

The threshold power is z_o and any power P below the threshold power will not be detected. Evaluating the CDF at the threshold power level z_o should hold the information about the probability of missing a signal with power P. So the detection efficiency is the probability of detecting the signal of power P, which is just an absolute value of the difference between one and the probability of missing the signal of power P.

For evenly sampled data, the summation over sine and cosine are orthogonal. The physical interpretation of orthogonal is that the variables which are orthogonal are independent of each other therefore, $P(\omega_n)$ is independent. For astronomical data $P(\omega_n)$ is a dependent variable because of unevenly spaced. This problem can be solved by choosing appropriately gridded frequencies. When the power for the evenly sampled data is compared with the power of appropriately gridded frequencies in the unevenly sampled data, the difference is either small or zero (Lomb, 1976).

The normalized periodogram defined by Lomb (1976) and Scargle (1982) (Lomb-Scargle periodogram) is slow and the required computation number is the product of the number of frequencies tested, N, and total number of data point sampled N_o. It is quite expensive in terms of computation in standard computer time. Press & Rybicki (1989) have solved this problem by introducing some new variables which convert some of the terms in the Lomb-Scargle periodogram into a Fast Fourier Transform (FFT).

The significant change made in the Lomb-Scargle method was to change y_i into

$y_i - \bar{y}$, where $\bar{y}$ is the mean. The new periodogram will be:

$$P_N(\omega) = \frac{1}{2\sigma}\left\{\frac{\left[\sum_i (y_i - \bar{y})\cos\omega(t_i - \tau)\right]^2}{\sum_i \sin^2\omega(t_i - \tau)} + \frac{\left[\sum_i (y_i - \bar{y})\sin\omega(t_i - \tau)\right]^2}{\sum_i \cos^2\omega(t_i - \tau)}\right\}. \quad (4.2)$$

New terms can be defined and they come in handy when simplifying equation 4.2, these are:

$$\begin{aligned} S_y &= \sum_{i=1}^{N_o} y_i \sin(\omega t_i), \quad C_y &&= \sum_{i=1}^{N_o} y_i \cos(\omega t_i), \\ S_2 &= \sum_{i=1}^{N_o} \sin(2\omega t_i), \quad C_2 &&= \sum_{i=1}^{N_o} \cos(2\omega t_i) \end{aligned} \quad (4.3)$$

The trigonometric identities can be used to reduce the cosine and sine terms in equation 4.2. S_y, S_2, C_y and C_2 can be obtained from two complex FFTs. This will make the periodogram faster even on a standard computer.

The false alarm probability method used to test the significance of the periods determined by the Lomb-Scargle method does not always work. Schwarzenberg-Czerny (1998) derived another false alarm distribution function which is called the Schwarzenberg-Czerny false alarm function and it is given by:

$$I_{1-z_o/N_o/2}([N_o/2], 1) = \left(1 - \frac{z_o}{[N_o/2]}\right)^{\frac{N_o}{2}}, \quad (4.4)$$

where N_o is size of the data sample and z_o is the threshold power as defined earlier. It has been shown by Frescura et al. (2008) that for a small data sample, a false alarm probability function given by Scargle (1982) deviates from empirical CDFs. To solve this problem, equation 4.4 can be substituted in place of the term $1 - \exp(-z_o)$ in equation 4.1.

The above theory was converted into the Python programming language. The code inputs the time series and produces the periodogram for each time series.

4.3 The Phase Dispersion Minimization method

The period in the time series can also be determined by the Phase Dispersion Minimization (PDM) method. This uses a least-squares method to determine the period. Time series data are a two vector function ($\mathbf{x}$), which is given by the magnitude x_i measured at time t_i (where $i = 1, 2, 3, ..., N-1, N$). The variance of the data can be obtained by:

$$\sigma^2 = \frac{\sum_{i=1}^{N} x_i - \bar{x}}{N-1}. \tag{4.5}$$

In equation 4.5, $\bar{x} = \frac{\sum_{i=1}^{N} x_i}{N}$ is the mean of the data. One can create a subset of vector space $\mathbf{x}$ and the variance of the subset can be determined by equation 4.5. Creating a subset of the vector space $\mathbf{x}$ is achieved by binning the data. The total number of bins can be defined by M. ${s^2}_j$ will be defined as the variance of the subset j where $j = 1, 2, 3, ..., M-1, M$. Each subset will have n_j data points. The overall variance s^2 can be calculated from equation 4.6,

$$s^2 = \frac{\sum_{j=1}^{M} (n_j - 1)\, {s^2}_j}{\sum_{j=1}^{M} n_j - M}. \tag{4.6}$$

The Phase Dispersion Minimization (PDM) method minimizes the variance of the data with respect to the mean of the light curve. In order to achieve this, the M subset of the vector space $\mathbf{x}$ must be determined by the phase vector ϕ. Stellingwerf

(1978) defined the phase vector as follows:

$$\phi : \phi_i = \frac{t_i}{P_{test}} - \left[\frac{t_i}{P_{test}}\right]. \tag{4.7}$$

The square brackets in equation 4.7 imply that only the integer is considered in the time t_i and period P_{test} ratio. Equation 4.7 shows that the phase vector $\phi \in (0, 1)$. The phase vector is divided into bins. The corresponding x_i values which fall under the defined bin width produced by the test period P_{test} and time t_i are grouped into M bins. In each bin, PDM can be determined by:

$$\Theta^2 = \frac{s^2}{\sigma^2}, \tag{4.8}$$

where s^2 is determined by equation 4.6 and σ^2 is determined by equation 4.5 (Stellingwerf, 1978). If P_{test} is a true period then $\Theta^2 \approx 0$. If it is not a true period, then $\Theta^2 \approx 1 \implies s^2 \approx \sigma^2$. This method seeks to minimise the dispersion of the data at constant phase, hence it is called Phase Dispersion Minimization (PDM). This is a least-squares method where the curve is defined by means of each bin, and as a result, the best fit period and the best least-squares light curve are found simultaneously.

4.4 The epoch-folding method

In the epoch-folding period search method, the time series is folded in the same way as in the PDM which is finding the modulo of P_{test}. Leahy et al. (1983) defined

epoch folding statistics as follows:

$$Q^2 = \sum_{j=1}^{M} \frac{(\bar{x_j} - \bar{x})^2}{{\sigma^2}_j}, \tag{4.9}$$

where ${\sigma^2}_j$ is the variance in the j^{th} bin and $\bar{x_j}$ is the mean of the data in the j^{th} bin. Larsson (1995) gave an in-depth epoch-folding analysis where for each P_{test} the Q^2 was evaluated. The true period is found where Q^2 is a maximum. The existence of a period or periodicity occurs when $Q^2 >> (M-1)$ and its significance can be determined from the distribution of Q^2.

Davies (1990) defined three new terms in the analysis of variance. Using the null hypothesis, ${\sigma^2}_j$ was assumed to be given by ${\sigma^2}_j = \frac{\hat{\sigma}^2}{n_j}$, where $\hat{\sigma}^2$ is the overall sample variance. These new terms are:

$$SST = \sum_{i=1}^{N} (x_i - \bar{x})^2, \tag{4.10}$$

$$SSA = \sum_{j=1}^{M} n_j (x_j - \bar{x})^2 \tag{4.11}$$

and

$$SSE = \sum_{j=1}^{M} \sum_{k=1}^{n_j} (x_{kj} - x_j)^2 = (N-M)\Theta^2\hat{\sigma}^2. \tag{4.12}$$

Analysis of the variance (ANOVA) is the study of the effects of splitting the total variance into its components. SSA in equation 4.11 is the variance between

the groups or subsets of a set, and SSE in equation 4.12 is the variance within the elements of a group or subset. Davies (1990) defined $SST = SSA + SSE$ which is for a one dimensional classification by phase. So SST is the measure of the total variability of x over the entire set. SSA and SSE are mutually independent (Hines & Montgomery, 1972). The PDM test statistic Θ^2 and the epoch-folding test statistics Q^2 can be determined in terms SST, SSA and SSE. The Θ^2 and Q^2 do not obey the F-distribution because the numerator and the denominator are dependent, therefore the significance of the period determined from either Θ^2 or Q^2 cannot be determined by Stellingwerf's statistical test (Davies, 1990). Using ANOVA, L-statistics can be determined in terms of Θ^2 and Q^2:

$$\left.\begin{aligned} L &= \frac{Q^2}{(M-1)\,\Theta^2}, \\ L &= \frac{(N-1)-(N-M)\,\Theta^2}{(M-1)\,\Theta^2}, \\ L &= \frac{(N-M)\,Q^2}{(M-1)\,[(N-1)-Q^2]}. \end{aligned}\right\} \tag{4.13}$$

The period can be calculated using either PDM [see equation 4.8] or epoch-folding [see equation 4.9] but the significance of the calculated period should be tested with L-statistics [see equation 4.13].

The epoch-folding and its test statistic which is the L-statistic were implemented in the python programming language. So the data were first folded by phase and then the variance was calculated for each bin. The L-statistic was applied to the epoch-folding to test the significance of the period.

4.5 The Lomb-Scargle and epoch-folding testing

In order to test the Lomb-Scargle and epoch-folding program (coded in Python), test time series were created. In the Python programming language, the data for G9.62+0.20E at 12178-MHz were loaded and its time component in MJD was used to generate unevenly spaced cosinusoidally varying time series. The period of the cosine function was set to 250 days with amplitude ranging from 0-20 (arbitrary units). In order to deviate from ideal periodic behaviour to create realistic data, noise was generated using a module in Numpy. The module is called *numpy.random.normal(mean='input',standard='input',number of data point='input')*. The noise was added to the cosine function data points. The mean was kept at zero and the standard deviation was set at 0, 1, 5, 10 and 50. These time series are shown in Figure 4.1.

As the standard deviation of the Gaussian noise increases, it becomes hard to see with the naked eye that the data are periodic (Figure 4.1). To determine the period for the test data, the Lomb-Scargle (Figure 4.2) and epoch-folding (Figure 4.3) period search methods were used.

The Lomb-Scargle periodograms show the existence of a period for all the Gaussian noise standard deviation (STD). The significance test limit was set to be less than 0.0001 (significance < 0.0001) in the script. A smaller significance value gives a smaller probability and lower probability gives a better significance of the peak. The stars in Figure 4.2, hold information about the significance of the peak. The stars are the points above the significance peak detection limit.

For the epoch-folding method, as the Gaussian noise standard deviation increases, the width of the power peak increases. The periods determined are sum-

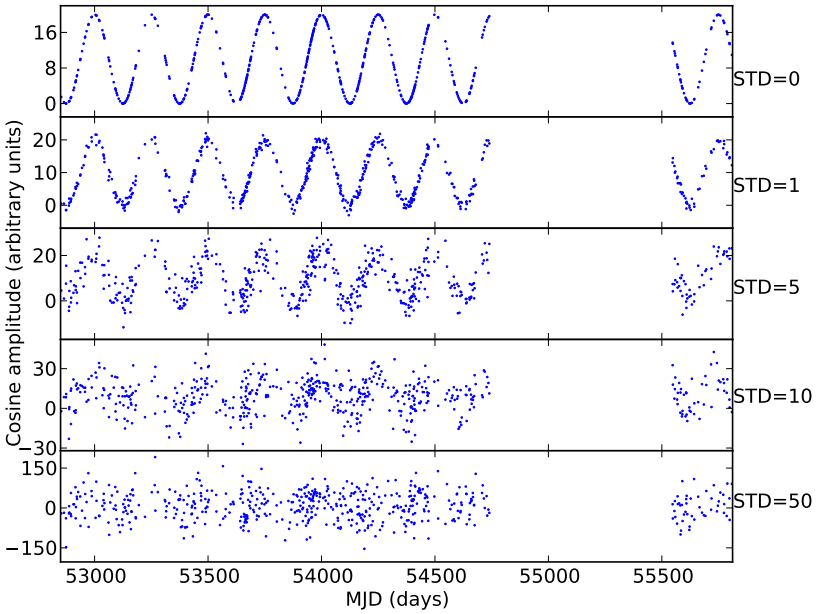

Figure 4.1: Simulated unevenly spaced time series. All these panels have equal periods of 250 days and an equal mean of zero, but different standard deviations for the noise. For each panel, the standard deviation of the Gaussian noise is given by the legend.

STD	LS (days)	EF (days)	EF error (days)
0	249.48	250.03	0.79
1	249.42	249.99	1.80
5	249.56	250.26	6.31
10	250.18	250.08	10.41
50	246.51	227.24	51.96

Table 4.1: Summary of the periods determined by the Lomb-Scargle (LS) and epoch-folding (EF) method for unevenly sampled simulated data. STD column shows the Gaussian standard deviation value which was applied to the time series.

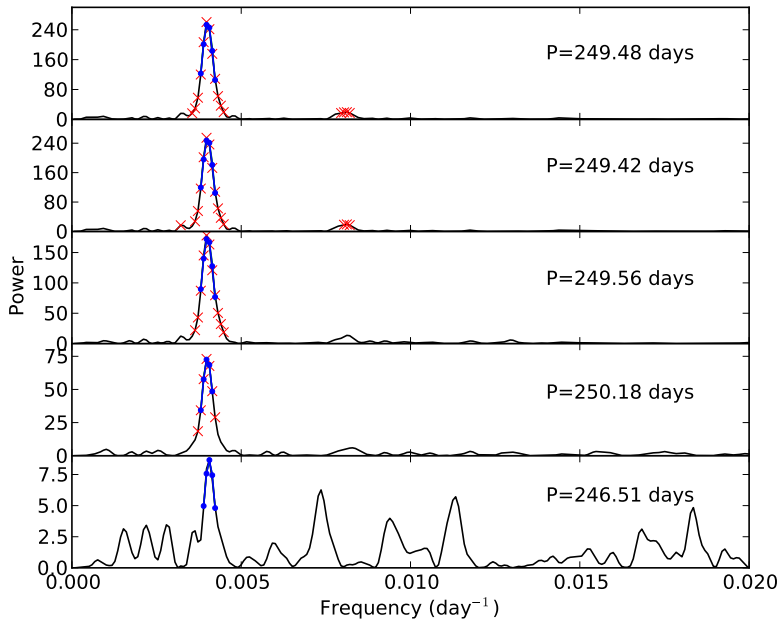

Figure 4.2: The Lomb-Scargle periodograms for all the simulated unevenly spaced data samples. The Gaussian noise standard deviations from the top panel down are: 0, 1, 5, 10 and 50. The inverse of the maximum peak is defined as the period of the time series. The stars are a test for the significance of the peak using the false alarm probability method (These are points greater than the value set to consider the peak to be significant). The period determined for each panel is marked as a legend and the solid line with dots (blue) on the peak is the fitted Gaussian function. A second-order polynomial was also fitted to the peak and this is shown by the solid line (green).

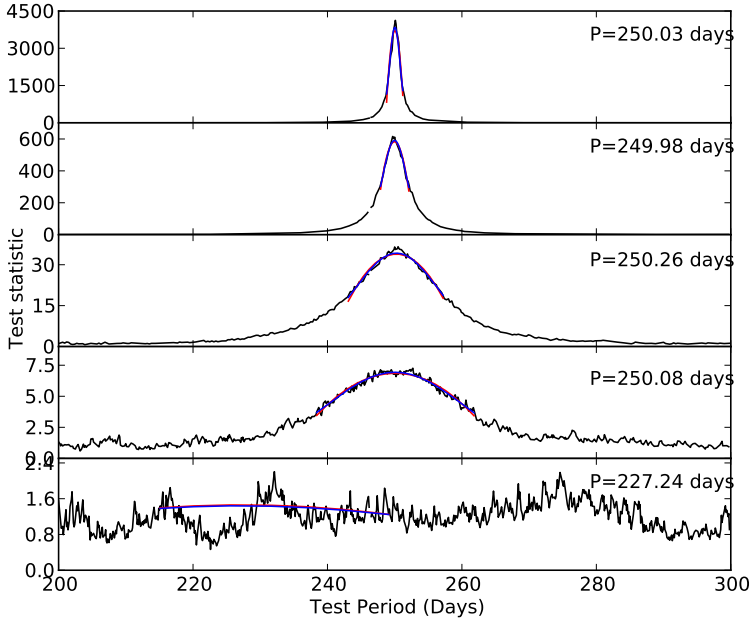

Figure 4.3: The L-statistics result for the epoch-folding method applied to the simulated time series. The second-order polynomial (solid line) and Gaussian function (solid line) were both fitted to the top of the peak data points to determine the period for each panel. The data were binned into 35 phase bins.

marised in Table 4.1. The Lomb-Scargle method detected the possibility of a period but it was not significant and the epoch-folding shows no period found.

4.6 The z-transform Discrete Correlation Function

In order to test for correlations and time delays between two time series, the z-transform Discrete Correlation Function (ZDCF) was used. It was developed to study the time delays and correlations for Active Galactic Nuclei (AGN). In this method, one time series is fixed and the other time series is moved across the fixed time series to check for correlation and phase lag.

It uses the cross-correlation function (CCF) and is commonly estimated by the interpolated cross-correlation function (ICCF) (Gaskell & Peterson, 1987) or by the discrete correlation function (DCF) (Edelson & Krolik, 1988). If x and y are two time series and their variance is given by V_x and V_y respectively, Blandford & McKee (1982) defined the cross-correlation function, with E being the expectation operator, as

$$CCF(\tau) = \frac{E\left[\left(x(t) - E_x\right)\left(y\left(t+\tau\right) - E_y\right)\right]}{\sqrt{V_x V_y}}, \tag{4.14}$$

where E_x is the expectation value in x, E_y is the expectation value in y and τ is the time lag (delay) between the two time series. Since our data are not evenly sampled, it implies that the Fourier analysis technique cannot be used directly on the time

series.

Alexander (1997) gave the estimate for the coefficient of the cross-correlation function for each bin, as

$$r(\tau) = \frac{1}{n} \sum_{\tau_{ij}} \frac{(x_i - \bar{x})\,(y_j - \bar{y})}{V_x V_y}, \tag{4.15}$$

where $\tau_{ij} \in bin$. The minimum data points in each bin should be at least 11 ($n_{min} = 11$) for the ZDCF to converge. The time delay $\tau = t_i - t_j$ is calculated for all possible ordered pairs of the x and y light curve, which can be then divided into n_{min} pair bins. The x and y series are assumed to be statistically stationary (meaning their statistical properties are constant, e.g. mean, variance, etc.). Also, the average of the light curve can be determined by integrating the light curve over time, which is called the ergodic statistical assumption, and the light curve is considered to have been randomly sampled. Equation 4.15 is skewed and is not a normal distribution. To correct for this behaviour, r can be transformed by Fisher's z-transform (Fisher, 1921).

$$z = \frac{1}{2} \ln \left(\frac{1 + r}{1 - r} \right). \tag{4.16}$$

Equation 4.16 implies r is quasi-normally distributed and that the mean $\bar{z}(r)$ and variance $V_z(r)$ are known. The r_{zdcf} was then defined by Alexander (1997) as

$$r_{zdcf}(\tau) = r^{+\left(\tanh\left(\bar{z}+\sqrt{V_z}\right)-r\right)}_{-\left(r-\tanh\left(\bar{z}-\sqrt{V_z}\right)\right)}. \tag{4.17}$$

This method was implemented in Fortran 77 by Alexander (1997). It was com-

piled and combined with the Python code to produce the plot and the time delay was determined by fitting a second-order polynomial function to the peak.

An interesting analytical derivation or simulations for future work on the ZDCF method would be to test how errors are propagated when using the ZDCF to make a comparison. To test this, we can use two time series with different periods and errors in the period, x, y, dx and dy days. This set up can help us determine the minimum time delay which will be significant.

Chapter 5

Results

5.1 Introduction

The spectra, time series, Lomb-Scargle periodograms, epoch-folding results and z-transform Discrete Correlation Function results for a control source, an irregularly varying source and the periodic or quasi-periodic sources are shown and explained.

For the new methanol maser source regions from the MMB survey catalogues I and II, the spectra, time series, and the Lomb-Scargle periodograms of G8.872-0.493 and G358.460-0.391 are shown.

In all time series, there was a long-term variations. The long-term variations are the slow changes which were observed over the monitoring window. Some were linear increase, some increased slowly to reach the maximum, then decrease. Within these long-term variations, there were short-term variations. The short- and long-term variations are due to astrophysical activities in the masing regions. In order to determined the period in the time series, the long-term variations were removed by subtracting the best fitted mathematical function. Sometimes the time series were segmented in order to find remove the long-term variations.

The long-term variations can be considered periodic if several cycles are observed.

5.2 Control source

G351.42+0.64 was used as a control source as it is bright and it has small variation range in both 6668-MHz and 12178-MHz maser transitions (Goedhart et al., 2009). If there is a step change due to fault in the telescope and the Point Source Sensitivity (PSS) is incorrect then it will be observed in the G351.42+0.64 time series.

5.2.1 G351.42+0.64

The G351.42+0.64 at 6668-MHz spectra are shown in Figure 5.1. This figure compares the spectra before and after the 26-m HartRAO telescope bearing failure. In both plots, there are the upper (dotted line), average (solid line) and lower (dash dot line) envelopes which hold information about the variation range of the maser emissions over the monitoring period. In order to see the kind of variations, the time series have to be made by concatenating the spectra over the monitoring period and extracting the flux density of the maser peaks in the spectra. The peak around -9.8 km.s^{-1} has become brighter.

Time series were produced for nine maser peaks at 6668-MHz (Figure 5.2). The gap (54750-55600 MJD) in all the time series including other sources for the period when the HartRAO bearing failed.. All show weak variations, and the -9.810, -9.766, -9.239, -8.667, -7.966 and -7.439 km.s^{-1} time series show the two flares between 53700-54200 MJD.

After removing long-term variations from all the selected time series for G351.42+0.64 at 6668-MHz, the Lomb-Scargle periodograms (Figure 5.3) were produced. The similar method was applied to other sources and the order of polynomial

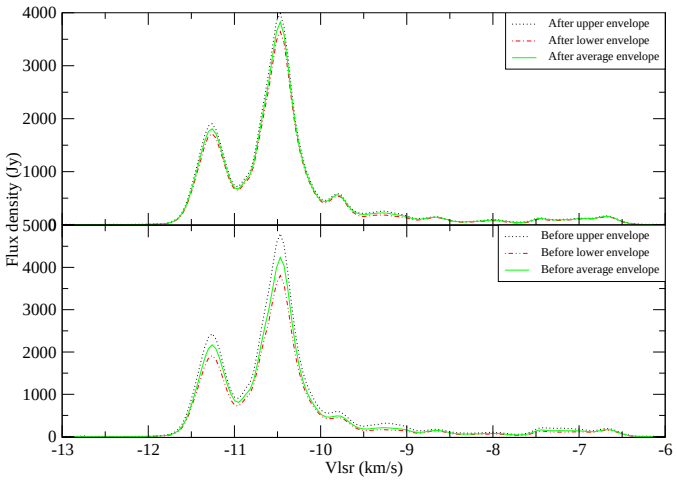

Figure 5.1: Methanol spectra for G351.42+0.64 at 6668-MHz before and after the bearing failure.

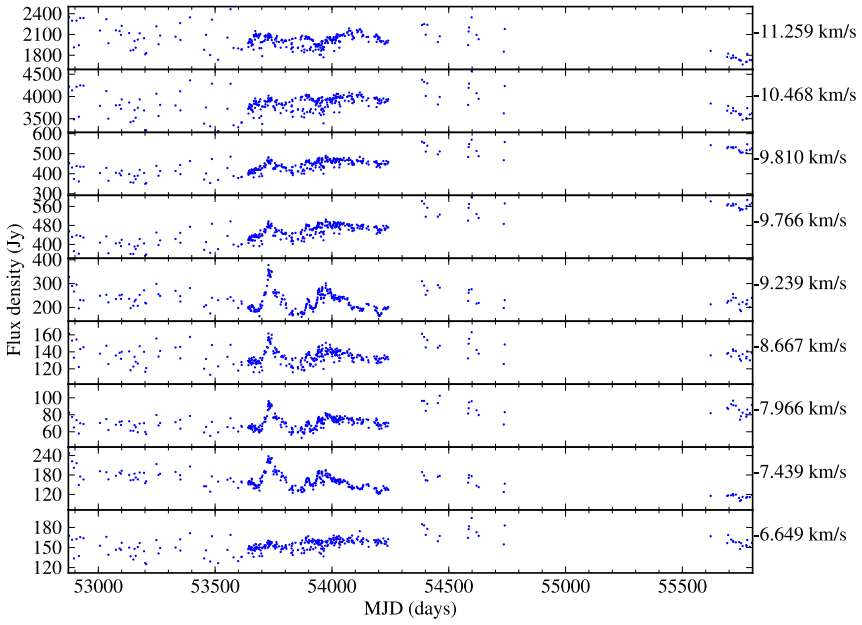

Figure 5.2: Time series for G351.42+0.64 at 6668-MHz.

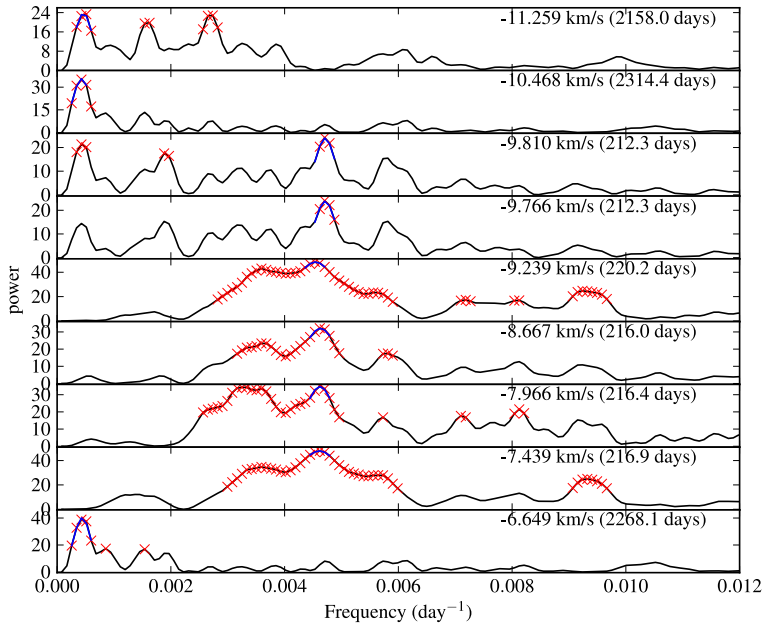

Figure 5.3: Lomb-Scargle periodograms for G351.42+0.64 at 6668-MHz.

was different from one time series to another. The periodograms for the -9.766, -9.239, -8.667, -7.966 and -7.439 km.s^{-1} time series have significant peaks which are due to the two peaks in their time series.

The correlations and time delays for G351.42+0.64 at 6668-MHz are shown in Figure 5.4 and it was tested by the ZDCF (Alexander, 1997). The data between 53500 and 54300 MJD, covering the two flares were selected for the time series at -9.810, -9.239, -8.667, -7.966 and -7.439 km.s^{-1}. The time delays ranges from 0 to 4 days. The negative (-) and positive (+) in the time delays hold information about which time series is delayed. For an example, if A time series is compared with B time series and has negative (-) time delays then A arrives first. In contrast, positive (+)time delays would mean B arrives first.

The spectra for G351.42+0.64 at 12178-MHz are shown in Figure 5.6. To study variations over the monitoring period, the maser peaks at -11.327, -10.991, -10.510,

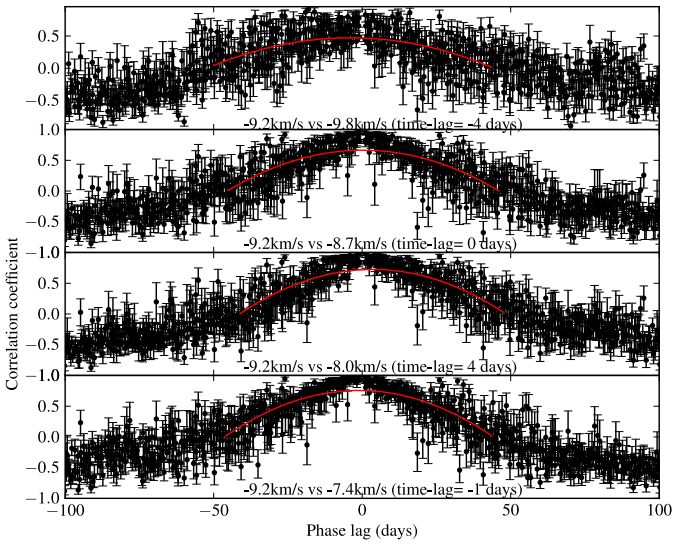

Figure 5.4: The correlations and time delays for G351.42+0.64 at 6668-MHz using the ZDCF method (see section 4.6). The time delays range from 0-4 days. These results are for the time series between 53700-54200 MJD.

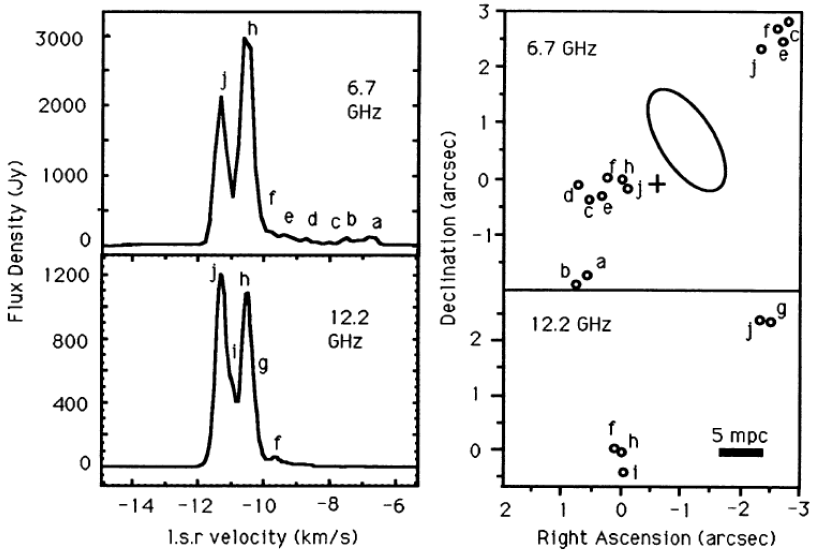

Figure 5.5: The interferometry spectra and maser spot maps for G351.42+0.64 at both 6668 and 12178-MHz (Norris et al., 1993). The cross in the maser spots for the 6668-MHz emission line is the continuum peak and the ellipse approximates the position of the OH maser.

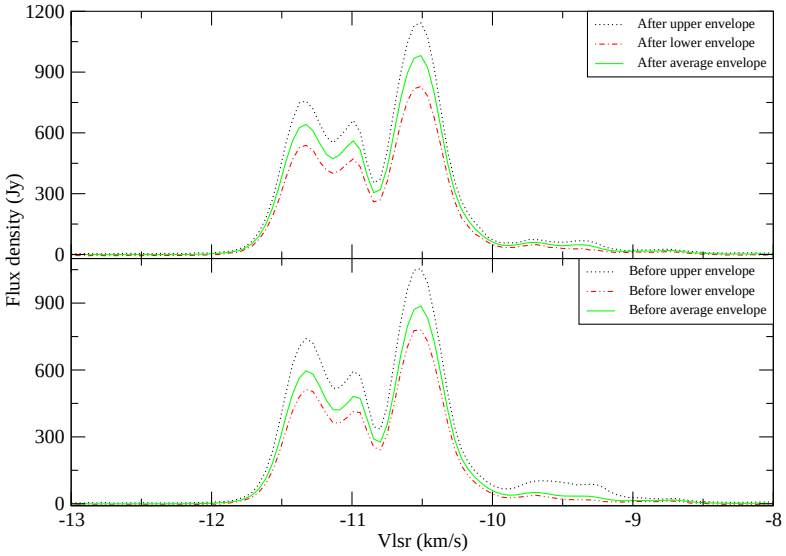

Figure 5.6: Methanol spectra for G351.42+0.64 at 12178-MHz before and after the bearing failure.

-9.692 and -9.356 km.s^{-1} were selected and their time series are shown in Figure 5.7.

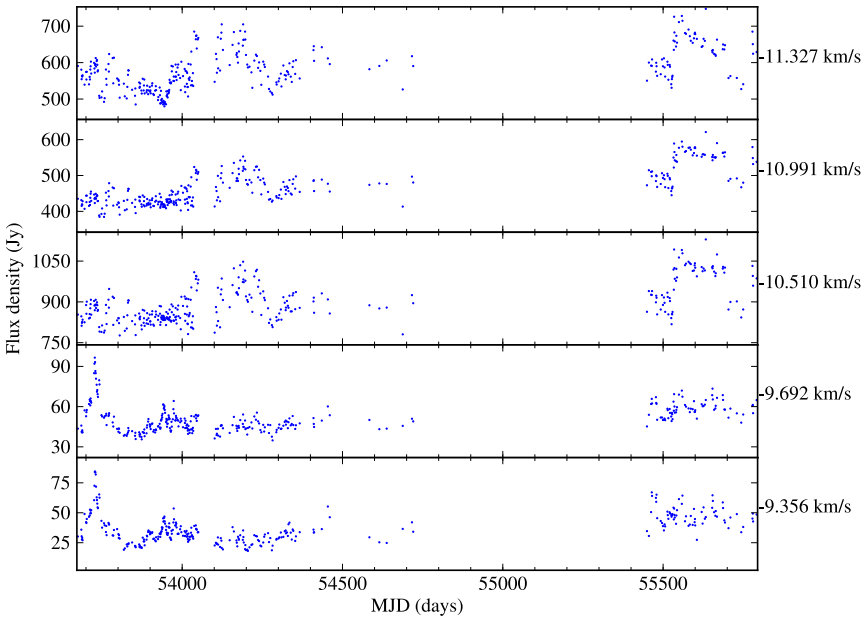

Figure 5.7: Time series for G351.42+0.64 at 12178-MHz.

The Lomb-Scargle periodograms for these time series are shown in Figure 5.8. In

the periodograms there are multiple peaks of similar probability which implies that they are the signatures of random variations. For conclusive evidence of the periodicity, several cycles should be observed. The data after the bearing was repaired for the three brightest peaks (which are: 11.327 (j), 10.001 (i) and 10.510 (h) km.s^{-1}, see Figures 5.5 and 5.6) show a flare which decays slowly, whereas the other time series show no significant variations.

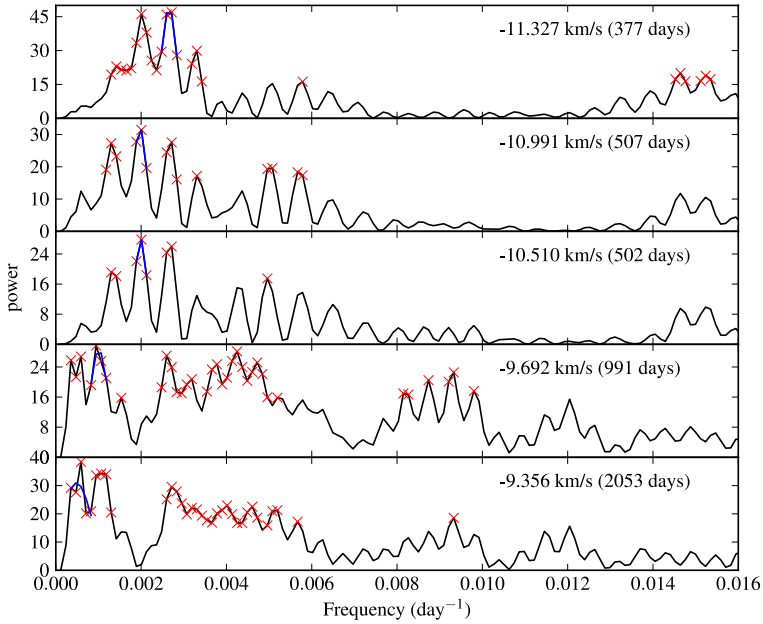

Figure 5.8: Lomb-Scargle periodograms for G351.42+0.64 at 12178-MHz.

The interferometric spectra and maser spot maps for G351.42+0.64 at both 6668 and 12178-MHz are shown in Figure 5.5. The spectra shown in Figure 5.1 and 5.6 are slightly different compared with the spectra by Norris et al. (1993).

If the maser spots shown in Figure 5.5 have not changed their locations or distributions, then both the 6668-MHz and 12178-MHz maser peaks coincide with their corresponding interferometric maser spots. The maser spots at h and j are very close to the continuum peak and they are the brightest peaks in the spectrum. The

flare is observed in the time series of the maser peaks between -10.0 and -7.0 km.s^{-1} which are: b, c, d, e and f maser spots in Figure 5.5. These maser spots are further out from the parent young massive stellar object or continuum source, but i and j maser spots are closer to the parent young massive stellar object or continuum source. This could be due to the variations of the environment, if the protostar coincides with the continuum peak's position. If it was from background radiation and the source of the flare is isotropic, then all the maser peaks should have shown a flare.

5.3 The irregularly varying source

5.3.1 G351.78-0.54

The spectrum for G351.78-0.54 at 6668-MHz is shown in Figure 5.9. The difference between the upper and lower envelopes of these spectra is significant different. There are new weak peaks between -2.0 and -1.0 km.s^{-1} but they are too weak for time series analysis. The maser peak around the -0.535 km.s^{-1} has become brighter but the upper and lower envelopes are close to each other which implies a small variation range with an increased intensity. This source is a good example of the long-term evolution of methanol maser spectra.

The time series at -2.704, -0.535, 0.989, 1.275, 1.634 and 1.888 km.s^{-1} are shown in Figure 5.10. They have the data from the HP1000 minicomputer (hereafter referred to as HP data) and data from the New Control Computer System (hereafter referred to as NCCS data). The first gap (54750-55600 MJD) separates the HP and NCCS data. The second gap in NCCS data for the two year gap (54750 - 55600

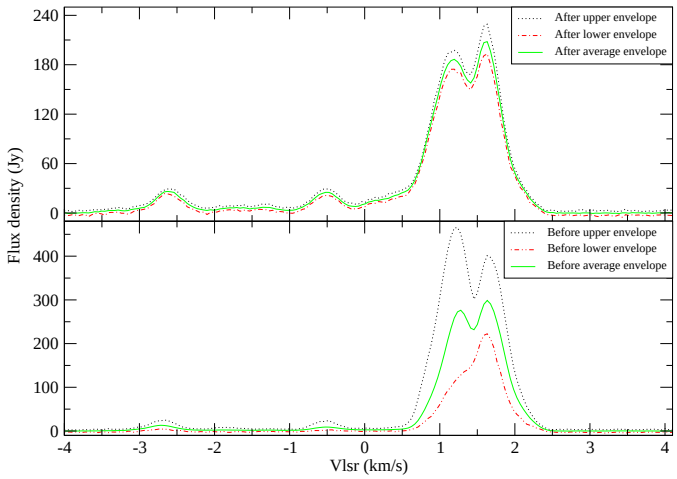

Figure 5.9: Methanol maser spectra for G351.78-0.54 at 6668-MHz before and after the bearing failure.

MJD) when the 26-m HartRAO radio telescope bearing failed.

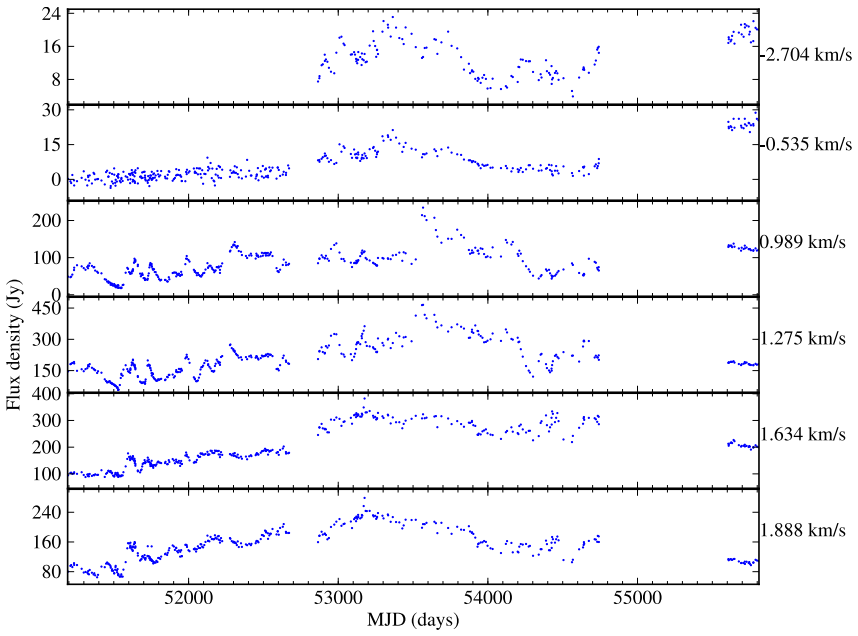

Figure 5.10: Time series for G351.78-0.54 at 6668-MHz.

The time series at -2.704 km.s^{-1} shows a gap (526800 - 528500 MJD) in the HP1000 minicomputer epoch. The maser peak at the -2.704 km.s^{-1} velocity was

cut out due to the chosen bandwidth being small.

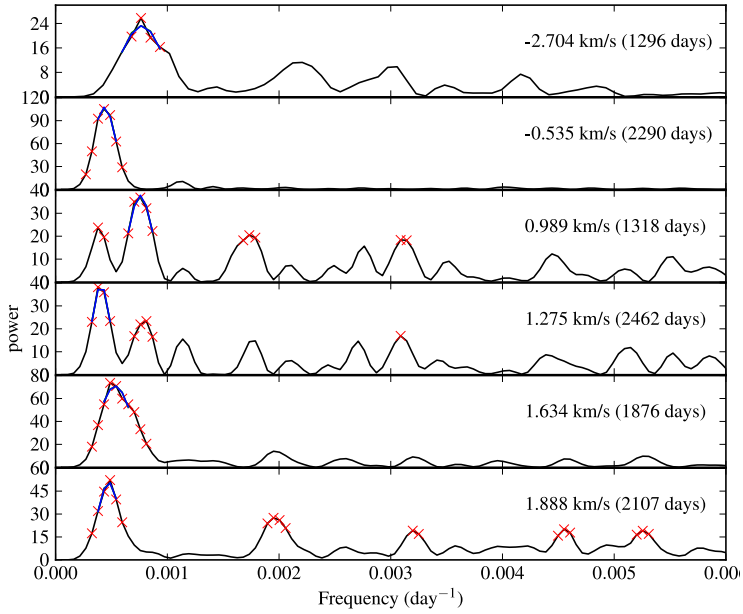

Figure 5.11: Lomb-Scargle periodograms for G351.78-0.54 at 6668-MHz.

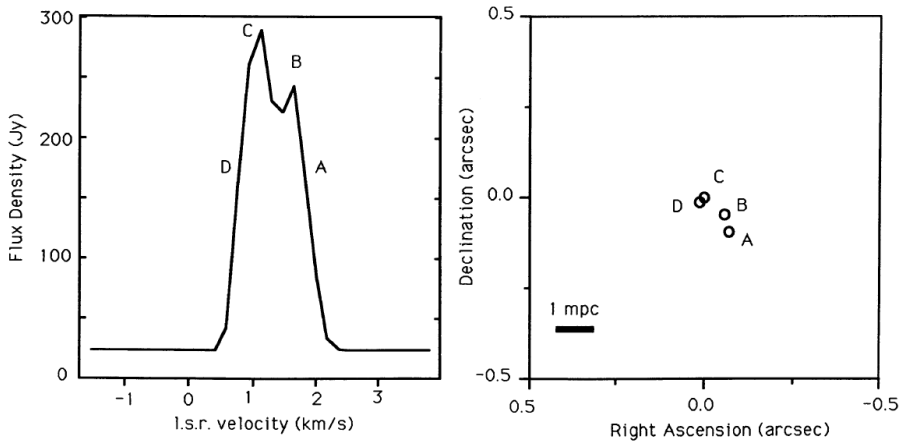

Figure 5.12: The interferometry spectra and maser spot maps for G351.78-0.54 at 6668-MHz (Norris et al., 1993).

For the -0.535 km.s^{-1} peak, the HP data segment shows weak variation. The time series for the D, C and B maser spots (Figure 5.12) are shown in Figure 5.10

as 0.989, 1.275 and 1.88 km.s^{-1} time series respectively. The C and D maser spots are very close to each other and show correlated variability.

It appears that maxima in the time series are random amplifications by the masers of the background radiation or the local environment. The Lomb-Scargle (Figure 5.11) method was tried on the time series, but the great challenge is de-trending the time series. The time series were tested for all possible periods after removing long-term linear characteristics. A third order polynomial function was used for de-trending the data. The peaks are due to the long-term variations even after de-trending the data. A third order polynomial function can also introduce variations into the data because the long-term variations are not a perfect polynomial function.

5.4 Periodic or quasi-periodic sources

5.4.1 G9.62+0.20E

The spectra for G9.62+0.20E at 6668-MHz are shown in Figure 5.13. There has been no significant change in the spectra. The time series were produced for maser peaks at -0.881, -0.222, 1.227, 1.798, 3.071 and 5.529 km.s^{-1} (Figure 5.14). There are discontinuities in the time series going from 256-channel (HP) spectrometer to 1024 channel (NCCS) spectrometer owing to the difference in channel spacing and width.

The -0.881, -0.222 and 1.227 km.s^{-1} masers have shown a steady increase and the amplitude of the variations has increased. The 3.071 km.s^{-1} maser has decreased in intensity.

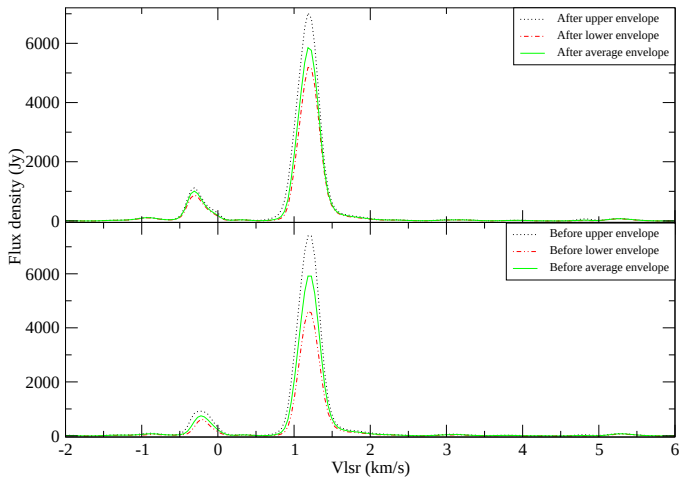

Figure 5.13: Methanol maser spectra for G9.62+0.20E at 6668-MHz before and after the bearing failure.

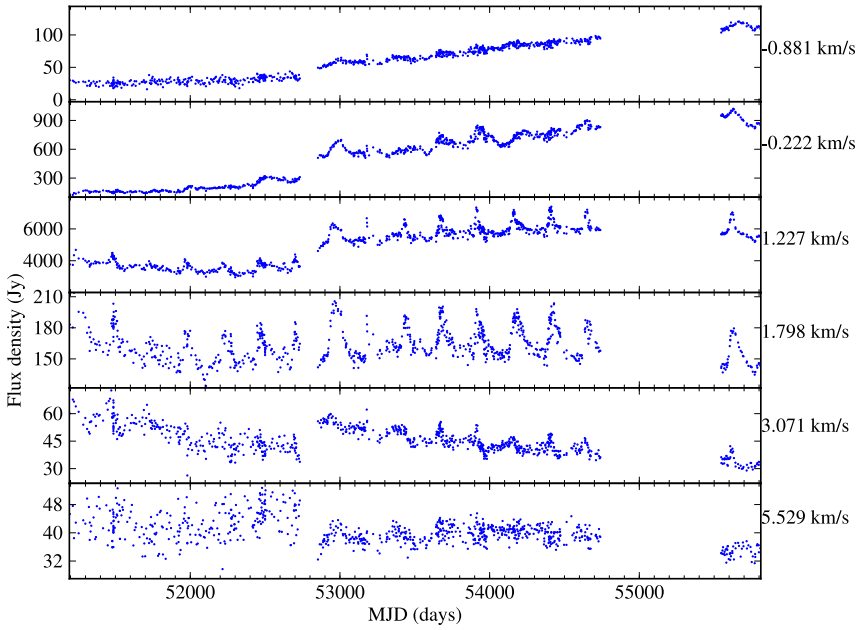

Figure 5.14: Time series for G9.62+0.20E at 6668-MHz.

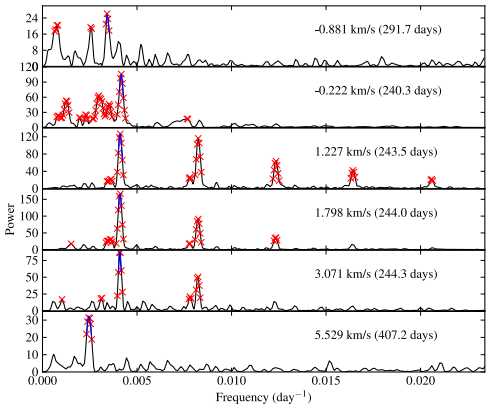

Figure 5.15: Lomb-Scargle periodograms for G9.62+0.20E at 6668-MHz.

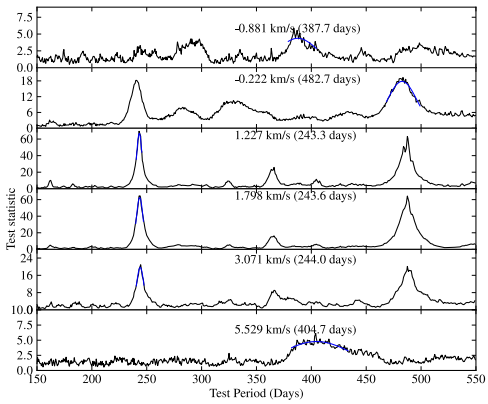

Figure 5.16: epoch-folding results for G9.62+0.20E at 6668-MHz.

Vel.	LS (days)			EF (days)			EF error (days)		
(km.s^{-1})	All	HP	NCCS	All	HP	NCCS	All	HP	NCCS
-0.881	291.7	388.6	276.7	387.7	-	-	18.3	-	-
-0.222	240.3	473.9	240.5	240.7	-	240.7	5.5	-	7.0
1.227	243.5	250.9	242.9	243.3	245.5	242.9	2.5	7.6	3.5
1.798	244.0	250.8	243.0	243.6	247.8	243.1	3.1	9.8	4.5
3.071	244.3	243.1	245.6	244.0	245.2	244.8	3.3	11.7	6.0
5.529	407.2	391.5	412.1	404.7	-	-	32.7	-	-

Table 5.1: Periods determined using the Lomb-Scargle and epoch-folding methods for G9.62+0.20E at 6668-MHz.

After de-trending the time series for G9.62+0.20E at 6668-MHz, the Lomb-Scargle and epoch-folding methods were applied to search for and to test the significance for the periods. All of the time series show regular variations, but the periods for the -0.881 and 5.529 km.s^{-1} peaks were not reliable values (Table 5.1).

The maser peaks at 1.227 and 1.798 km.s^{-1} have the best determined periods in the HP and NCCS data. The period determined for the -0.222 km.s^{-1} time series in HP data (see Table 5.1) is due to strong waveform at the end of HP data epoch (see Figure 5.14).

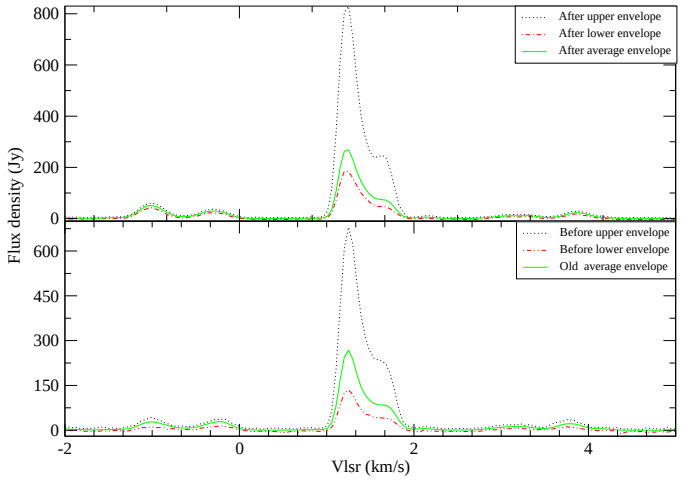

Figure 5.17: Methanol maser spectra for G9.62+0.20E at 12178-MHz before and after the bearing failure.

The spectra for G9.62+0.20E at 12178-MHz are shown in Figure 5.17. They show no significant evolution. Five maser peaks were selected for time series analysis and they are at: -1.028, -0.234, 1.256, 1.631 and 3.792 km.s^{-1} (Figure 5.18).

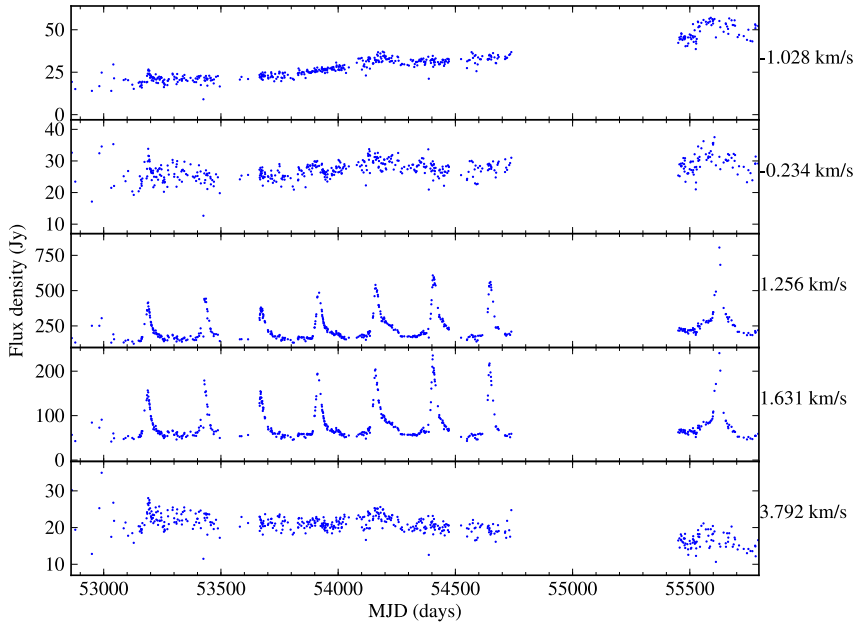

Figure 5.18: Time series for G9.62+0.20E at 12178-MHz.

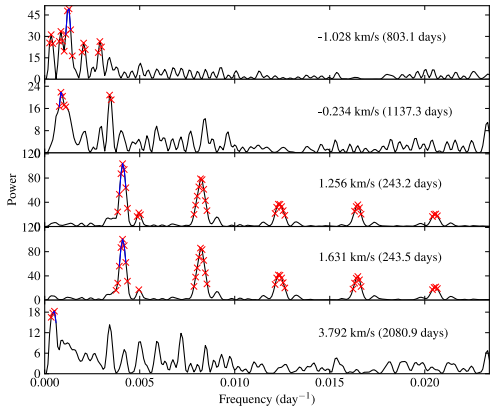

Figure 5.19: Lomb-Scargle periodograms for G9.62+0.20E at 12178-MHz.

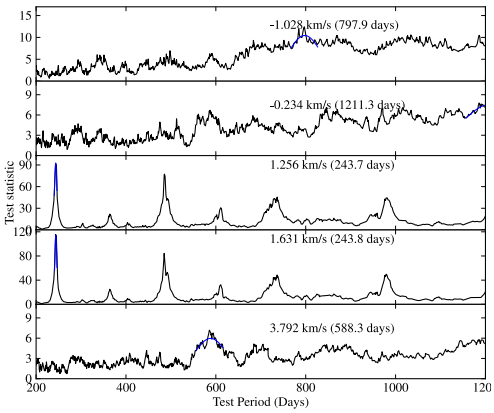

Figure 5.20: epoch-folding results for G9.62+0.20E at 12178-MHz.

The 1.256 and 1.631 km.s^{-1} time series in Figure 5.18 show strong regular variations. The flares have different intensities and are periodic. The shape of the flare is not entirely consistent. Taking a closer look at the time series, the behaviour is not entirely smooth as it increases towards the local maximum. This behaviour is also observed as the time series decreases to its local minimum. This behaviour started from around 53250.0 MJD and it becomes stronger on the last flare.

After removing the trends in these time series, the Lomb-Scargle and epoch-folding methods were used to search for and test the significance of the period. The Lomb-Scargle periodograms are shown in Figure 5.19 and the epoch-folding results are shown in Figure 5.20. Strong periodic behaviour is observed in the 1.256 and 1.631 km.s^{-1} time series. The periodograms for these peaks also have harmonics.

Vel. (km.s^{-1})	L-S (days)	E-F (days)	E-F error (days)
1.256	243.2	243.8	2.8
1.631	243.5	243.7	2.4

Table 5.2: Periods determined using the Lomb-Scargle and epoch-folding methods for G9.62+0.20E at 12178-MHz.

Table 5.2 summarises the periods determined for the 1.256 and 1.631 km.s^{-1} time series . For both time series, the periods determined are consistent and the calculated width for the epoch-folding is also consistent.

These two maser peaks show strong correlations as shown by the ZDCF results in Figure 5.21. The time delay was determined by fitting a second-order polynomial to the peak, and it is 1.6 days. The time delay is not significant.

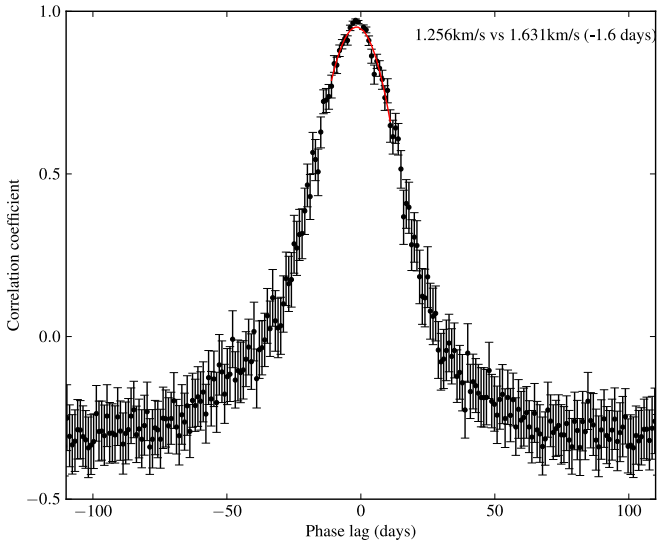

Figure 5.21: The correlation and time delay between the 1.256 and 1.631 km.s^{-1} time series for G9.62+0.20E at 12178-MHz.

5.4.2 G12.89+0.49

The spectra for G12.89+0.49 at 6668-MHz are shown in Figure 5.22 and show significant variation. Both diagrams have the two brightest peaks at around 39 and 34 km.s^{-1}. The peak around 31.5 km.s^{-1} has become weaker.

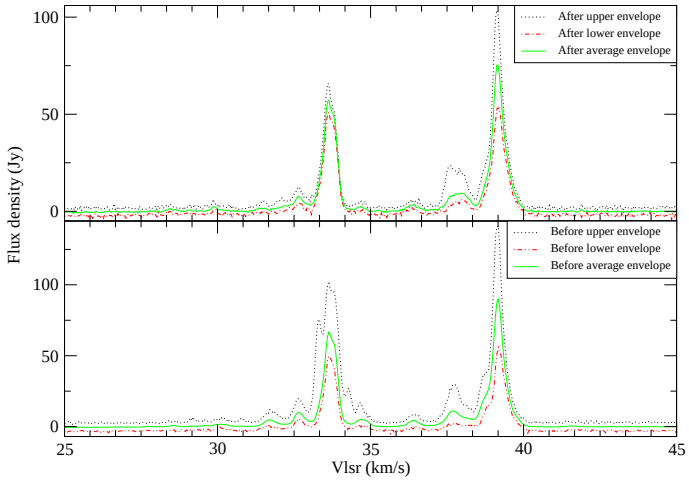

Figure 5.22: Methanol maser spectra for G12.89+0.49 at 6668-MHz.

Due to a technical problem, the observations for this source after the bearing replacement were not properly sampled. It has been reported to have a period of about 29.5 days by Goedhart et al. (2009).

The spectra for G12.89+0.49 at 12178-MHz are shown in Figure 5.23. The diagrams are similar. One maser peak was used to produce the time series and is at 39.231 km.s^{-1}.

The time series for the 39.231 km.s^{-1} maser peak was created from the concatenated G12.89+0.49 spectra at 12178-MHz (Figure 5.24). The first plot in Figure 5.24 gives the complete time series for the 39.231 km.s^{-1} maser peak and the rest of the plots are the expanded segments of the time series.

The Lomb-Scargle periodograms (Figure 5.25) and epoch-folding results (Figure

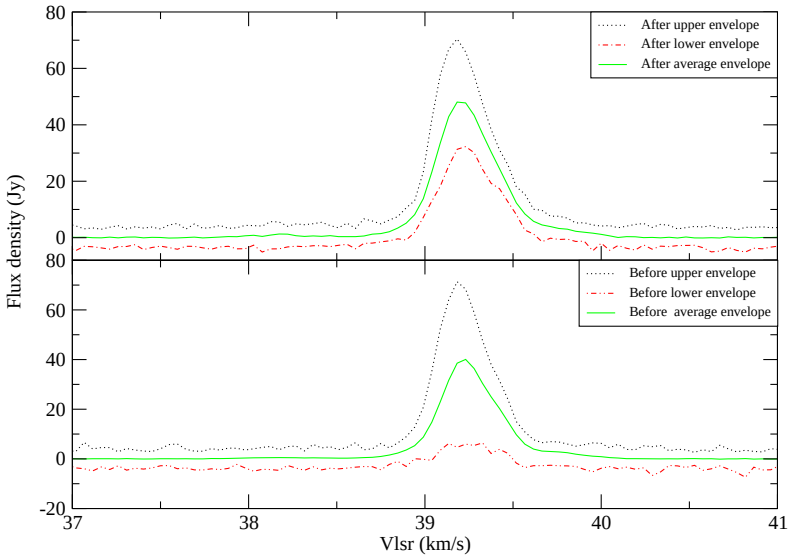

Figure 5.23: Methanol spectra for G12.89+0.49 at 12178-MHz before and after the bearing failure.

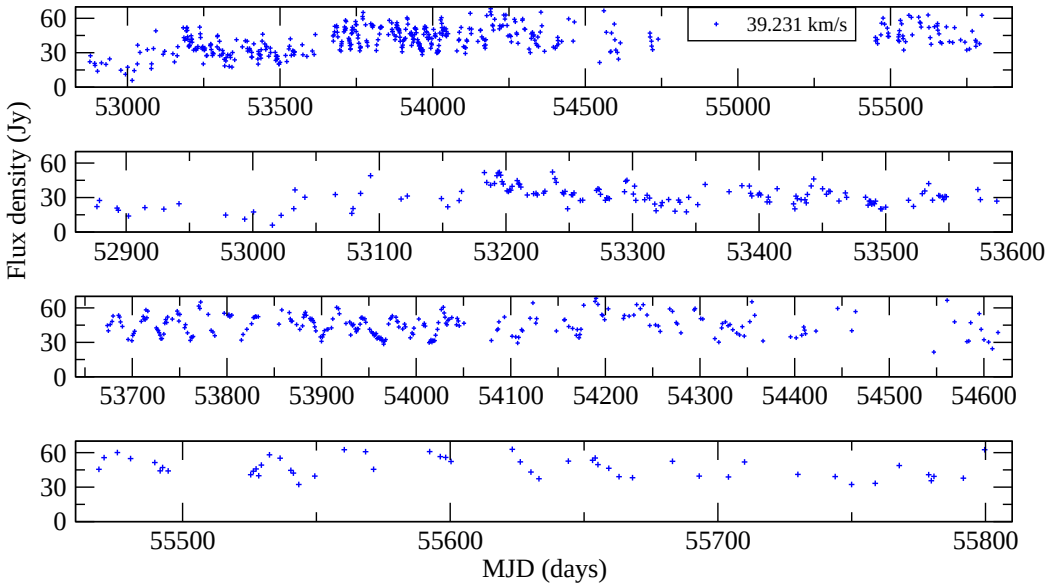

Figure 5.24: Time series for G12.89+0.49 at 12178-MHz. The time series in the top diagram was expanded in the other three time series diagrams. The bottom diagram is for the data collected after the bearing was repaired.

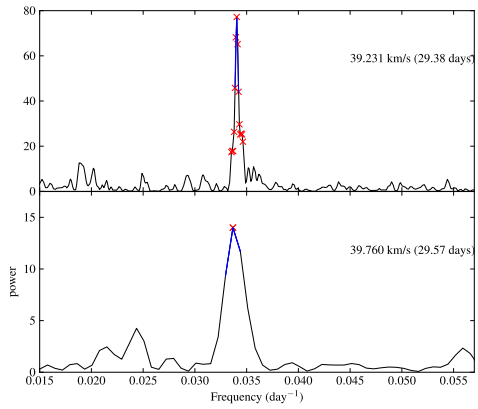

Figure 5.25: Lomb-Scargle periodograms for G12.89+0.49 at 12178-MHz. The lower panel is the periodogram for the time series after the bearing was fixed.

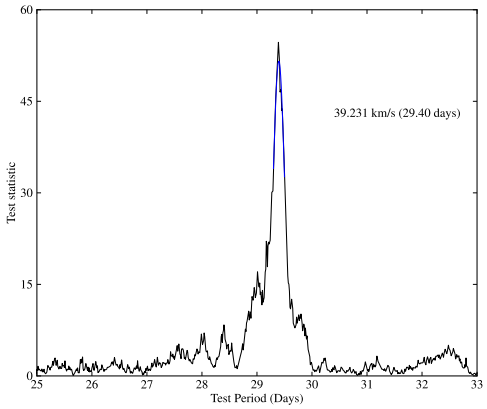

Figure 5.26: epoch-folding result for G12.89+0.49 at 12178-MHz.

5.26) show that G12.89+0.49 is periodic at 12178-MHz. The period determined is consistent at 29.4 days using both methods. Since the Lomb-Scargle method is not very sensitive to the size of the data sample, the periodogram for the whole time series and separated section of the time series were produced to check the evolution of the period. These are shown in Figure 5.25. The upper panel is for the complete time series, the lower panel is for the data after the bearing was repaired. The average period is 29.4 days.

Vel. (km.s^{-1})	L-S (days)	E-F (days)	E-F error (days)
39.231	29.38	29.40	0.11

Table 5.3: Periods determined using the Lomb-Scargle and epoch-folding methods for G12.89+0.49 at 12178-MHz.

This source has the shortest period of 29.40 ± 0.11 days and it still shows periodic behaviour.

5.4.3 G188.95+0.89

The top and bottom panels in Figure 5.27 show the spectra for G188.95+0.89 at 6668-MHz. The maser peaks at 8.419, 9.648 and 10.702 km.s^{-1} have become stronger and the other peaks (10.087, 10.439 and 11.404 km.s^{-1}) are now weaker.

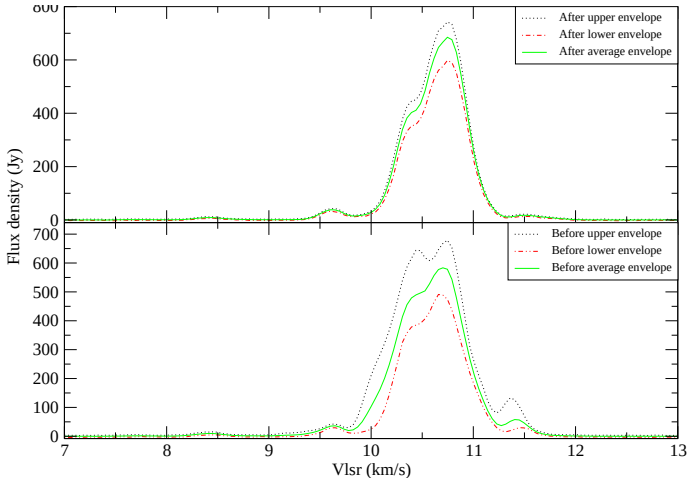

Figure 5.27: Methanol maser spectra for G188.95+0.89 at 6668-MHz before and after the bearing failure.

The time series were produced using the 8.419, 9.648, 10.08, 10.439, 10.702 and 11.404 km.s^{-1} maser peaks (Figure 5.28).

The 8.419 km.s^{-1} time series shows no variation in the HP data. For the NCCS data, it shows a weak counterpart to the variations seen in the other time series.

The 9.648, 10.087, 10.439, 10.702 and 11.404 km.s^{-1} time series start with a long-term increase in flux density, coupled with a periodic variation. Some of these time series continue to rise in flux density while others reach maximum and then start to decay. The time series at 9.648 and 10.702 km.s^{-1} increased throughout the monitoring period. The other time series started to decrease after reaching a global maximum over our monitoring window. The waveform of the regular behaviour has

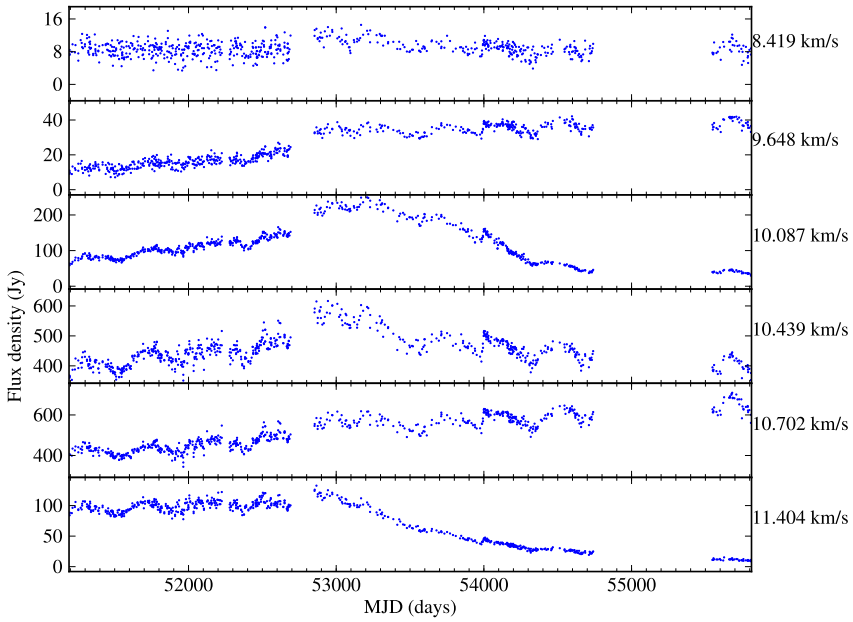

Figure 5.28: Time series for G188.95+0.89 at 6668-MHz.

evolved over the monitoring period. At the beginning of the monitoring window the waveform resembles a sinusoid but it evolved later to a new shape which rises faster than its decay rate. Around 54000 MJD, there is a flare in all the selected time series.

The 11.404 km.s^{-1} time series shows an exponential decay. This was confirmed by fitting an exponential function to the data when it started to decay. A second-order polynomial was also fitted to the time series for comparison. The results of the fits are shown in Figure 5.29. The exponential function is a better fit, with an e-folding time of 1271 days.

All time series were de-trended before searching for the existence of the periods. The results for the period search using the Lomb-Scargle and epoch-folding methods are shown in Figure 5.30 and 5.31 respectively.

The summary of the periods determined for all data, HP and NCCS data, is

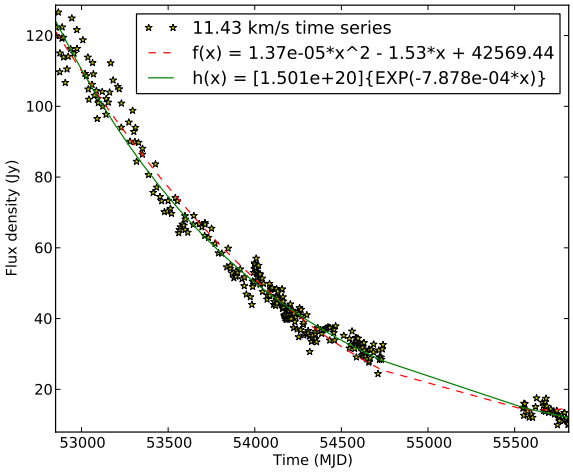

Figure 5.29: The 11.404 km.s^{-1} NCCS data time series for G188.95+0.89 at 6668-MHz. The dashed line is for a second-order polynomial fit and the solid line is for an exponential fit to the time series.

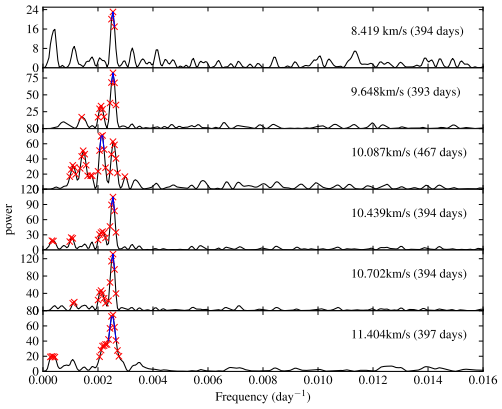

Figure 5.30: Lomb-Scargle periodograms for G188.95+0.89 at 6668-MHz.

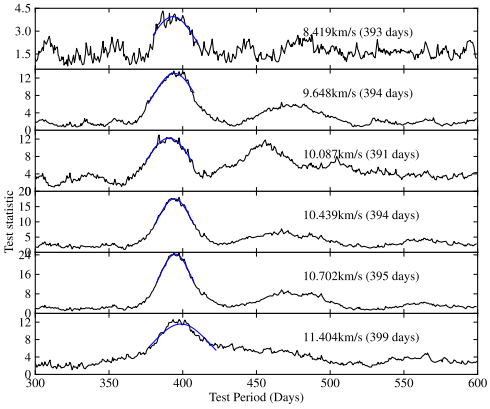

Figure 5.31: epoch-folding results for G188.95+0.89 at 6668-MHz.

Vel.	LS (days)			EF (days)			EF error (days)		
km.s^{-1}	All	HP	NCCS	All	HP	NCCS	All	HP	NCCS
8.419	394	-	397	393	-	397	15	-	23
9.648	391	426	393	394	439	394	14	35	28
10.087	389	432	397	391	434	403	15	38	26
10.439	394	423	398	394	429	398	12	46	25
10.702	395	421	393	395	426	392	11	37	25
11.404	397	407	390	399	410	378	20	33	40

Table 5.4: Periods determined using the Lomb-Scargle and epoch-folding methods for G188.95+0.89 at 6668-MHz.

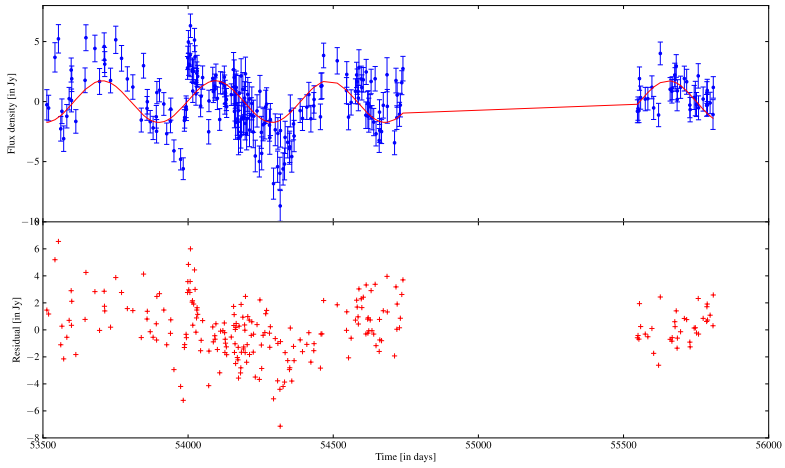

Figure 5.32: Sum of sine and cosine functions with 389.7 day period fitted to the 11.404 km.s^{-1} time series.

given in Table 5.4. The periods in the HP data are substantially longer than those for the NCCS data only and the combined(NCCS and HP) data for all maser peaks. This suggests evolution of the periods.

The time series at 11.404 km.s^{-1} was tested for periodicity during its decay, with the Lomb-Scargle method after subtracting the fitted exponential function. This gave a frequency of 0.0026 cycle per day (390 day period). The sum of the sine and cosine functions with a 390 day period was fitted to the de-trended time series (Figure 5.32). The fit confirms that there are weak periodic variations during the exponential decay segment for the 11.404 km.s^{-1} time series.

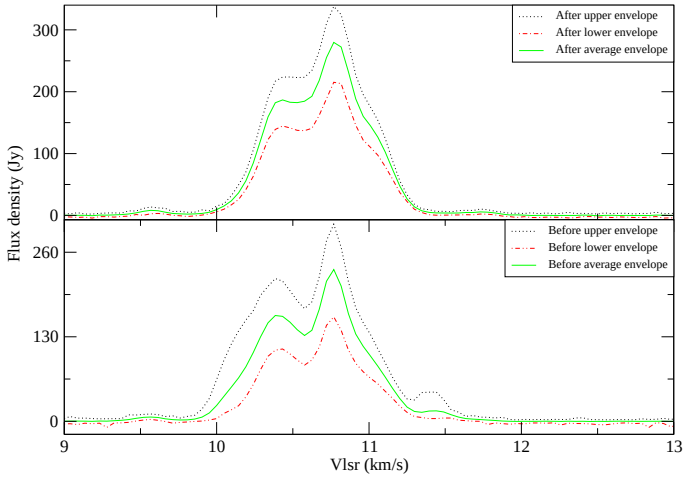

Figure 5.33: Methanol maser spectra for G188.95+0.89 at 12178-MHz before and after the bearing failure.

The spectra for G188.95+0.89 at 12178-MHz are shown in Figure 5.33, indicating substantial differences before and after the bearing failure. The time series for all the selected peaks are shown in Figure 5.34.

The time series at 10.192 and 11.394 km.s^{-1} show a decay which is coupled with short-term variations. The decay for both time series were well fitted with an exponential function (Figure 5.35). The maser peak at 10.192 km.s^{-1} shows weak

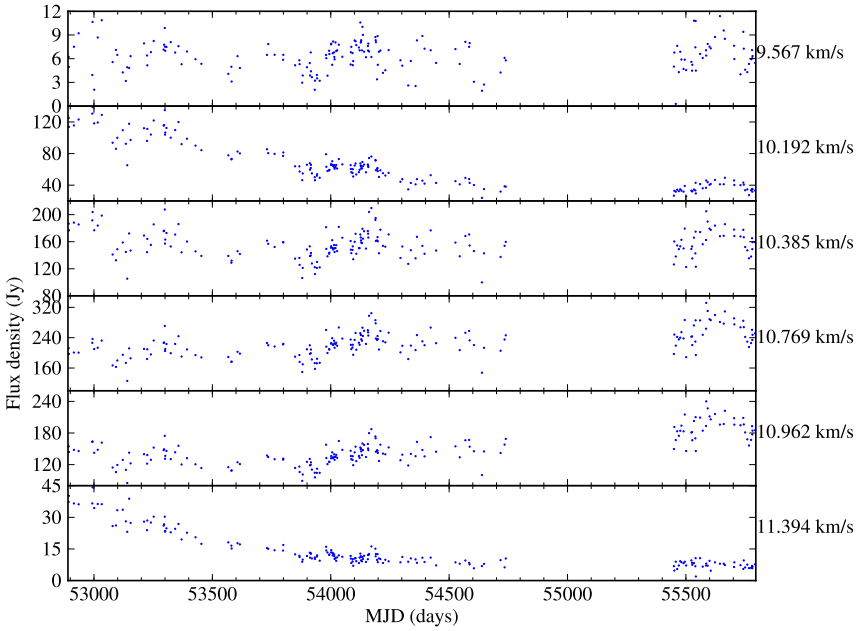

Figure 5.34: Time series for G188.95+0.89 at 12178-MHz.

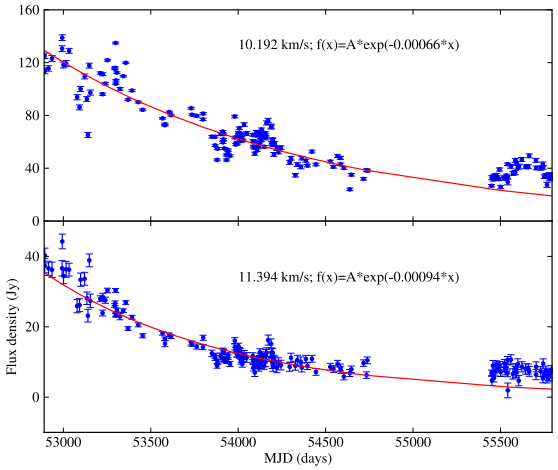

Figure 5.35: Exponential fit to the 10.192 and 11.394 km.s^{-1} time series for G188.95+0.89 at 12178-MHz. The exponential function was fitted to the data before the bearing failure ($<$ 55000 MJD).

regular variations during the exponential decay, and has an e-folding time of 1515 days. The 11.394 km.s^{-1} time series has a 1064 day e-folding decay time.

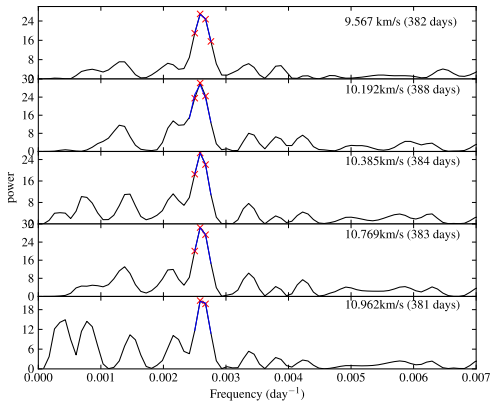

Figure 5.36: Lomb-Scargle periodograms for G188.95+0.89 at 12178-MHz.

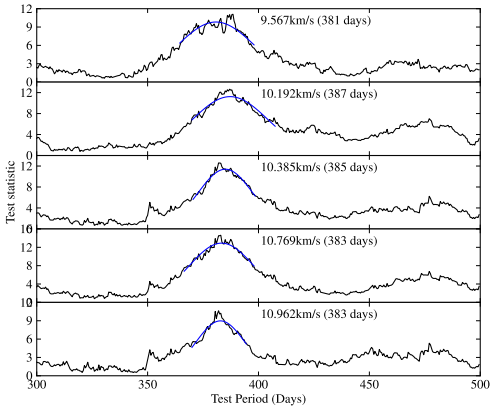

Figure 5.37: epoch-folding results for G188.95+0.89 at 12178-MHz.

After removing the long-term variations in the time series for G188.95+0.89 at 12178-MHz, the Lomb-Scargle (Figure 5.36) and epoch-folding (Figure 5.37) methods were used to find periods in the time series. All the time series show the existence of periods, except for the 11.394 km.s^{-1} time series. The results are summarised in Table 5.5. There is a difference in the periods determined between 6668-MHz and 12178-MHz (see Tables 5.4 and 5.5). When the uncertainties associated with the periods determined are taken into consideration, these differences (in the periods) are not significant.

5.4.4 G328.24-0.55

The spectra for G328.24-0.55 at 6668-MHz are shown in Figure 5.38. There is a new maser peak at -31.824 km.s^{-1}. Twelve maser peaks were selected for the time series analysis (Figures 5.39 and 5.40). The -49.605 and -48.771 km.s^{-1} time series show

Vel. (km.s^{-1})	LS (days)	EF (days)	EF error (days)
9.567	382	381	18
10.192	388	387	17
10.385	384	385	12
10.769	383	383	15
10.962	381	383	11

Table 5.5: Periods determined using the Lomb-Scargle and epoch-folding methods for G188.95+0.89 at 12178-MHz.

different behaviour for the data after the bearing replacement. There is a flare at 53250 MJD for all the time series. The -34.941 km.s^{-1} time series shows a linear long-term increase in flux density for the data before the bearing failure. The data after the bearing was repaired show a decrease in long-term variation. The maser peak at -31.824 km.s^{-1} shows a slow rise and quick decay which was not there before the bearing failure.

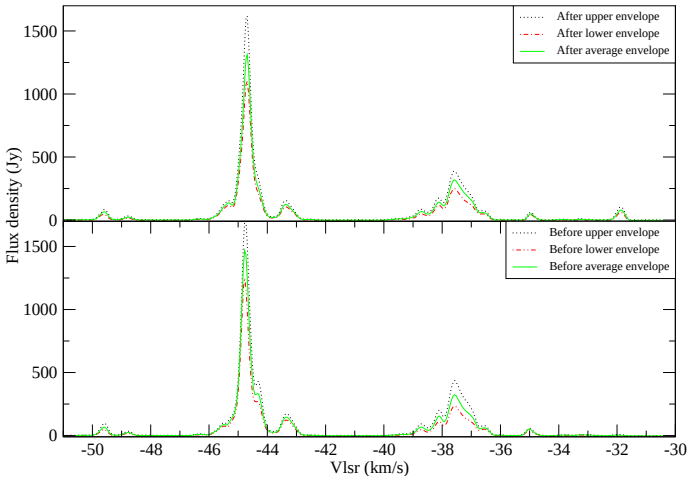

Figure 5.38: Methanol maser spectra for G328.24-0.55 at 6668-MHz.

The maser peak group with peaks at: -45.522, -44.293, -44.776 and -43.327 km.s^{-1} show regularly varying behaviour which is coupled with an increase in the intensity up to MJD 54800 (Figure 5.39). The data after MJD 55000 show that this

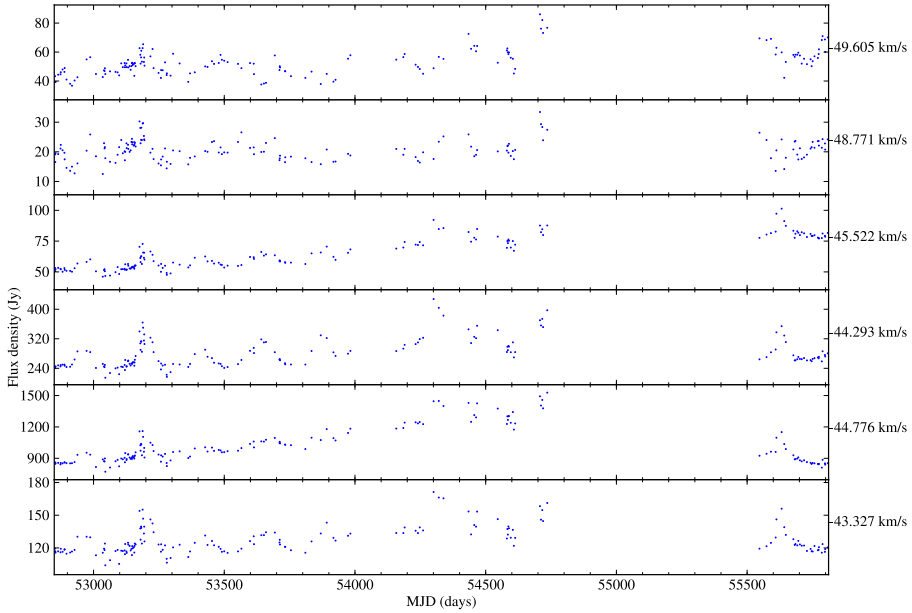

Figure 5.39: Time series for G328.24-0.55 at 6668-MHz.

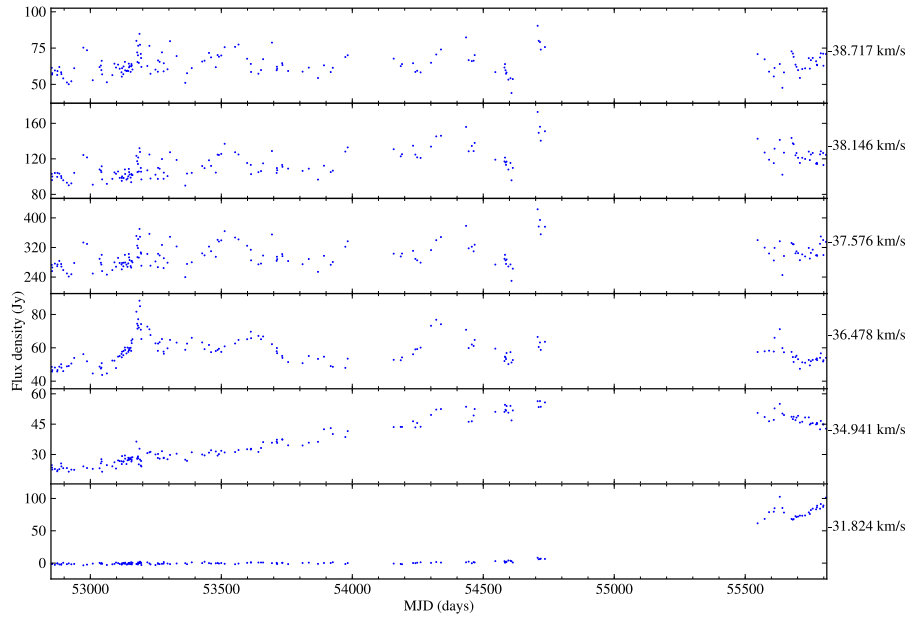

Figure 5.40: Time series for G328.24-0.55 at 6668-MHz.

increase was reversed in some maser peaks.

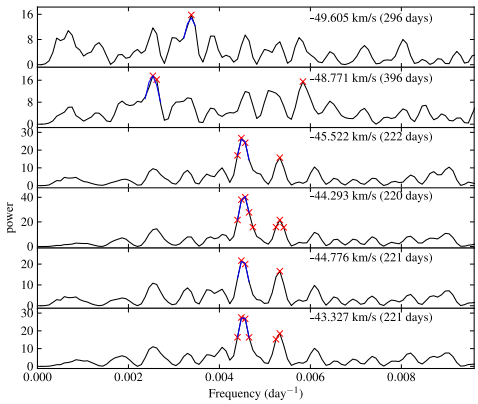

Figure 5.41: Lomb-Scargle periodograms for G328.24-0.55 at 6668-MHz.

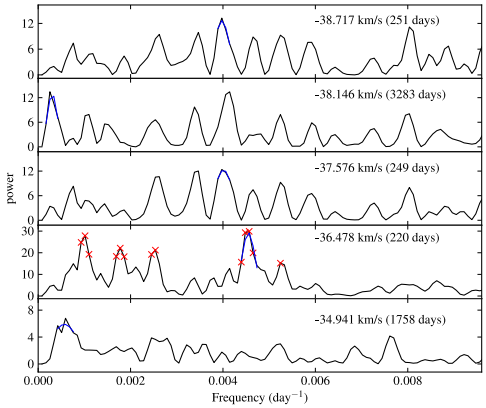

Figure 5.42: Lomb-Scargle periodograms for G328.24-0.55 at 6668-MHz.

All the time series were tested for periodicity except for that at 31.824 km.s^{-1} as it only appears in recent data. The -49.605 km.s^{-1} periodogram has multiple peaks, but the maximum peak lies below the defined significant peak limit. The Lomb-Scargle periodograms for the -48.771, -45.522, -44.293, -44.776 and -43.327 km.s^{-1} time series in Figure 5.41 show significant peaks. The epoch-folding method also shows the existence of the periods in some of the time series and the results are shown in Figure 5.43. For the -49.605 and -48.771 km.s^{-1} time series, there are several peaks which could indicate a weak detection of period. The blue-shifted maser peak time series show a consistent period (Table 5.6).

The search for periodicity using both the Lomb-Scargle (Figure 5.42) and the epoch-folding (Figure 5.44) methods was also done for the red-shifted maser peak time series. The periodograms for the -38.717, -38.146 and -37.576 km.s^{-1} time series have multiple peaks with the maximum peak below the significant limit. The summary for the periods determined is given in Table 5.6. In Table 5.6, the periods

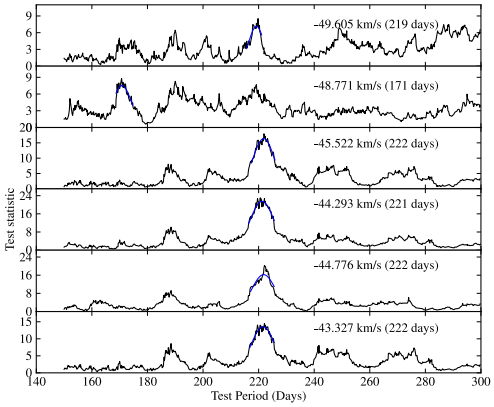

Figure 5.43: epoch-folding results for G328.24-0.55 at 6668-MHz.

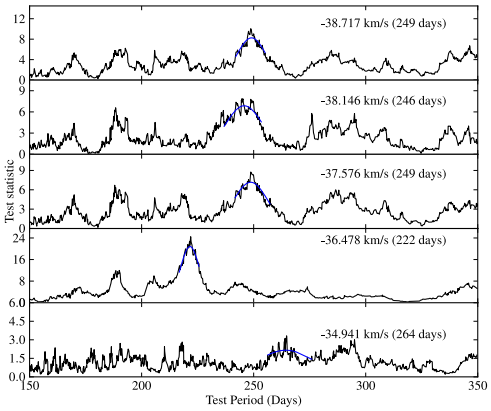

Figure 5.44: epoch-folding results for G328.24-0.55 at 6668-MHz.

determined for the -49.605 and -48.771 km.s^{-1} time series show the discrepancy between the results obtained by the Lomb-Scargle and epoch-folding methods is much greater than the formal epoch-folding errors.

Vel. (km.s^{-1})	LS (days)	EF (days)	EF error (days)
-49.605	296	219	3
-48.771	396	171	3
-45.522	222	222	4
-44.293	220	221	4
-44.776	221	222	4
-43.327	221	222	4
-38.717	251	249	7
-38.146	-	246	9
-37.576	249	249	8
-36.478	220	222	5
-34.941	-	264	13

Table 5.6: Periods determined using the Lomb-Scargle and epoch-folding methods for G328.24-0.55 at 6668-MHz.

The spectra for G328.24-0.55 at 12178-MHz are shown in Figure 5.45. The maser peak at -44.846 km.s^{-1} has become brighter.

The time series analysis was done in three maser peaks (Figure 5.46). The -

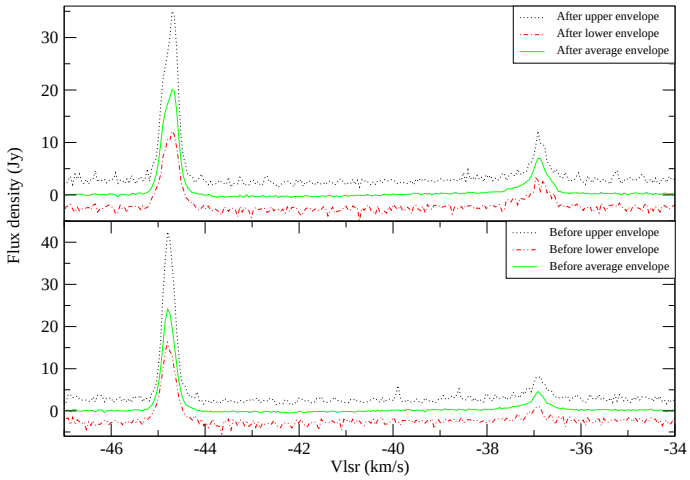

Figure 5.45: Methanol maser spectra for G328.24-0.55 at 12178-MHz before and after the bearing failure.

44.846 and -44.702 km.s^{-1} time series show strong variability. There is a flare just before 54000 MJD. The data after 55000 MJD show a better defined waveform than the data taken before the bearing failure. The -36.913 km.s^{-1} time series shows only noise variations.

After de-trending the time series, the Lomb-Scargle and epoch-folding methods were used to determine the periods. The Lomb-Scargle periodograms are shown in Figure 5.47. The periodograms for the -44.846 and -44.702 km.s^{-1} time series indicate the existence of the periods. There are other peaks in the Lomb-Scargle periodograms which are due to the fact that the peaks before 55000 MJD are random rather than regular, and their shapes are also significantly different. The epoch-folding method (Figure 5.48) confirms the results from the Lomb-Scargle method. The periods determined for these two time series have been summarised in Table 5.7. For the -36.913 km.s^{-1} time series, the Lomb-Scargle periodogram shows that the main peak is below the significant peak limit based on the false alarm probability statistics by Scargle.

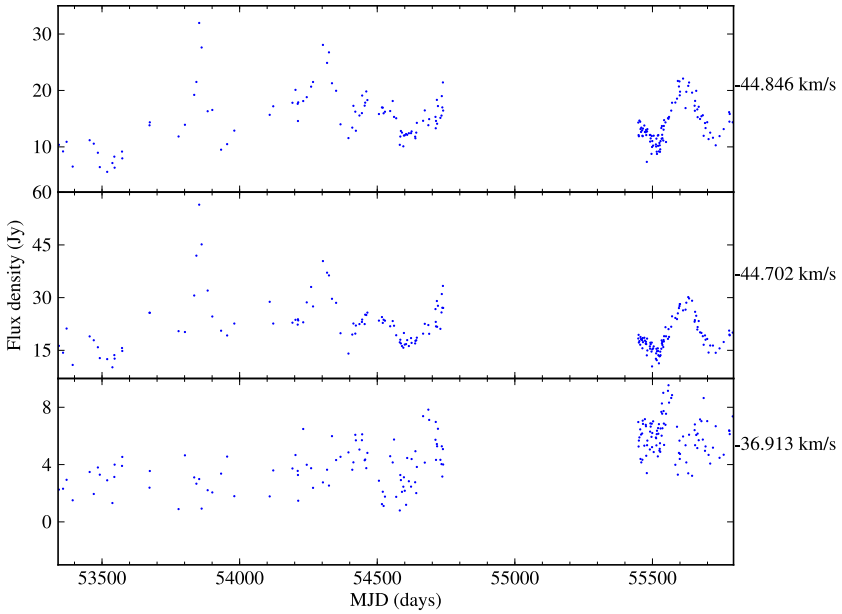

Figure 5.46: Time series for G328.24-0.55 at 12178-MHz.

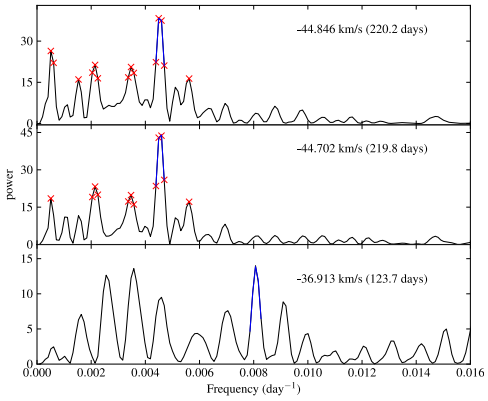

Figure 5.47: Lomb-Scargle periodograms for G328.24-0.55 at 12178-MHz.

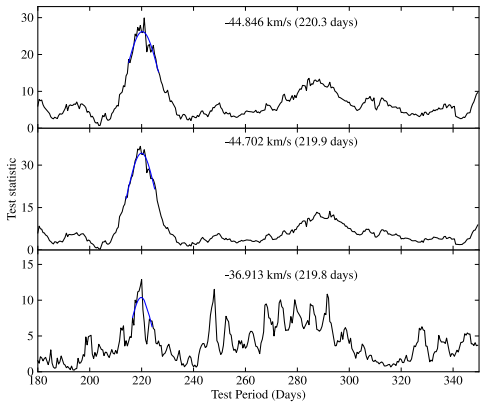

Figure 5.48: epoch-folding results for G328.24-0.55 at 12178-MHz.

Vel. (km.s^{-1})	LS (days)	EF (days)	EF error (days)
-44.846	220.2	220.3	6.0
-44.702	219.8	219.9	5.3

Table 5.7: Periods determined using the Lomb-Scargle and epoch-folding methods for G328.24-0.55 at 12178-MHz.

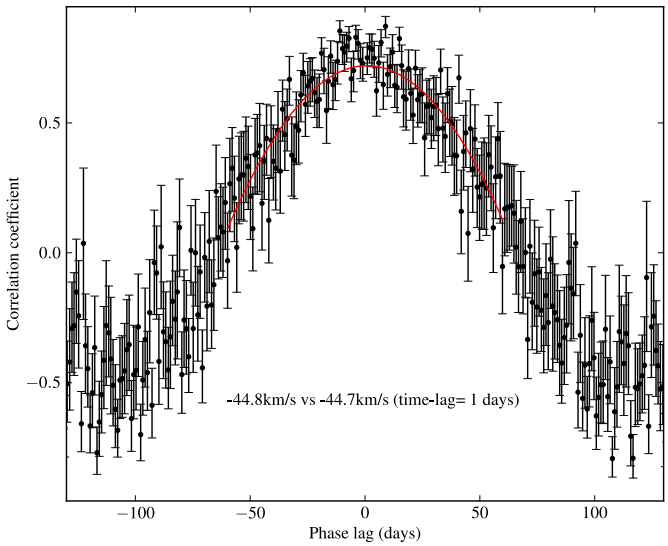

Figure 5.49: ZDCF results for G328.24-0.55 at 12178-MHz.

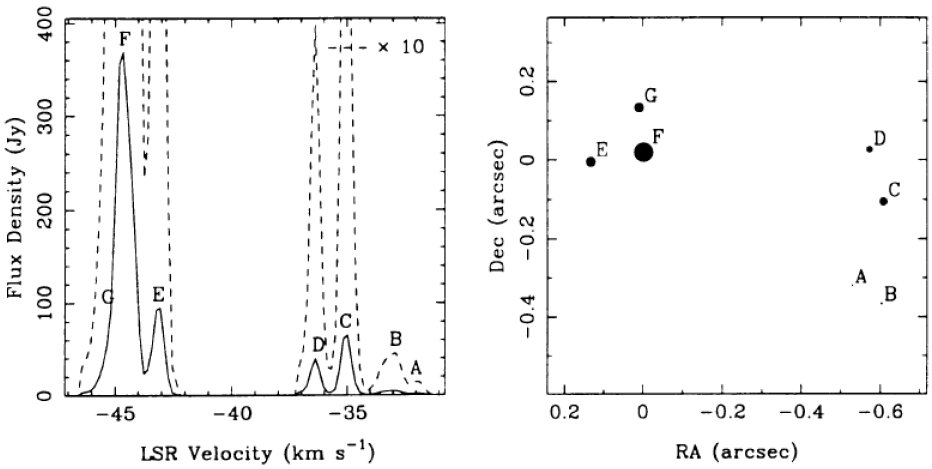

Figure 5.50: Interferometric spectra and maser spot maps for G328.24-0.55 at 6668-MHz (Phillips et al., 1998).

The ZDCF method was used on the -44.846 and -44.702 km.s^{-1} time series to check for a time delay and a correlation between them. As shown in Figure 5.49, the two time series are correlated with time delay of a day. The time delay is considered to be insignificant.

These two groups of peaks at both 6668-MHz and 12178-MHz are thought to be on the opposite edges of the UCHII region, or else each group is associated with its own protostar (see Figure 5.50). At 6668-MHz, the maser peaks' time series in these two groups have similar periods which suggests a common source of the observed regularly varying behaviour. If they have different protostars, the activities in their time series should not correlate. If this is not the case, how is it possible for two things in different locations to communicate to produce the same behaviour if their environments are different?

5.4.5 G331.13-0.24

The spectra for G331.13-0.24 at 6668-MHz are shown in Figure 5.51 and the time series of the main peaks are shown in Figure 5.52. There are two maser peak groups in the spectra - the group that lies between -92 and 90 km.s^{-1} (red-shifted group) and the group which is found between -88 and -83 km.s^{-1} (blue-shifted group). There is a weak peak around -82.5 km.s^{-1}.

The time series in Figure 5.52 show strong quasi-periodic modulation but the timing of the maxima differs. There is a flare in all time series from 53800 to 54500 MJD. The waveforms in the time series do not repeat and their time delays are small before the flare.

The Lomb-Scargle and epoch-folding methods were applied in the de-trended

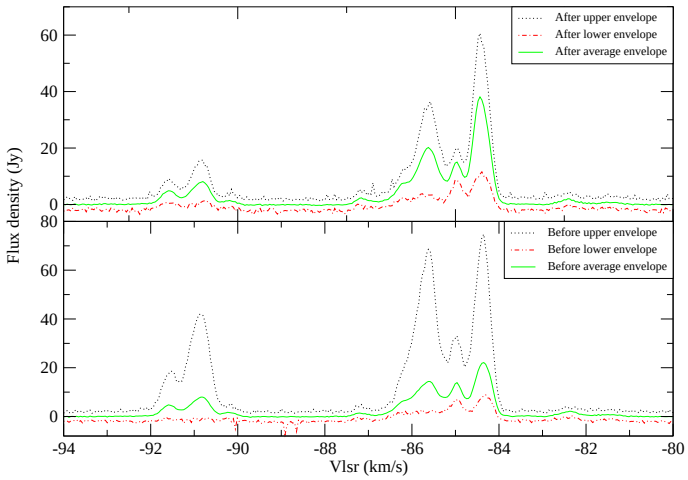

Figure 5.51: Methanol maser spectra for G331.13-0.24 at 6668-MHz before and after the bearing failure.

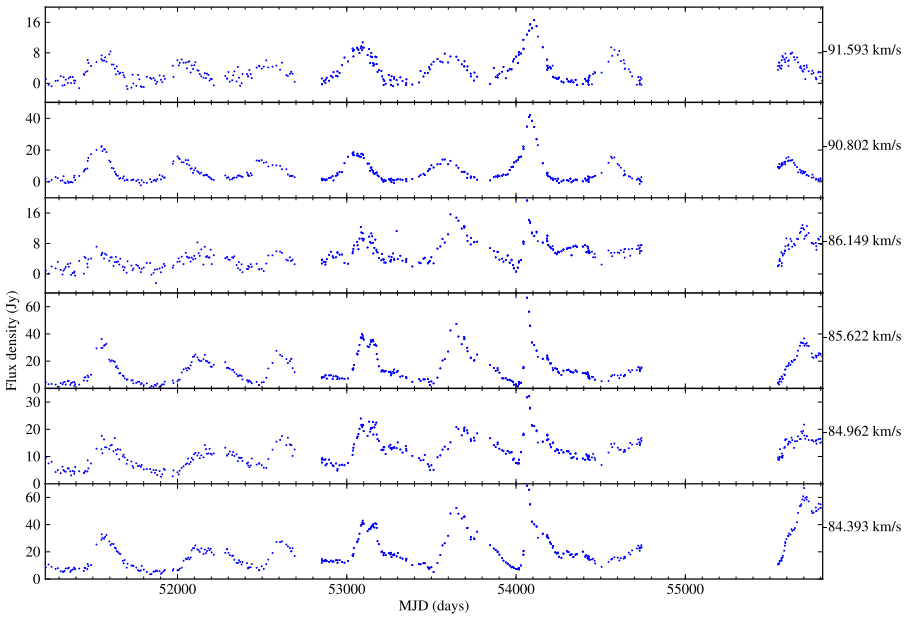

Figure 5.52: Time series for G331.13-0.24 at 6668-MHz.

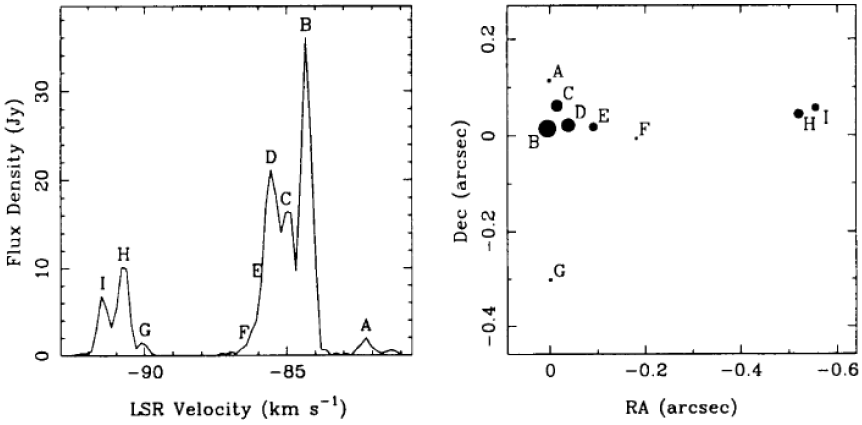

Figure 5.53: Interferometric spectra and maser spot maps for G331.13-0.24 at 6668-MHz (Phillips et al., 1998).

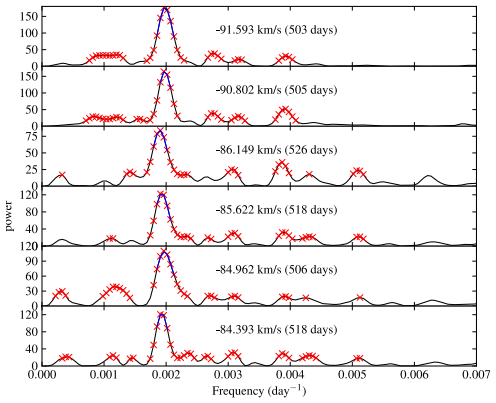

Figure 5.54: Lomb-Scargle periodograms for G331.13-0.24 at 6668-MHz.

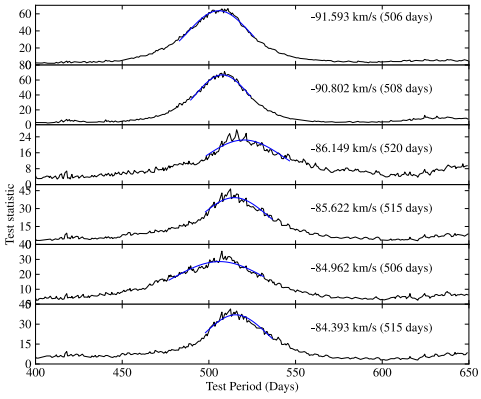

Figure 5.55: epoch-folding results for G331.13-0.24 at 6668-MHz.

time series for G331.13-0.24 at 6668-MHz (Figures 5.54 and 5.55). Both methods show the periodicity in all of the selected maser peaks (Table 5.8).

Phillips et al. (1998) produced a maser spot map for G331.13-0.24 at 6668-MHz (Figure 5.53). Apart from the maser spot at G, the morphology is linear. It was also suggested that this region could contain multiple star forming regions. The time series for spots B (84.393 km.s^{-1}), C (84.962 km.s^{-1}), D (85.622 km.s^{-1}) and E (86.149 km.s^{-1}) show flares on the decaying part of the variations that is much less evident in spots H (90.802 km.s^{-1}) and I (91.593 km.s^{-1}).

Vel.	LS (days)			EF (days)			EF error (days)		
km.s^{-1}	All	HP	NCCS	All	HP	NCCS	All	HP	NCCS
-91.593	503	489	500	506	492	501	18	39	25
-90.802	505	489	501	508	489	504	15	35	27
-86.149	518	589	533	517	551	521	20	64	34
-85.622	506	571	521	505	541	516	29	54	40
-84.962	506	551	507	516	544	504	18	55	40
-84.393	518	564	522	516	544	520	18	55	24

Table 5.8: Periods determined using the Lomb-Scargle and epoch-folding methods for G331.13-0.24 at 6668-MHz.

If we assume that all maser spots lie at the same distance from us, then the time delays in Figure 5.56 would be due to shock wave front or radiation travelling to the location of the maser spots. With this assumption, the transverse distances between the maser spots will give the minimum light travel time. Figure 5.56 shows the correlation and time delays between the -91.593 km.s^{-1} and other selected maser peaks time series. This case study should tell us whether it is a light travel or shock wave front which is responsible for the observed variations. The speed of light is 173.3 Au.day^{-1} (8.4×10^{-4} pc.day^{-1}). The adopted distance to G331.13-0.24 is 5.2 kpc (Phillips et al., 1998). The B and H have 60 days time delay which translates

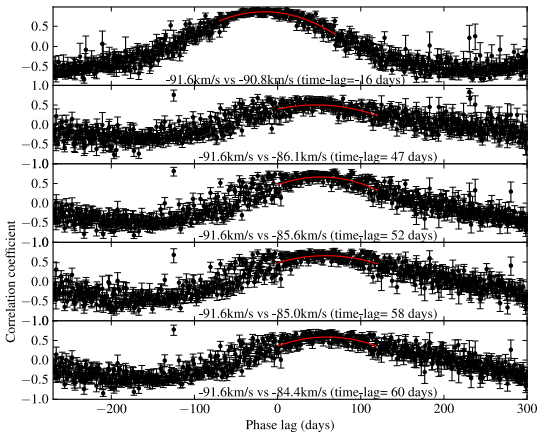

Figure 5.56: ZDCF results for G331.13-0.24 at 6668-MHz. The light curve of the peak at -91.593 km.s^{-1} is used as the reference time series.

into 0.050 pc light travel. H to B $\sim$ 0.54 arcseconds (0.014 pc) in the spot map. The high speeds of jets or outflows in young stellar objects range from 200 to 700 km.s^{-1} (Blandford, 1993) and in 60 days at 1.96×10^{-6} pc.day^{-1} (700 km.s^{-1}) they can cover about 0.00012 pc. The difference is in the order of 10^4 pc. The variations must be communicated radiatively rather than by physical propagation.

5.4.6 G338.93-0.06

The spectra for G338.93-0.06 at 6668-MHz are shown in Figure 5.57, and the time series of the main peaks in Figure 5.58.

The three brightest peaks show strong regular variations, while the peak at -41.420 km.s^{-1} shows only weak modulation. The periodic variations are coupled with some long-term variations. Around 53250.0 MJD, there is a flare, but it did not alter the regularly varying behaviour. The regular behaviour of these peaks

resembles an absolute cosine function. These time series show very quick decays and also quick rises from local minima.

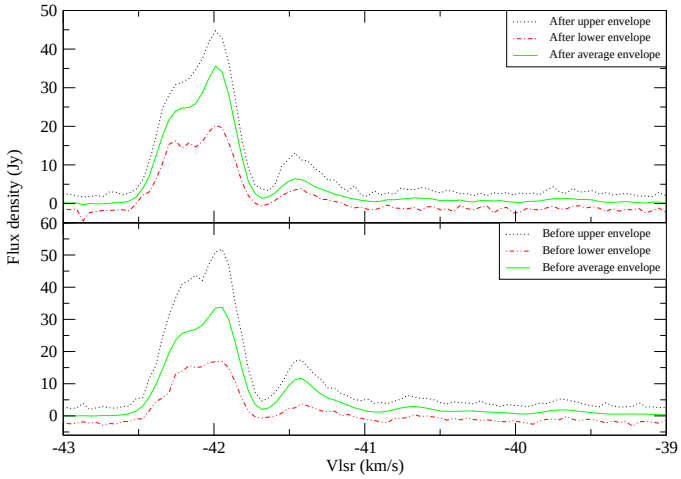

Figure 5.57: Methanol maser spectra for G338.93-0.06 at 6668-MHz before and after the bearing failure.

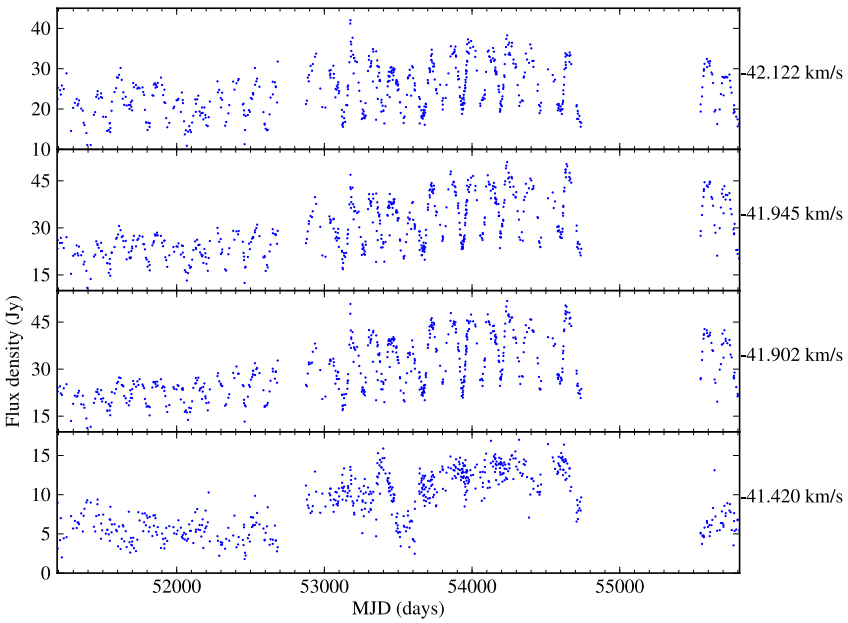

Figure 5.58: Time series for G338.93-0.06 at 6668-MHz.

After removing long-term variations in the time series in Figure 5.58 with first-

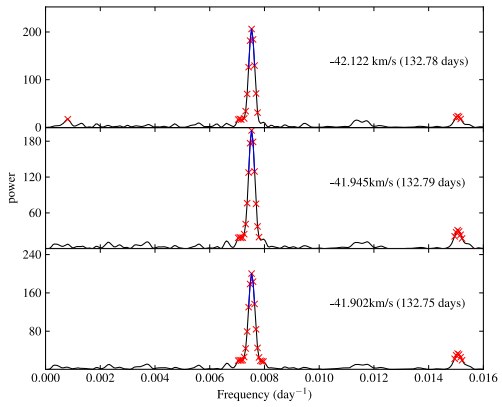

Figure 5.59: Lomb-Scargle periodograms for G338.93-0.06 at 6668-MHz.

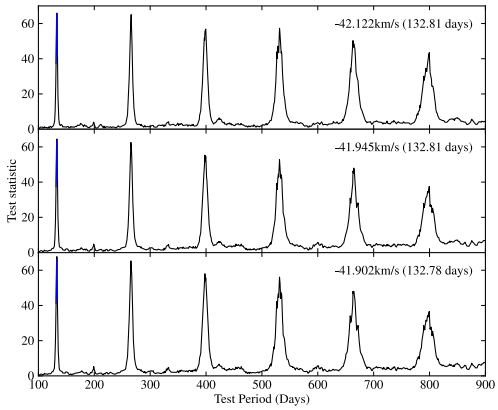

Figure 5.60: epoch-folding results for G338.93-0.06 at 6668-MHz.

Vel.	LS (days)			EF (days)			EF error (days)		
km.s^{-1}	All	HP	NCCS	All	HP	NCCS	All	HP	NCCS
-42.122	132.78	132.98	133.14	132.80	133.08	133.11	1.20	3.51	1.66
-41.945	132.79	132.38	133.00	132.79	132.59	133.00	1.25	3.19	1.66
-41.902	132.74	132.71	132.91	132.76	133.04	133.92	1.30	2.91	1.68

Table 5.9: Periods determined using the Lomb-Scargle and epoch-folding methods for G338.93-0.06 at 6668-MHz.

order polynomials, the periods were determined from Lomb-Scargle periodograms (Figure 5.59) and epoch-folding results (Figure 5.60).

Both period search methods agreed on a period of about 133 days (Table 5.9). The evolution of the period was tested by splitting the data. The periods determined for the HP and NCCS data are also shown in Table 5.9. The errors in the periods from the epoch-folding method in the complete data set (combined HP and NCCS data) is around 1 day.

The correlations and time delay results obtained by the ZDCF are shown in Figure 5.61. There are small time delays between the three main peaks which implies that they are insignificant.

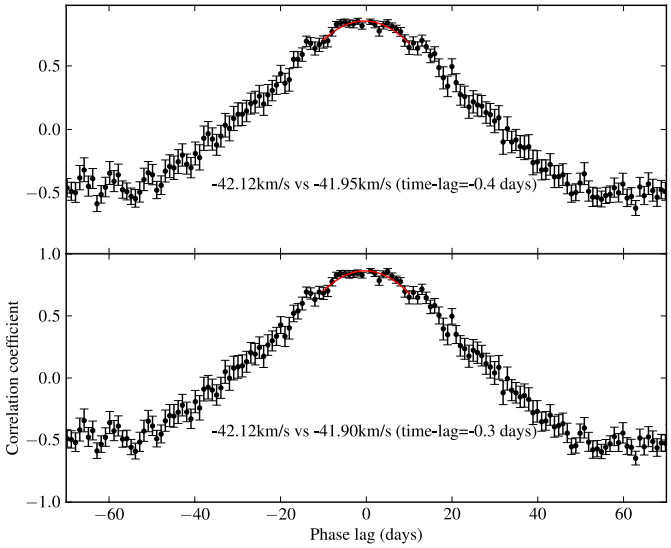

Figure 5.61: ZDCF results for G338.93-0.06 at 6668-MHz.

5.4.7 G339.62-0.12

The upper, average and lower envelopes for the spectra for G339.62-0.12 at 6668-MHz are shown in Figure 5.62 and the time series of the main peaks are shown in Figure 5.63. No new maser peaks formed over the two year gap period. The maser peaks in the spectra fall into two groups, the first between -39 and -35 km.s^{-1} (red-shifted) and the second between -34 and -29 km.s^{-1} (blue-shifted).

Nine velocity channels with maser peaks were used to create the time series (Figure 5.63). An exponential function was fitted to the time series between 52860.0-54740.0 MJD for the -33.533 km.s^{-1} (Figure 5.64). The fitted exponential function had a 1030 day e-folding time.

Periodic variations are strongest in all the red-shifted peaks. They are not seen in the blue-shifted group. Period testing was done with the Lomb-Scargle (Figure 5.65) and epoch-folding (Figure 5.66) methods for the red-shifted masers (Table 5.10).

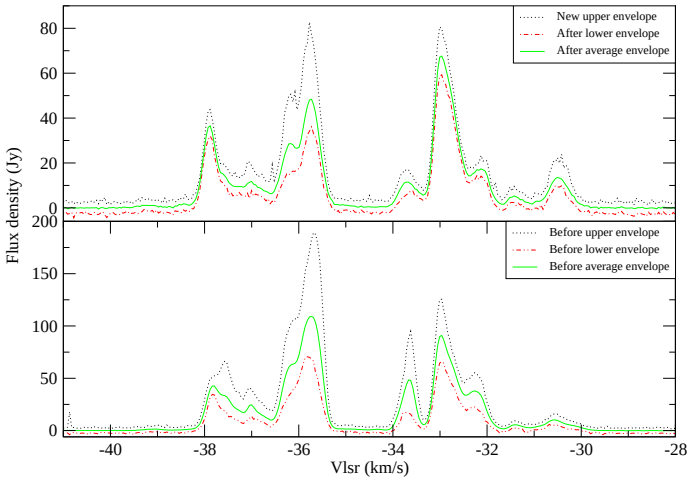

Figure 5.62: Methanol maser spectra for G339.62-0.12 at 6668-MHz before and after the bearing failure.

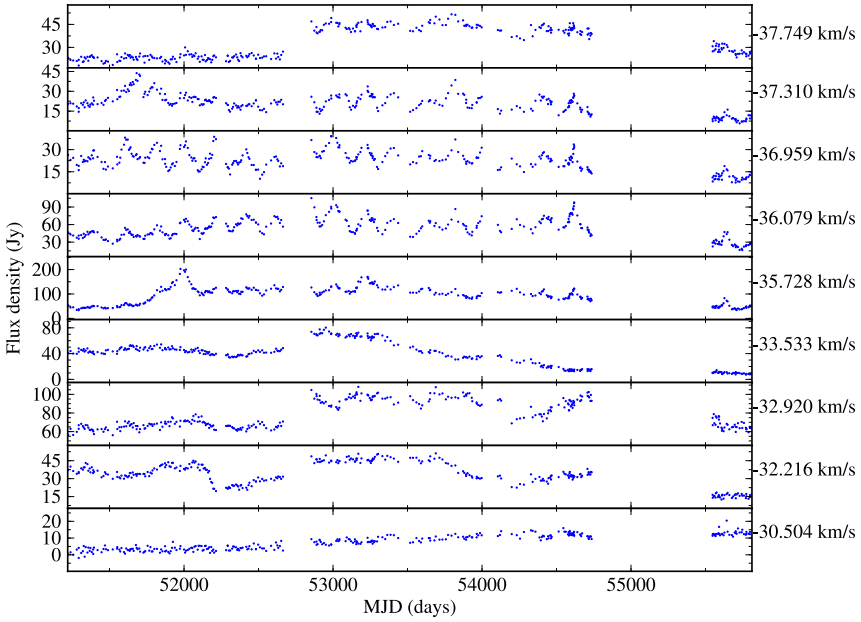

Figure 5.63: Time series for G339.62-0.12 at 6668-MHz.

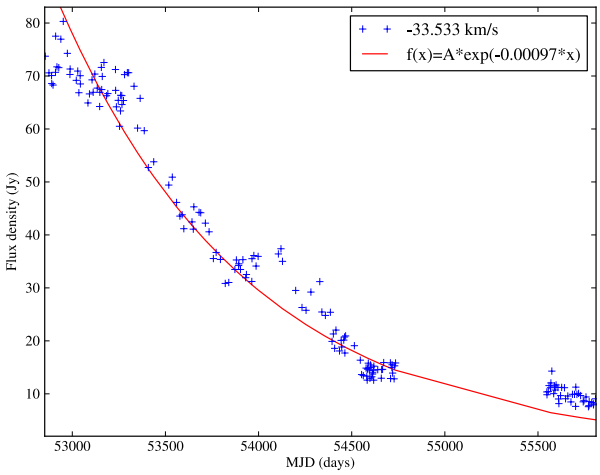

Figure 5.64: An exponential function fitted to the -33.533 km.s^{-1} (for G339.62-0.12 at 6668-MHz) time series from 52860.0 to 54740.0 MJD.

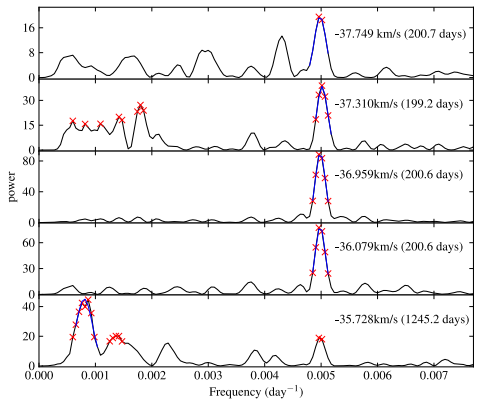

Figure 5.65: Lomb-Scargle periodograms for G339.62-0.12 at 6668-MHz.

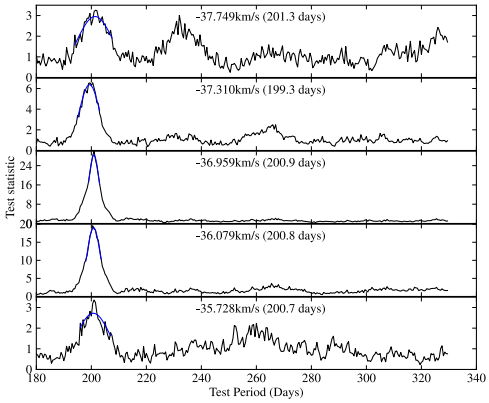

Figure 5.66: epoch-folding results for G339.62-0.12 at 6668-MHz.

Vel.	LS (days)			EF (days)			EF error (days)		
km.s^{-1}	All	HP	NCCS	All	HP	NCCS	All	HP	NCCS
-37.749	200.7	211.4	200.8	201.2	212.2	-	6.9	13.1	-
-37.310	199.2	203.3	199.9	199.5	-	201.0	3.5	-	3.5
-36.959	200.6	200.1	200.6	200.9	200.1	201.3	2.1	6.4	3.2
-36.079	200.6	203.3	198.9	200.8	202.8	199.8	2.5	9.4	3.8
-35.728	201.4	-	200.2	200.8	-	200.5	6.2	-	5.4

Table 5.10: Periods determined using the Lomb-Scargle and epoch-folding methods for G339.62-0.12 at 6668-MHz. If there was no period determined in the time series, "-" was inserted in the place of period.

The -37.749, -37.310, -36.959, -36.079 and -35.728 km.s^{-1} time series show some periodicity and the summary of the periods determined for the complete time series, HP data only and NCCS data only, are shown in Table 5.10. These maser peaks are the red-shifted group (lies between -39 and -35 km.s^{-1}). They show similar long and short-term variations.

The second group of maser peaks are the blue shifted and they lie between -34 and -29 km.s^{-1}. The -32.920 and -32.216 km.s^{-1} time series show similar behaviour which suggests a common source of the observed variability.

This region could be a multiple star forming region because some peaks are anti-correlated with one another. The blue shifted maser peaks could be associate their protostar and the red shifted maser peaks could have their own background source (protostar).

5.5 New methanol maser sources

5.5.1 G0.092+0.663

The G0.092+0.663 methanol maser source was found in the 6668-MHz methanol multi-beam maser (MMB) catalogue I, which was an unbiased search for class II methanol masers in our galactic center regions from 345° to 6° longitudes (Caswell et al., 2010). The spectra for the methanol emission at 6668-MHz are shown in Figure 5.67. It is a weak source with weak activity. Eleven maser peaks were selected to produce time series (Figures 5.68 and 5.69). All time series show weak variations which are within the range of the experimental uncertainties.

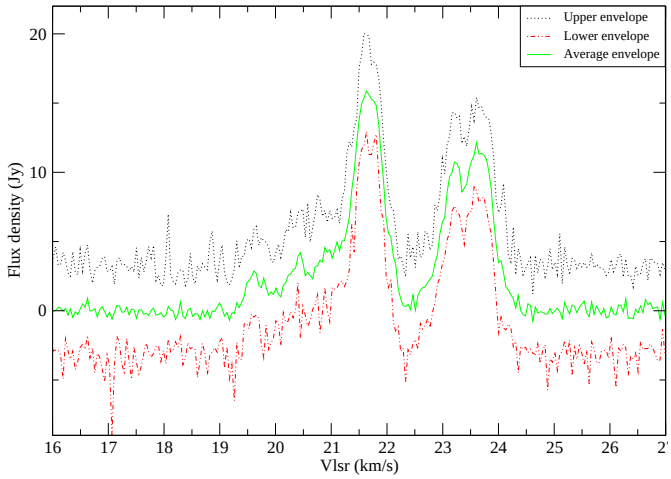

Figure 5.67: Methanol maser spectra for G0.092+0.663 at 6668-MHz.

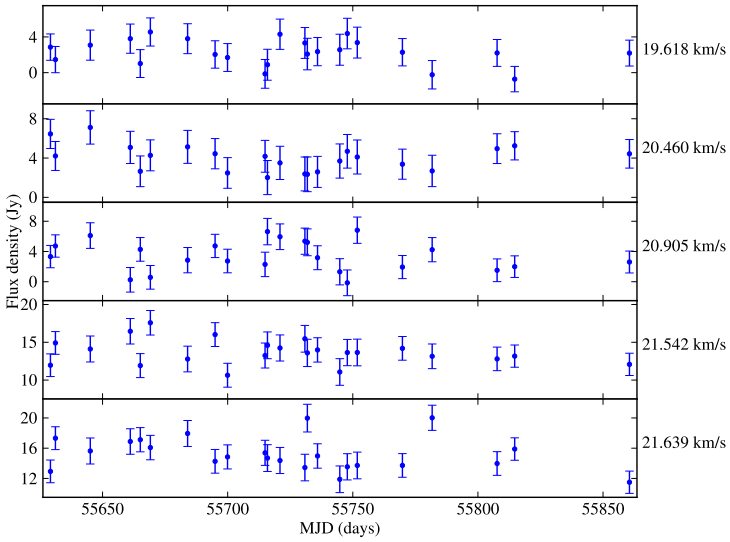

Figure 5.68: Time series for G0.092+0.663 at 6668-MHz.

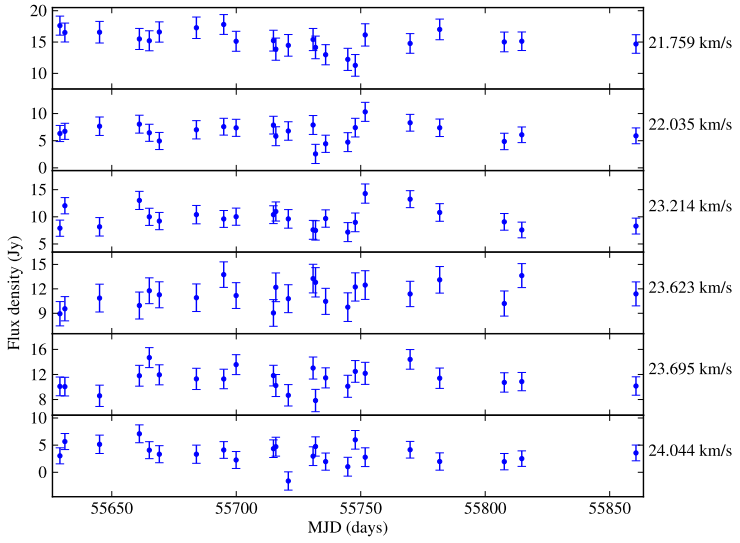

Figure 5.69: Time series for G0.092+0.663 at 6668-MHz.

5.5.2 G6.189-0.358

G6.189-0.358 was found in the 6668-MHz methanol multi-beam maser survey catalogue II, which was an unbiased search in the galactic longitudes from 6° to 20°, and it is associated with a 3 kpc arm (Green et al., 2010). It was the brightest new source in the catalogue. Its spectra are shown in Figure 5.70. The brightest maser peak in the spectra show the strongest difference between the upper and lower envelopes. The time series for eleven maser peaks are shown in Figures 5.71 and 5.72. They show weak variation during our monitoring window.

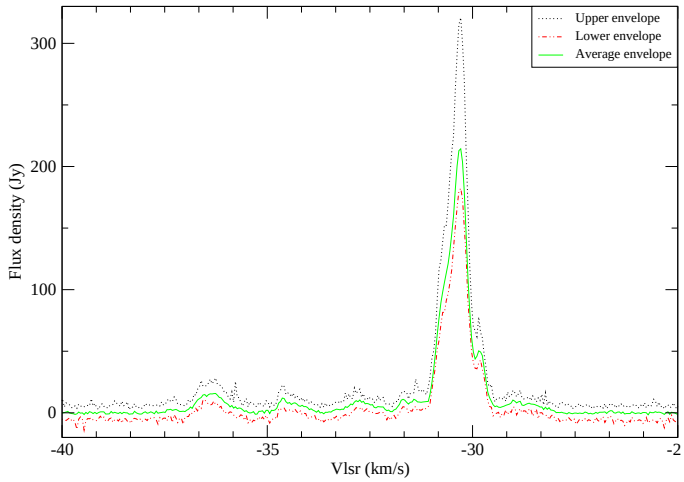

Figure 5.70: Methanol maser spectra for G6.189-0.358 at 6668-MHz.

5.5.3 G8.832-0.028

G8.832-0.028 is a bright source which was found by Xu et al. (2009) using the Australia Telescope Compact Array (ATCA) and it was confirmed in the 6668-MHz methanol multi-beam maser survey catalogue II (Green et al., 2010). Its spectra are shown in Figure 5.73. It has five main active peaks between -6 and 5 km.s^{-1}. These form three groups: (i) consists of the three brightest maser peaks at -5.314,

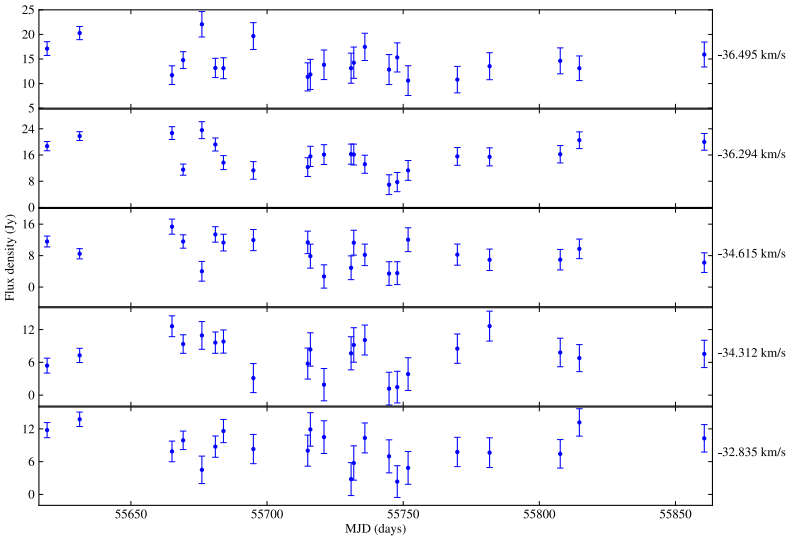

Figure 5.71: Time series for G6.189-0.358 at 6668-MHz.

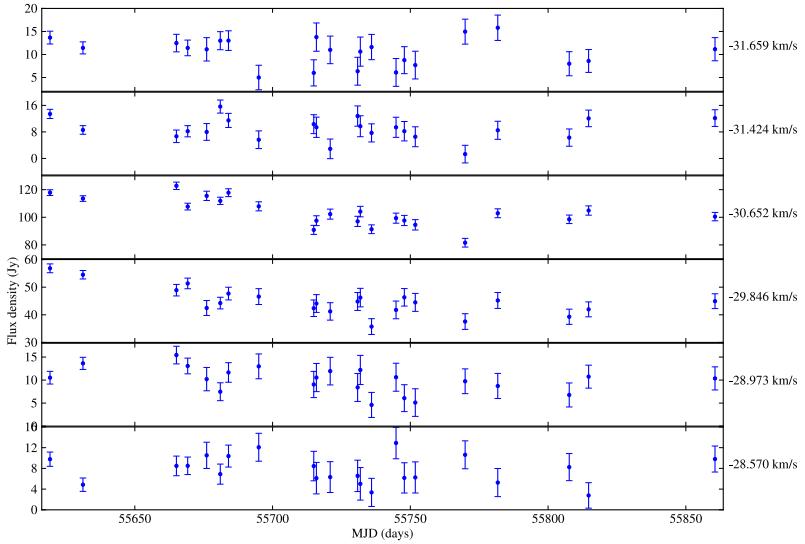

Figure 5.72: Time series for G6.189-0.358 at 6668-MHz.

-3.870 and -3.165 km.s^{-1}, (ii) has one resolved maser peak at -0.277 km.s^{-1}, (iii) occurs around 2 km.s^{-1} and it has four resolved maser peaks at 1.537, 2.040, 2.175 and 2.611 km.s^{-1}. The peak at -3.870 km.s^{-1} is the brightest in the spectrum.

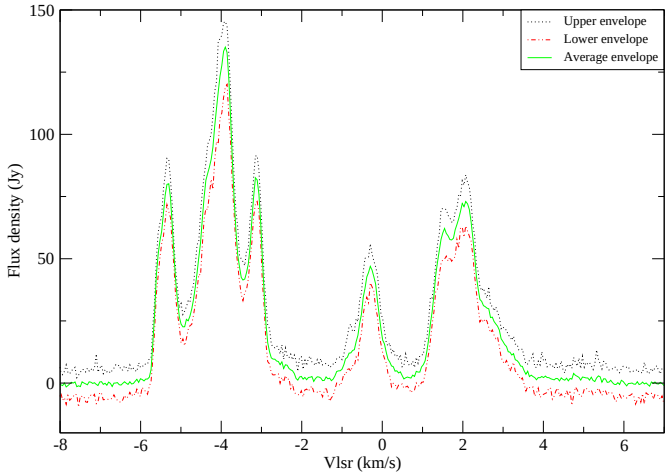

Figure 5.73: Methanol maser spectra for G8.832-0.028 at 6668-MHz.

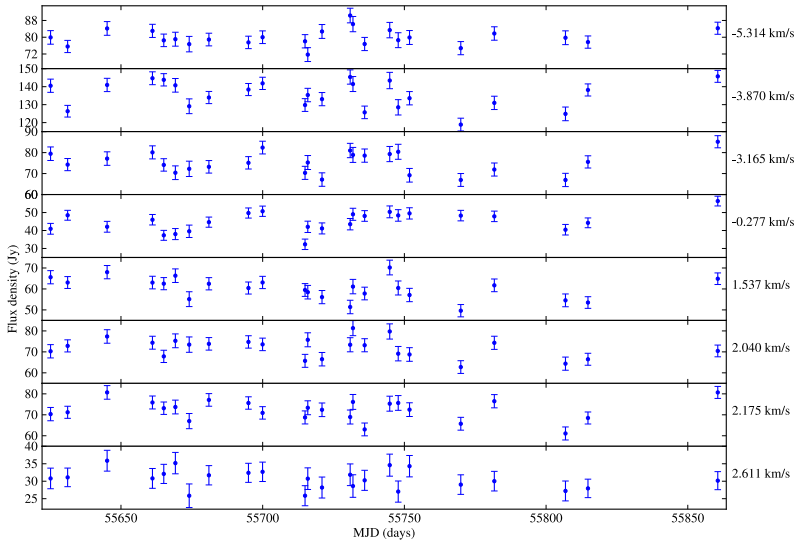

Figure 5.74: Time series for G8.832-0.028 at 6668-MHz.

G8.832-0.028 does not show significant variability over the monitoring window at 6668-MHz (Figure 5.74).

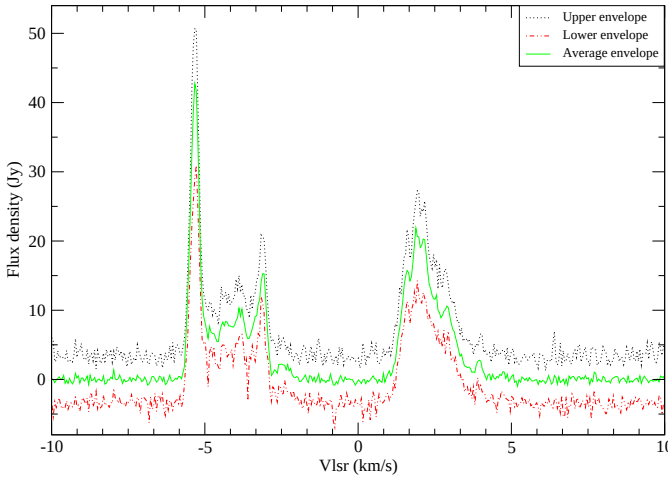

Figure 5.75: Methanol maser spectra for G8.832-0.028 at 12178-MHz.

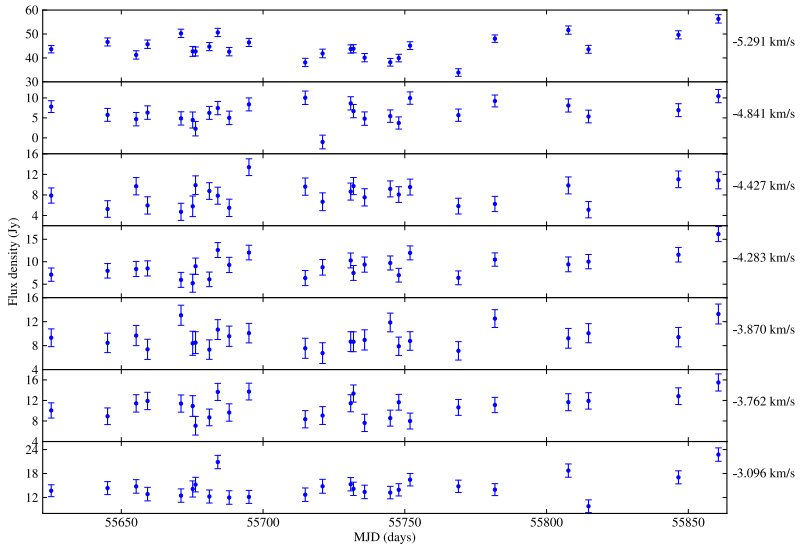

Figure 5.76: Time series for G8.832-0.028 at 12178-MHz.

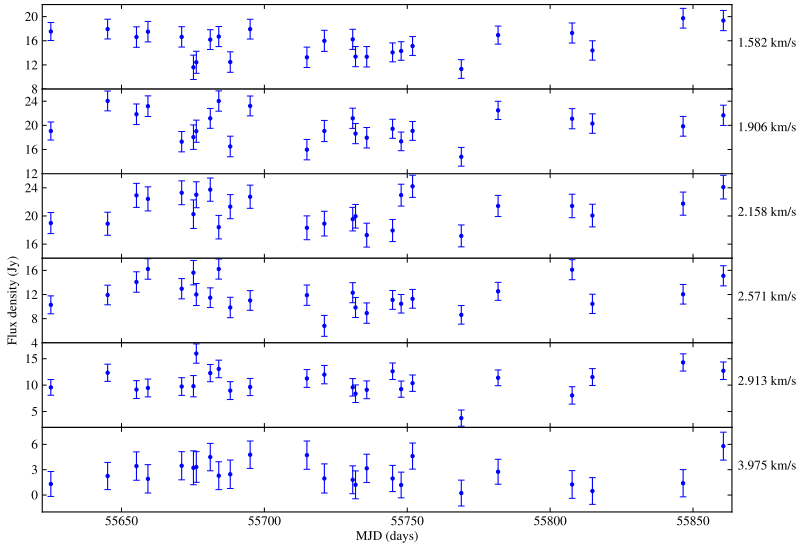

Figure 5.77: Time series for G8.832-0.028 at 12178-MHz.

The spectra of G8.832-0.028 at 12178-MHz are given in Figure 5.75 and time series of the main maser peaks in Figures 5.76 and 5.77. There are two maser peak groups, one with negative velocities and one with positive. Between -2 and 0.5 km.s^{-1}, there are emissions at the 6668-MHz spectrum (Figure 5.73) but in the 12178-MHz spectrum, there is no emission. It suggests that these two emission lines require slightly different conditions.

Time series for both groups show no significant variation, but rather random variation over the monitoring period (Figures 5.76 and 5.77).

5.5.4 G8.872-0.493

G8.872-0.493 was found in the 6668-MHz methanol multi-beam maser catalogue II (Green et al., 2010). Xu et al. (2009) determined the position of this new source using the Australia Telescope Compact Array (ATCA). The spectra for G8.872-0.493 at 6668-MHz are shown in Figure 5.78. The three brightest maser peaks at

23.256, 23.606 and 23.959 km.s^{-1} were used to produce the time series (Figure 5.79). They all show some variability but there is not enough data to confidently claim that the variability is real, also the variability occurs over a very short range.

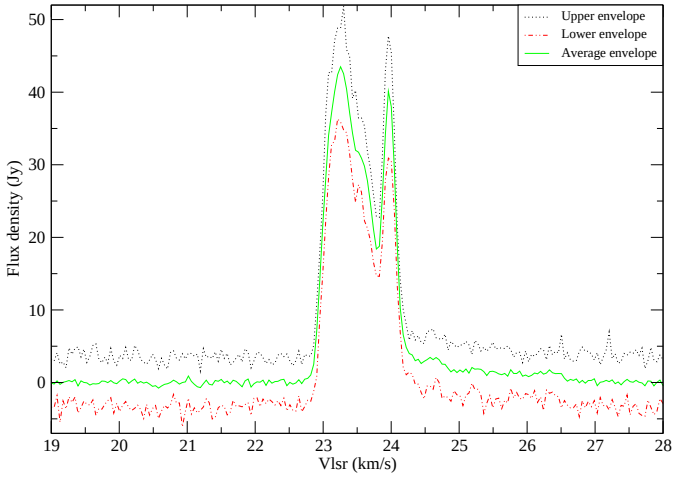

Figure 5.78: Methanol maser spectra for G8.872-0.493 at 6668-MHz.

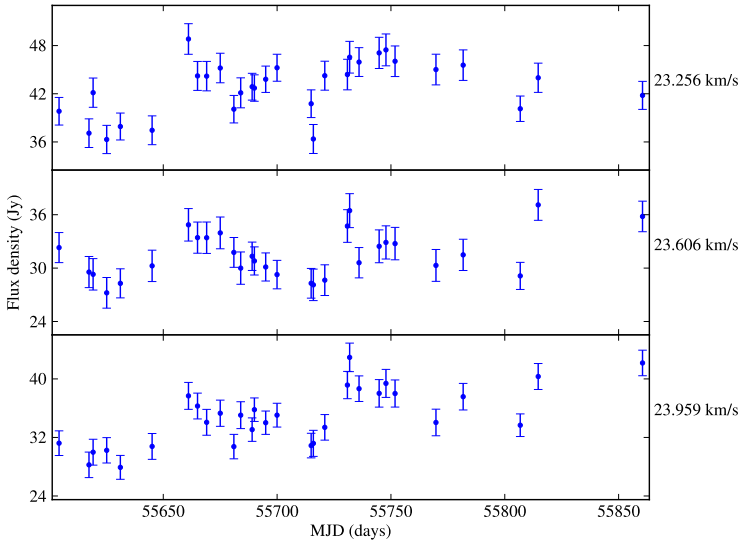

Figure 5.79: Time series for G8.872-0.493 at 6668-MHz.

Even though the data did not show several cycles in its variability, the Lomb-Scargle periodograms were produced for these time series (Figure 5.80).

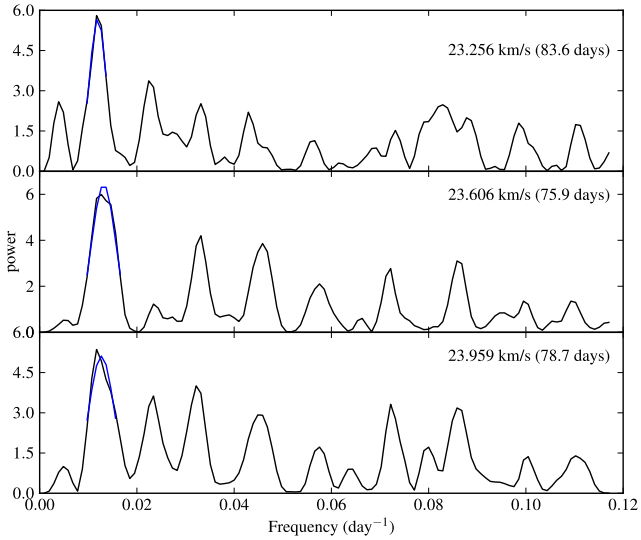

Figure 5.80: Lomb-Scargle periodograms for G8.872-0.493 at 6668-MHz.

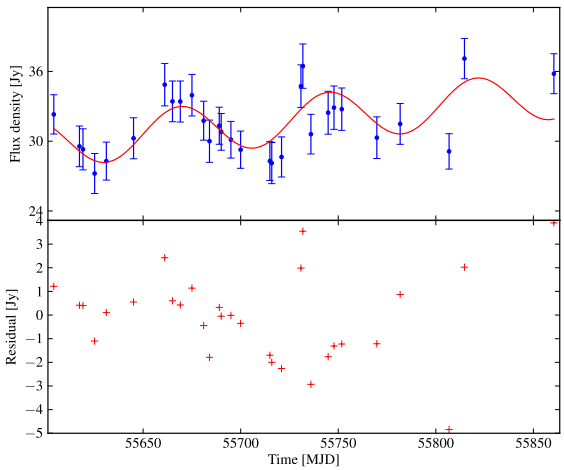

Figure 5.81: A sine function with 75.9 day period fitted to the 23.606 km.s^{-1} time series for G8.872-0.493 at 6668-MHz.

The 23.606 km.s^{-1} time series shows variations which could be periodic, with a period of 75.9 days. For the variations to be confirmed as regular or periodic, several cycles should be observed.

A sinusoidal function was fitted to the 23.606 km.s^{-1} time series to see how well this variation fits to a simple periodic function. The fitted function was defined as follows: $f(x) = A\sin(2\pi\nu x + \omega_o) + mx + c$. The parameters to be minimised are: m (gradient), c (y-intercept), A (amplitude) and ω_o (phase). The mx and c terms are for long-term variation. In Python, the script was written to use the module called optimize.leastsq() to determine the best curve fit to the 23.606 km.s^{-1} time series (Figure 5.81). Even though it appears to be periodic, there is not enough data to confirm whether G8.872-0.493 at 6668-MHz is periodic or quasi-periodic, even random variations can mimic periodically for a short time period. The monitoring on this source will need to be continued in order to confirm if this source is periodic or not.

5.5.5 G348.617-1.162

G348.617-1.162 was found in the 6668-MHz methanol multi-beam maser catalogue I and it was the brightest new maser source in the catalogue (Caswell et al., 2010). The spectra of this source are shown in Figure 5.82. The difference between the upper and lower envelopes suggests that the range of variation is small. Twelve maser peaks were used to produce the time series over the monitoring period (Figures 5.83 and 5.84). The small variations observed are within the range of experimental uncertainties.

G348.617-1.162 was also observed and monitored at 12178-MHz, the spectra

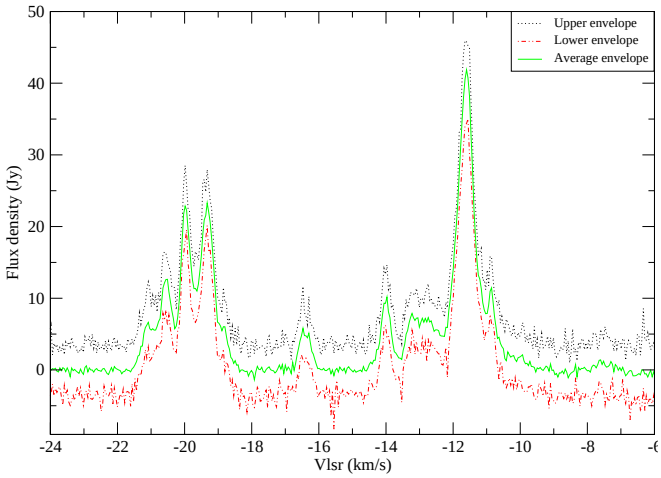

Figure 5.82: Methanol maser spectra for G348.617-1.162 at 6668-MHz.

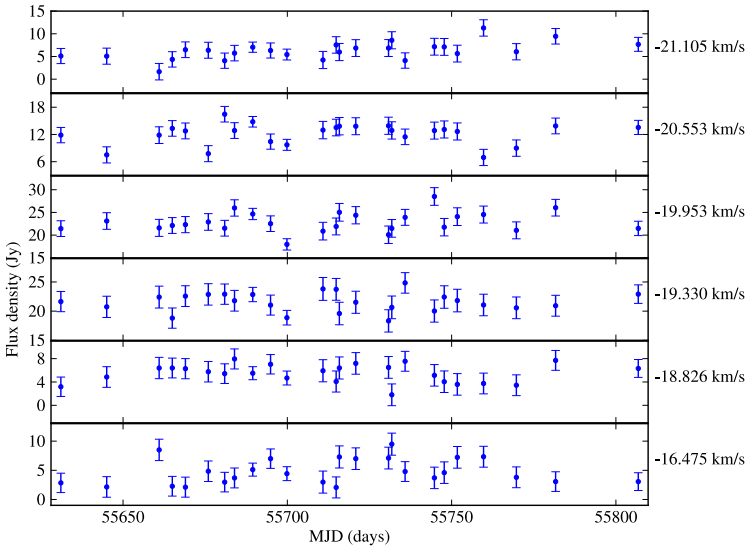

Figure 5.83: Time series for G348.617-1.162 at 6668-MHz.

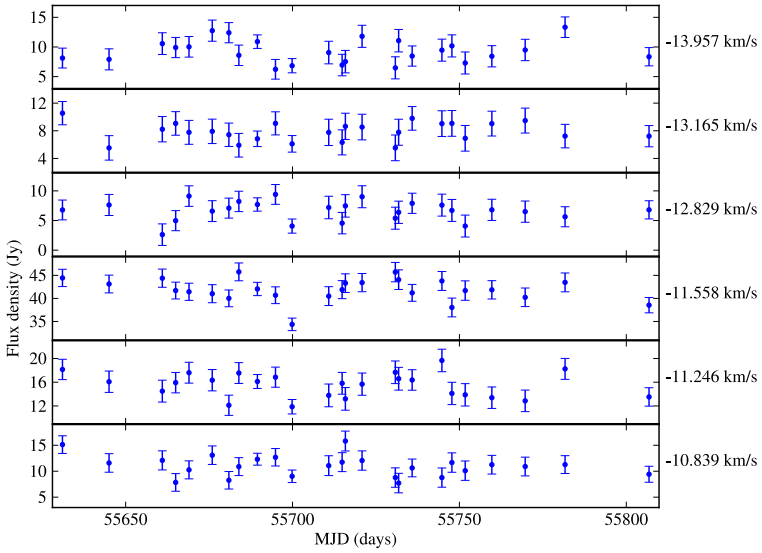

Figure 5.84: Time series for G348.617-1.162 at 6668-MHz.

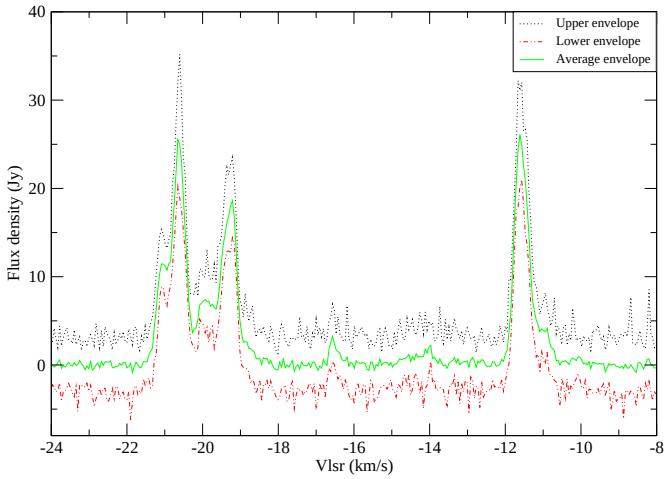

Figure 5.85: Methanol maser spectra for G348.617-1.162 at 12178-MHz.

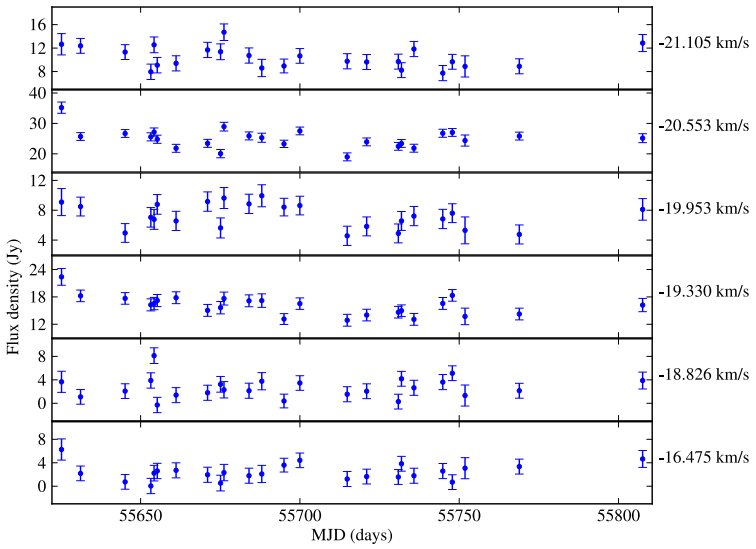

Figure 5.86: Time series for G348.617-1.162 at 12178-MHz.

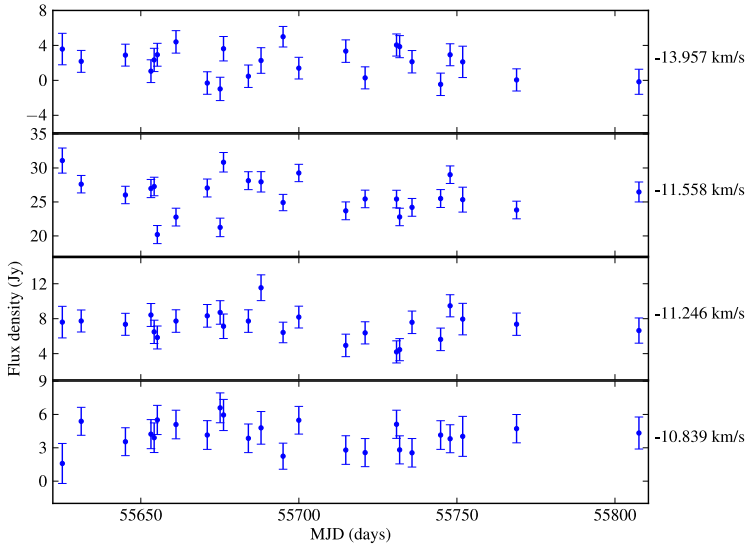

Figure 5.87: Time series for G348.617-1.162 at 12178-MHz.

obtained at 12178-MHz are shown in Figure 5.85. The emissions occur at a similar velocity range to that at 6668-MHz. The maser peaks were selected to produce the time series (Figures 5.86 and 5.87). They show no significant variations.

5.5.6 G351.688+0.171

G351.688+0.171 was found in the 6668-MHz methanol multi-beam maser catalogue I (Caswell et al., 2010) and its spectra are shown in Figure 5.88. There are two main maser peak groups: (i) the red-shifted group (from -22.5 to -17.5 km.s^{-1}), and (ii) the blue-shifted (from -12.5 to -10 km.s^{-1}). Their time series (Figures 5.89 and 5.90) show no significant variations.

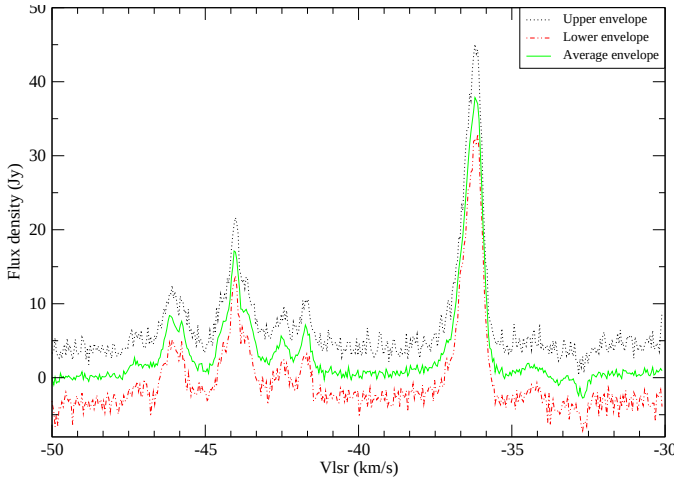

Figure 5.88: Methanol maser spectra for G351.688+0.171 at 6668-MHz.

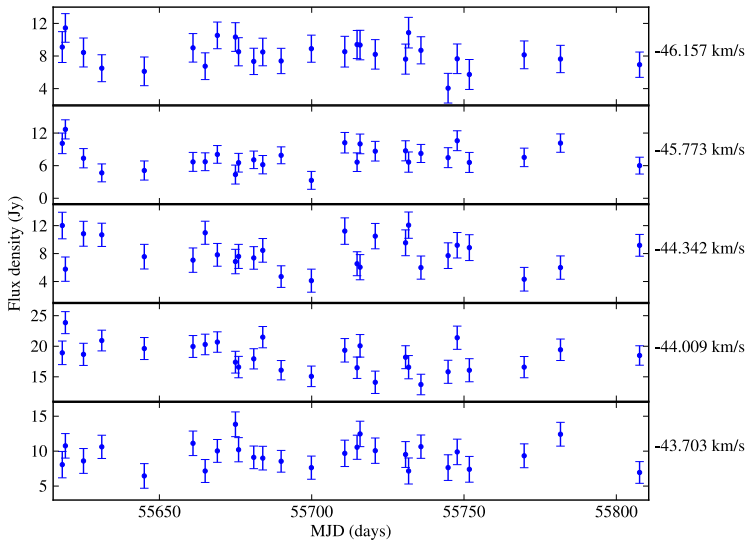

Figure 5.89: Time series for G348.617-1.162 at 6668-MHz.

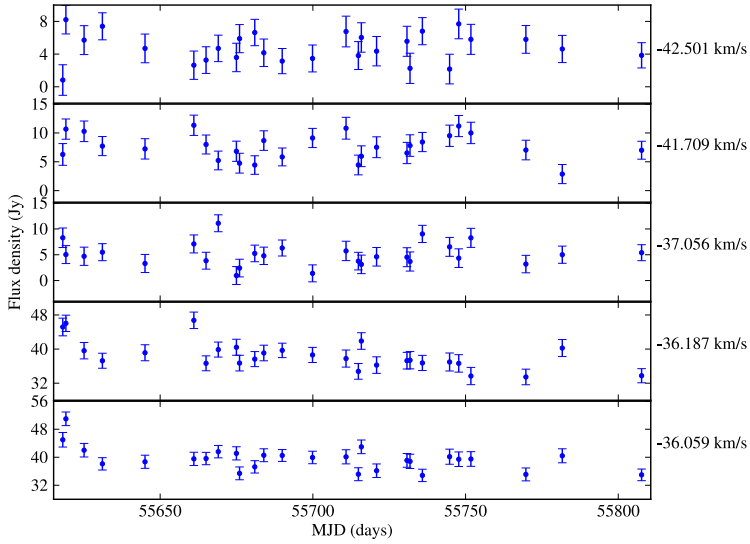

Figure 5.90: Time series for G351.688+0.171 at 6668-MHz.

5.5.7 G358.460-0.391

The G358.460-0.391 was obtained from the Australian 6668-MHz methanol multi-beam maser (MMB) catalogue I (Caswell et al., 2010) and Figure 5.91 shows its spectra at 6668-MHz. In these spectra, there are two maser peak groups which are: three maser peaks at -7.584, -7.382 and -6.476 km.s^{-1}, two maser peaks at 1.147 and 1.685 km.s^{-1}. The time series are shown in Figure 5.92.

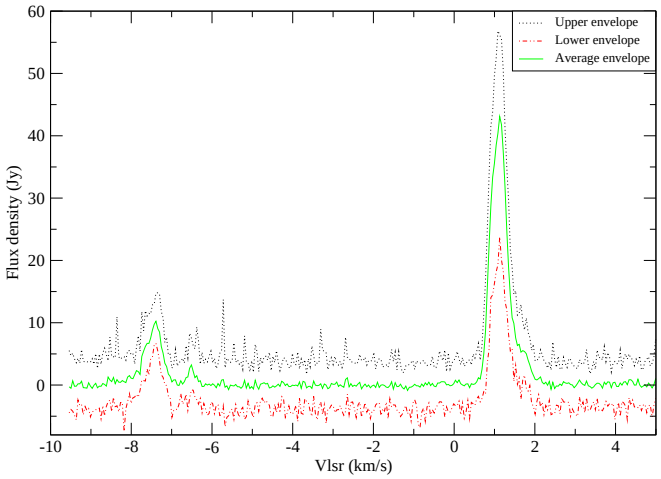

Figure 5.91: Methanol maser spectra for G358.460-0.391 at 6668-MHz.

The time series at 1.147 km.s^{-1} shows strong variability (see Figure 5.92). Its variability could be periodic, but several cycles are required to conclude that it is a new periodic source. The monitoring needs to continue for this source to see if it is periodic.

The Lomb-Scargle method was used to produce periodograms for the G358.460-0.391 time series at 6668-MHz (see Figure 5.93). All show negative results except for the time series at 1.147 km.s^{-1}, which shows a period of 186.9 days. The least-squares fit for a 186.9 day period sine function and a first-order polynomial to the 1.147 km.s^{-1} time series is shown in Figure 5.94. long-term monitoring is required

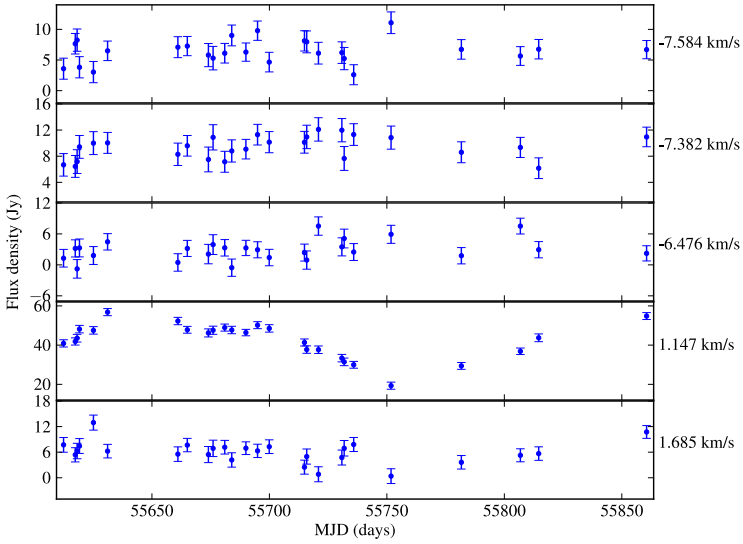

Figure 5.92: Time series for G358.460-0.391 at 6668-MHz.

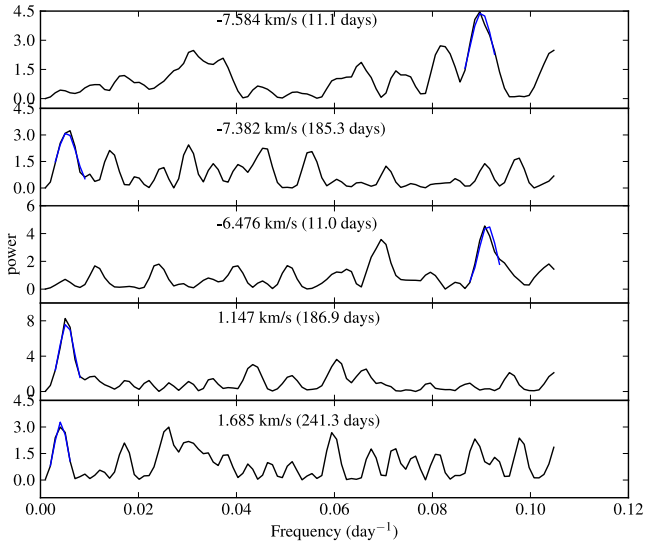

Figure 5.93: Lomb-Scargle periodograms for G358.460-0.391 at 6668-MHz.

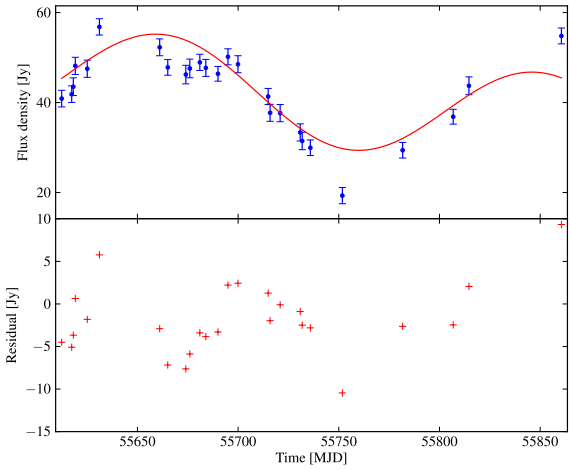

Figure 5.94: A sine function with a 186.9 day period fitted to the 1.147 km.s^{-1} time series for G358.460-0.391 at 6668-MHz. The residuals for the fit are shown in the bottom diagram.

to confirm the nature of the variability of G358.460-0.391 at 6668-MHz.

Chapter 6

Discussion

6.1 Introduction

The time series for the class II methanol masers in Chapter 5 show regularly and irregularly varying behaviour which are sometimes embedded in long-term variations. In this chapter, the common behaviour observed in methanol sources and the search results for the new periodic or quasi-periodic methanol maser sources are discussed.

The periods for the periodic and quasi-periodic sources are presented and the assumptions used to get to the final periods and period uncertainties are discussed. The extreme (minimum and maximum) periods were used to determine the properties of a binary star system. In the quest for understanding more about class II methanol masers, the common features in the sources have been singled out and discussed in detail; these are flares, long-term variations and waveforms.

In our new methanol maser sample, two sources could be periodic or quasi-periodic.

6.2 Periodic and quasi-periodic methanol maser sources

The spectra, time series, Lomb-Scargle periodograms, epoch-folding results, and time series correlations and delays for seven periodic and quasi-periodic methanol maser sources were shown in Section 5.4.

6.2.1 Periods for the periodic or quasi-periodic sources

In order to determine the period of a source in either the 6668-MHz or 12178-MHz emission line, it was assumed that the observed periodicities in the time series are due to a common mechanism. Using this assumption, the period determined by the Lomb-Scargle method for a methanol maser at each frequency can be approximated by the average period for all time series in the source (see Table 6.1). For the periods determined by the epoch-folding method, a weighted average was determined rather than the standard average value. The weighted average μ can be determined by minimising χ^2 given by

$$\chi^2 = \sum_i^N \left(\frac{x_i - \mu}{\sigma_i} \right)^2, \tag{6.1}$$

where σ_i is the error of x_i and it is not a constant. By setting $\frac{\partial \chi^2}{\partial \mu} = 0$, the weighted average μ is given by

$$\mu = \frac{\sum_i \left(\frac{x_i}{{\sigma_i}^2} \right)}{\sum_i \left(\frac{1}{{\sigma^2}_i} \right)}. \tag{6.2}$$

The error in the weighted average can be derived using error propagation (Taylor, 1997), which will be:

$$\begin{aligned} {\sigma^2}_\mu &= \textstyle\sum_i {\sigma^2}_i \left(\frac{\partial \mu}{\partial x_i}\right)^2, \\ {\sigma^2}_\mu &= \frac{1}{\sum_i \left(\frac{1}{{\sigma^2}_i}\right)}. \end{aligned} \tag{6.3}$$

The weighted averages and their errors for the epoch-folding method are given in Table 6.1. Equation 6.3 is true if the data are independent. In our time series, there are variables which produce dependencies in different velocity channels. All the time series from different velocity channels in the spectrum are scaled by the same Point Source Sensitivity (PSS), the same atmospheric correction, etc. These activities will produce correlations between the time series from different velocity channels. However, in our case we assumed that the time series are independent, although this condition is not strictly met in this dataset. This simplification assumption will result in underestimating the error in the averaged period for each source.

Source	Freq. (MHz)	LS (days)	EF (days)	$\Delta(EF)$ (days)
G12.89+0.49	12178	29.38	29.40	0.11
G338.93-0.06	6668	132.8	132.8	0.7
G339.62-0.12	6668	200.5	200.6	1.4
G328.24-0.55	6668	220.8	221.7	2.1
	12178	220.0	220.1	4.0
G9.62+0.20E	6668	242.8	243.3	1.6
	12178	243.4	243.7	1.8
G188.95+0.89	6668	393.3	394.1	5.6
	12178	383.6	383.8	6.2
G331.13-0.24	6668	509.3	511.0	7.6

Table 6.1: Comparison of the periods for the periodic and quasi-periodic methanol maser source sample.

If the source of the periodicities is the same for both the 6668-MHz and the

12178-MHz emission line, then the weighted average period of the 6668-MHz and 12178-MHz emission lines will be a better approximation of the epoch-folding periods. Using the above arguments, weighted mean periods and uncertainties were determined using the epoch-folding results (Table 6.2).

Source	Period (days)	Period Error (days)	Percentage Error
G12.89+0.49	29.40	0.11	0.37
G9.62+0.20E	243.5	1.2	0.49
G338.93-0.06	132.8	0.7	0.54
G339.62-0.12	200.6	1.4	0.69
G328.24-0.55	221.4	1.9	0.84
G188.95+0.89	389.4	4.2	1.06
G331.13-0.24	511.0	7.6	1.48

Table 6.2: The weighted mean periods, period errors and percentage errors for the periodic and quasi-periodic methanol maser source sample.

In Table 6.2, the uncertainties in the periods of the sources were determined using Equation 6.3. G188.95+0.89 and G331.13-0.24 have large percentage errors (> 1) and large period errors. These are the sources with longer periods and they were sampled like the others. Only G12.89+0.49 required two to four days sampling because of a 29.40 *pm* 0.11 day period. The periods in some of the selected time series in G188.95+0.89 and G331.13-0.24 were not significantly different but their uncertainties were large. These arguments suggest that they are probably quasi-periodic sources, but there is no easy distinction between periodic and quasi-periodic.

Throughout the monitoring period, some sources show a high degree of regularity (Table 6.1). These environments are evolving and energetic, yet these sources show strong periodicities. It means that precise conditions are required to produce the observed periodicities.

6.2.2 Origin of the regular variations

It was shown that some of the class II methanol masers are either periodic or quasi-periodic, and they (6668-MHz and 12178-MHz methanol maser lines) are thought to be radiatively pumped (see Section 2.4). A very important question is, the origin of these observed periodicities.

It is known that there are stars which are variable. The pulsating variable stars could be the source of the observed periodicities. Stellar pulsation is due to a pressure fluctuation inside the star (Stahler & Palla, 2004). Eyer & Mowlavi (2008) summarise the variable stars in the Hertzsprung-Russell (HR) diagram and they are found almost everywhere in the diagram. Figure 6.1 shows some of the known pulsating stars (e.g. Mira, RR Lyrae, Cepheid, etc. (Stahler & Palla, 2004)) in the HR diagram. Ramsay et al. (2011) reported new short periods for pulsating stars (SX Phe or δ Scuti stars) ranging between 51-83 minutes, and Hart et al. (2007) found typical long periods in 54 of 378 pulsating stars (Long Period Variable) being between 100-300 days. Eyer & Mowlavi (2008) give periods of 80 seconds to 8 minutes for the EC 14026 stars, and high periods ranging between 50-1000 days for Semi-regular (SR) and Mira stars. Table 6.3 gives the periods for some of the known periodic pulsating stars. The periods for our periodic and quasi-periodic methanol maser source sample ranges from 29.4 to 511.0 days. In our case, the stars are still being formed and the period range suggests that they should be evolved stars which they are clearly not. So pulsating stars are unlikely to be the source of the observed periodic or quasi-periodic behaviour in class II methanol maser time series.

Another possibility of explaining the periodicity was proposed by Sobolev et al. (2007) (see section 2.6). It was proposed that the variability of masers could be

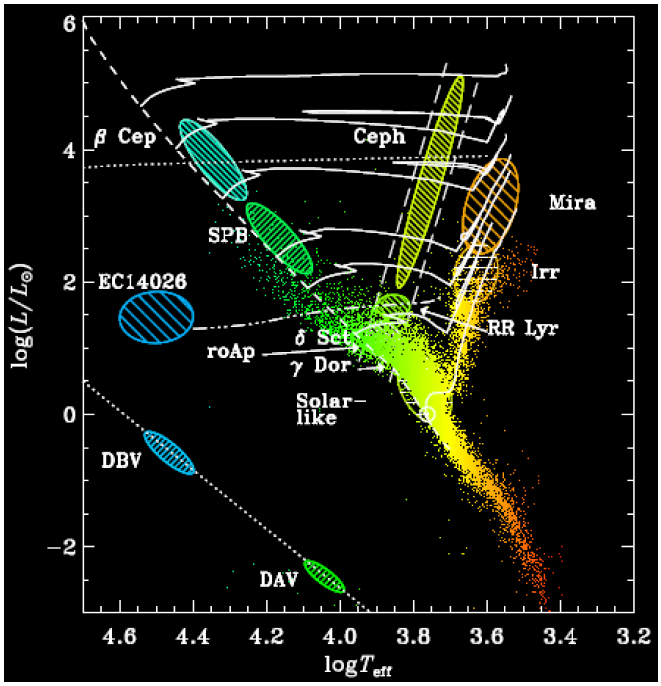

Figure 6.1: Hertzsprung-Russell (HR) diagram taken from De Cat (2001) with some of the variable stars. The instability strip is shown by two parallel diagonal dash lines. The solid lines represent different stellar evolution paths - with more horizontally flat lines representing massive star evolution paths.

due to the variation in the surrounding environment (dust temperature) in which they are found. In contrast, van der Walt (2011) proposed the Colliding Wind Binary (CWB) model as the source of the periodic variability for G9.62+0.20E (see section 2.6). The model does not include the variations in the disk and the accretion processes of the binary system which can affect the evolution of the period. Perhaps, if these two models can be coupled one can produce a model that better explains the observed behaviour.

Star	Period	Amplitude (mag)
EC 14026	80 s-8 m	up to 0.03
ZZ Ceti	0.5 - 25 m	up to 0.2
V777 Her	2 - 16 m	up to 0.2
roAp	5-20 m	up to 0.01
GW Vir	5 -80 m	up to 0.2
PG1716 "Betsy"	30-150 m	up to $\sim$ 0.01
δ Scuti	30 m - 6 h	up to few 0.1
β Cephei	2-12 h	up to 0.05
RR Lyrae	5 h - 1.1 d	0.2-2
γ Dor	8 h -3 d	up to few 0.01
Slowly Pulsating B (SPB)	0.5 - 5 d	up to 0.03
W Vir	1-20 d	0.3-1.2
α Cyg	1-50 d	few 0.1
Cepheids	2-70 d	0.1-1.5
RV Tau	30 - 150 d	1-3
Semi-regular (SR), Mira	50 - 1000 d	up to 8

Table 6.3: Some of the known variable stars listed by Eyer & Mowlavi (2008). The periods are given in seconds (s), minutes (m) and days (d). For each type of star, the magnitude (mag) ranges are given as amplitude of the variations.

Assuming that the CWB is the source of the observed periodicity (van der Walt, 2011), a simple binary model can be developed to find the properties of the binary star systems corresponding to the observed period limits of 29.4 and 511.0 days. Kepler's Third law for two bodies orbiting around their barycenter can be summarised

mathematically as

$$M_A + M_B = \frac{d^3}{P^2}, \tag{6.4}$$

where M_A and M_B are the masses of the primary and secondary bodies, both measured in solar masses ($M_\odot$), d is the separation distance in Astronomical Units (AU) and P is the orbital period in years. From equation 6.4, the separation distance of the two bodies orbiting each other can be determined provided the period and their masses are known.

Since early B-type (B2) stars are the lower mass limit to produce Lyman continuum photons which can have enough energy to form UCHII, they should be the lower mass limit for the protostars which are associated with methanol masers (Walsh et al., 1997). Using data from Panagia (1973) table and $L = M^{3.2}$ adopted from De Loore & Doom (1992), where L and M are the luminosity and mass for a hydrogen-burning ZAMS respectively, the B2-type hydrogen-burning ZAMS mass will be 12 $M_\odot$, which was rounded to 10 $M_\odot$ for modelling purposes. It is important to note that ZAMS stars are more developed.

Using the shortest and longest periods listed in Table 6.1, namely 29.4 days for G12.89+0.49 and 511.0 days for G331.13-0.24, the separation distance was determined for a 10 $M_\odot$ primary object and a 8.00, 4.00, 1.00, and 9.49×10^{-4} $M_\odot$ secondary object. The mass of 9.49×10^{-4} $M_\odot$ is equal to Jupiter's mass so that would be a Jupiter-like planet moving around a 10 $M_\odot$ protostar. The results are shown in Table 6.4 (also see Figure 6.2).

Since Equation 6.4 takes the primary and secondary bodies as a point mass, we want to determine whether the secondary body will be either inside, outside, or

overlapping with the primary object. Hosokawa et al. (2010) gives a model which details the four phases of a protostar evolution. Some of the core arguments in the model were high accretion rate ($\dot{M} > 10^{-4}$ $M_{\odot}yr^{-1}$) and spherically symmetric accretion. For a 10 $M_{\odot}$ protostar, the stellar radius reaches maxima of 30-400 $R_{\odot}$ (0.14 to 1.86 AU). For comparison, Panagia (1973) made calculations for the temperatures, absolute magnitude, luminosities and radii for the Zero-Age Main Sequence (ZAMS), dwarf, giant, and supergiant stars from B3 to O4. The radius determined ranges from 3.4-15.1 $R_{\odot}$ for the ZAMS stars. For our case study, the lower (0.14 AU) and upper (1.86 AU) maximum modelled by Hosokawa et al. (2010) will be used. Palla (2005) presented the result that the possible explanation for the measured effective temperature in Orion KL could be due to a large protostar $\sim$ 300 $R_{\odot}$ or a very active inner circumstellar accretion disk with a 10 $M_{\odot}$ protostar. Orion KL is a special star forming region but the radius approximated by Palla (2005) falls within the range described by Hosokawa et al. (2010) model. The radius range determined by Panagia (1973) is very small when compared with those determined by Hosokawa et al. (2010) model and Palla (2005), but class II methanol masers are associated with massive Young Stellar Objects (YSOs) which occur long before the ZAMS stage.

The distance from the center of the primary body to the barycenter (d_1) of the system can be determined from

$$d_1 = \left(1 - \frac{M_A}{M_A + M_B}\right) d, \tag{6.5}$$

where $d = d_1 + d_2$ is the separation distance. Equation 6.5 depends on the masses of the primary and secondary objects in a binary star system, and is for a circular

Period	29.4 days	511.0 days
M_B ($M_\odot$)	d (AU)	d (AU)
8.00	0.49	3.27
4.00	0.45	3.01
1.00	0.41	2.78
9.49×10^{-4}	0.40	2.69

Table 6.4: Possible binary system properties (mass and separation distance) with a 10 $M_\odot$ primary star. The first column gives the mass of secondary objects. The second column gives the separation distance for a 29.4 day period and the last column gives the separation distance for a 511.0 day period.

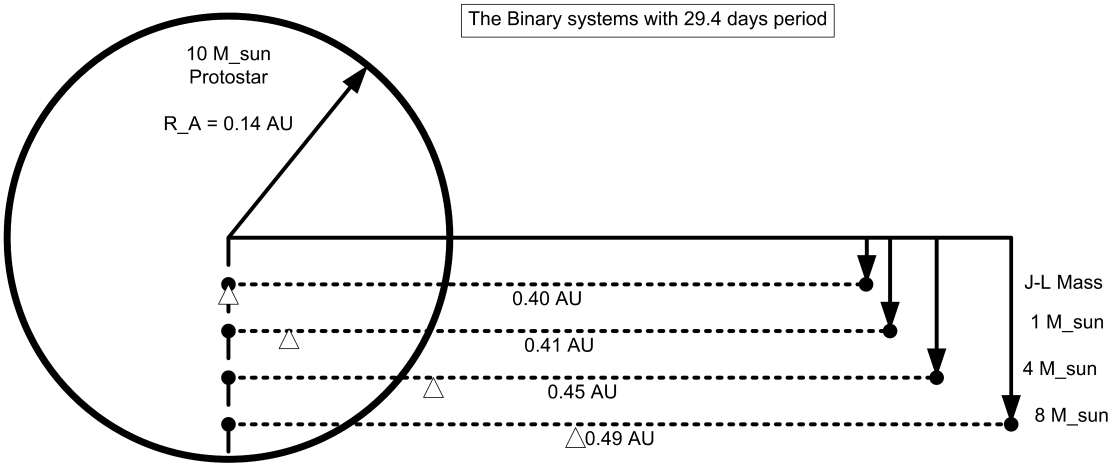

Figure 6.2: Our 29.4 day period binary system models - with a 10 $M_\odot$ (0.14 AU radius) protostar as a primary object and the secondary objects were: Jupiter-like (J-L) mass, 1 $M_\odot$, 4 $M_\odot$ and 8 $M_\odot$. The separation distances are given in Astronomical Units (AU). The Δ shows the location of the center of rotation or the center of mass.

orbit which contradicts the CWB model. If the center of rotation or center of mass of a circular binary system is inside the primary object, then it is possible to have a contact binary. The radius of the binary companion will be less than or equal to ($\leq$) $d - r_A$. If the center of rotation is outside the primary object, then the barycenter will be inside a secondary object in a contact binary. This implies that the radius of the binary companion will be less than ($<$) $d - d_1$ which is the same as or less than the distance from the center of rotation to the center of secondary object (d_2).

As discussed above, a protostar has a very large radius compared with a developed star. This means that the existence of a binary system will depend on the size of the primary (protostar) and secondary (protostar or protoplanet) objects.

Period M_B ($M_\odot$)	29.4 days r_B (AU)	Mean density $\sim M/R^3$ ($M_\odot.{R_\odot}^{-3}$)	511.0 days r_B (AU)	Mean density $\sim M/R^3$ ($M_\odot.{R_\odot}^{-3}$)
8.00	0.35	1.88×10^{-5}	3.12	2.60×10^{-8}
4.00	0.31	1.35×10^{-5}	2.86	1.70×10^{-8}
1.00	0.27	5.06×10^{-6}	2.64	5.00×10^{-9}
9.49×10^{-4}	0.26	5.00×10^{-9}	2.53	5.89×10^{-12}

Table 6.5: The absolute upper limit radius for the binary companions for a 10 $M_\odot$ protostar. The radius of a protostar is set to be 0.14 AU (30 $R_\odot$) and the periods of the binary systems are 29.4 and 511.0 days. The center mass of rotation was ignored in determining the radius of the secondary object (r_B), so r_B was determined from the difference between the separation distance (d) and the radius of the primary object r_A ($r_B = d - r_A$).

In summary, our case study uses a protostar (primary object) 10 $M_\odot$ with a 0.14 AU (30 $R_\odot$) radius, which will have a mean density of 3.66×10^{-4} $M_\odot.{R_\odot}^{-3}$. The second case will also use a protostar (primary object) 10 $M_\odot$, but with a 1.86 AU (400 $R_\odot$) radius and a mean density of 1.56×10^{-7} $M_\odot.{R_\odot}^{-3}$.

For a 29.4 day period, d_1 ranges between 3.80×10^{-5} - 0.22 AU. If the protostar radius is 0.14 AU, then the center of rotation (center mass) for a Jupiter-like mass, 1 and 4 $M_\odot$ binary companion will lie inside the protostar. The mean density of

the protostar is 3.66×10^{-4} $M_\odot.{R_\odot}^{-3}$ and the mean densities in Table 6.5 are even smaller. For a 8 $M_\odot$ binary companion, the radius must be less than 0.27 AU because the center of rotation lies outside the protostar. The new minimum mean density for a 8 $M_\odot$ binary companion with 0.27 AU radius will be 4.08×10^{-5} $M_\odot.{R_\odot}^{-3}$. The radius of the binary companions can still be decreased to avoid contact, so these are possible binary systems. The size and approximated mean density constraints for the binary companions are given in Table 6.5. If the protostar radius is 1.86 AU, all the binary companions will be inside the protostar, which is impossible.

M_B ($M_\odot$)	r_B (AU)	$\sim M/R^3$ ($M_\odot.{R_\odot}^{-3}$)
8.00	1.44	2.69×10^{-7}
4.00	1.18	2.43×10^{-7}
1.00	0.95	1.17×10^{-7}
9.49×10^{-4}	0.85	1.56×10^{-10}

Table 6.6: The absolute upper limit radius for the binary companions of a 10 $M_\odot$ protostar. The radius of a protostar is set to be 1.86 AU (400 $R_\odot$) and the period of the binary system is 511.0 days.

For a 511.0 day period binary, d_1 ranges between 2.55×10^{-4} - 1.45 AU. If the protostar has 1.86 AU radius, the center of rotation lies inside the protostar. The size of the binary companion is also important. If it is not considered, then the orbiting bodies may be in contact or overlapping with each other. The size and approximate mean density constraints for the binary companions are shown in Table 6.6. All binary companions are denser than the primary object except for a Jupiter-like object, so only Jupiter-like objects can be in a binary system. If the protostar has a 0.14 AU radius (3.66×10^{-4} $M_\odot.{R_\odot}^{-3}$ mean density), then all binary companions in our model are very probable. The size and approximated mean density constraints for the binary companions are shown in Table 6.5.

Since the model suggests that a binary system is possible with some constraints, would the binary companion lie inside, outside or surrounded by the the accretion disk? If it is surrounded by the accretion disk, how is the mass flow from the accretion disk to the binary system distributed to the primary and secondary objects? From the observations, M. J. McCaughrean and C. R. O'Dell (1996) found the diameter of a circumstellar accretion disk to be between 50-1000 AU. Machida et al. (2005) did the modelling, where the size of the circumstellar accretion disk was restricted to $\sim$ 10 AU during the main accretion phase. As the main accretion phase evolves, the diameter increased to $\gtrsim$ 100 AU, based on the given size range of a circumstellar accretion disk. Since the largest separation distance in our simple model is 3.27 AU, it suggests that the binary companion would be in the inner accretion disk or that the binary system is surrounded by the accretion disk.

6.2.3 Waveforms of periodic or quasi-periodic sources

The periodic and quasi-periodic methanol maser sources have various waveforms (Figure 6.3). The waveforms in Figure 6.3 resemble simple derivations of sinusoids. This hypothesis was tested and the results are shown in Figures 6.5 to 6.9. For the G338.93-0.06 time series, an absolute cosine function ($f(x) = |\cos(\omega x + \phi)|$) was used. For the G9.62+0.20E time series, an absolute sine function ($f(x) = |\sin(\omega x + \phi)|$) was used. The fits were done with Python script which uses the module called optimize.leastsq(). The fits were good except for G9.62+0.20E, due to its steep rise and decay near local maxima. The G9.62+0.20E waveforms are not symmetric which also contributes to the offset in the fit.

Since there is more than one type of periodic waveform observed (Figure 6.3),

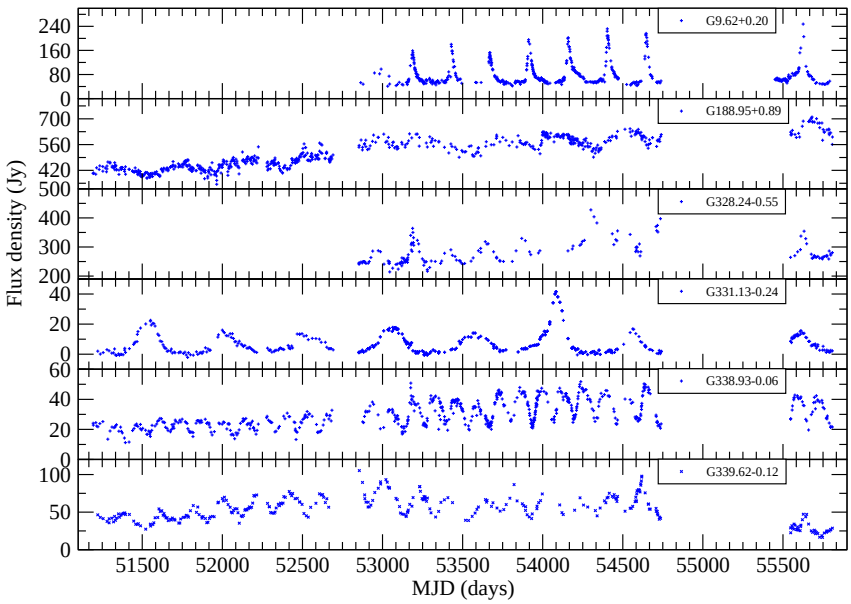

Figure 6.3: Comparison of waveforms for periodic and quasi-periodic methanol maser sources.

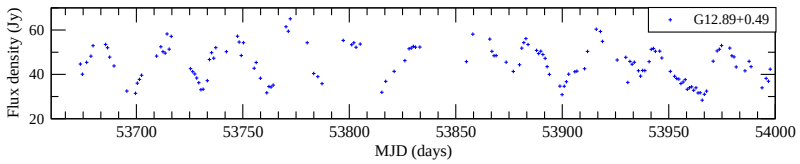

Figure 6.4: G12.89+0.49 waveform.

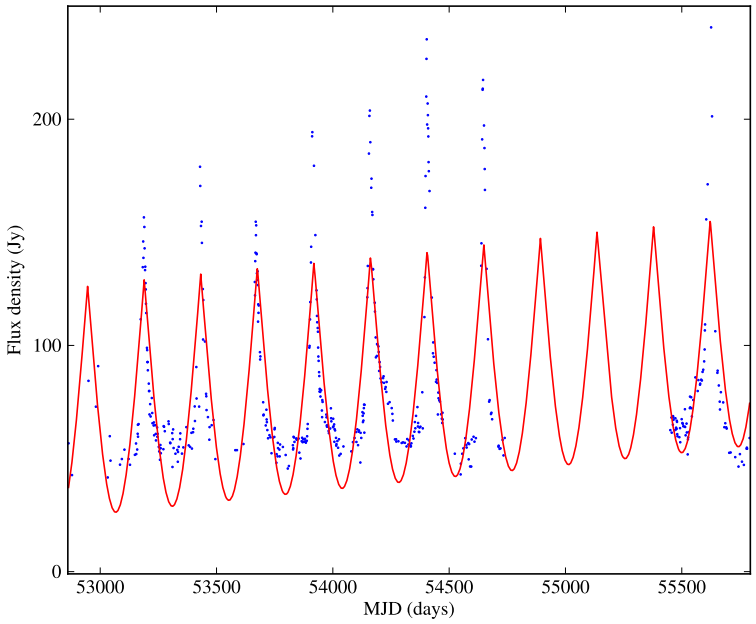

Figure 6.5: A negative absolute sine function fitted to the waveform of the G9.62+0.20E time series at 12178 MHz.

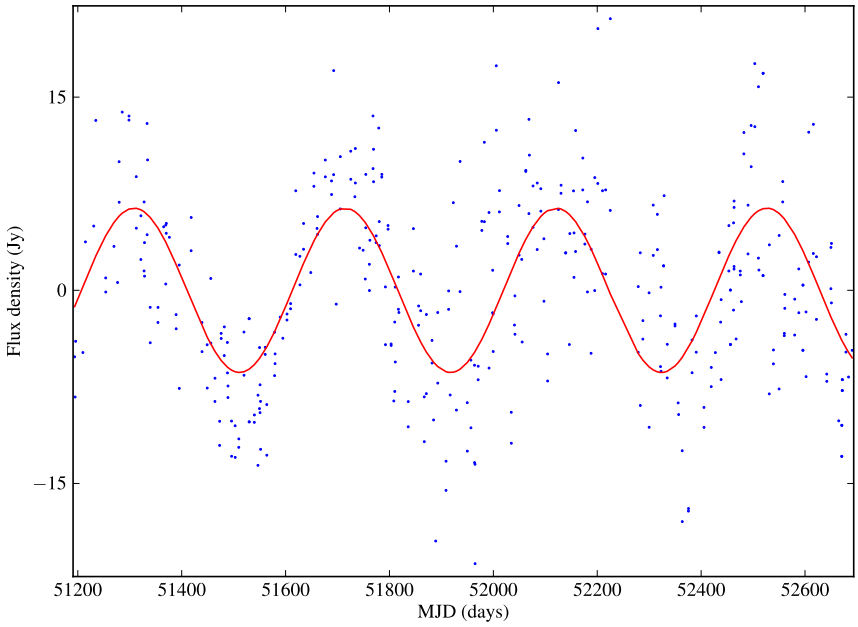

Figure 6.6: A sine function fitted to the waveform of the G188.95+0.89 time series at 6668 MHz.

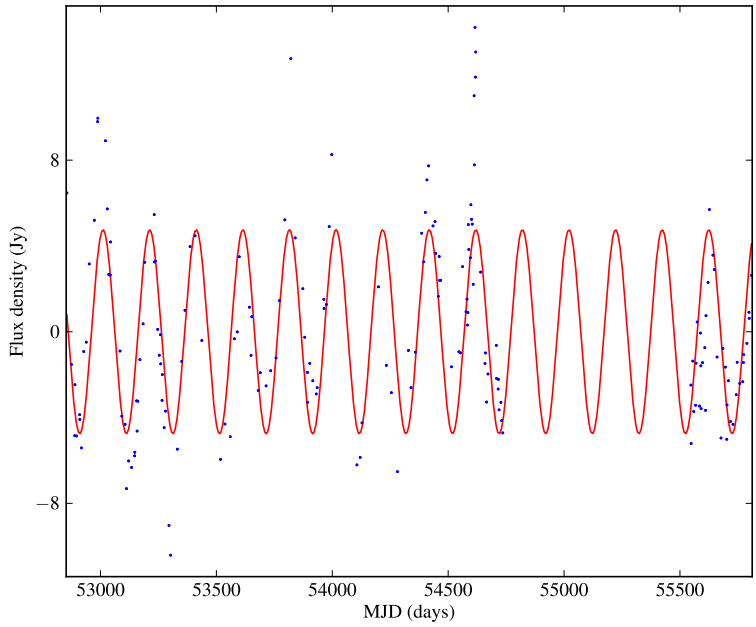

Figure 6.7: A sine function fitted to the waveform of the G339.62-0.12 time series at 6668 MHz.

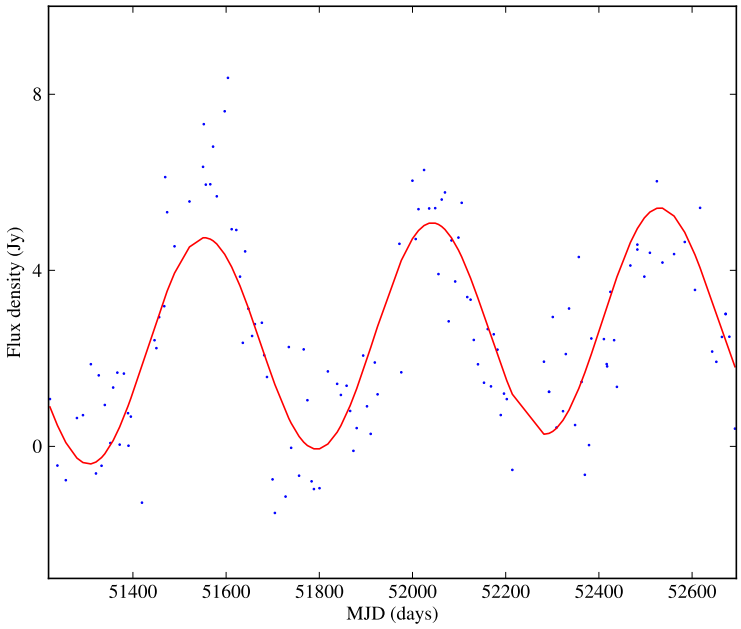

Figure 6.8: A sine function fitted to the waveform of the G331.13-0.24 time series at 6668 MHz.

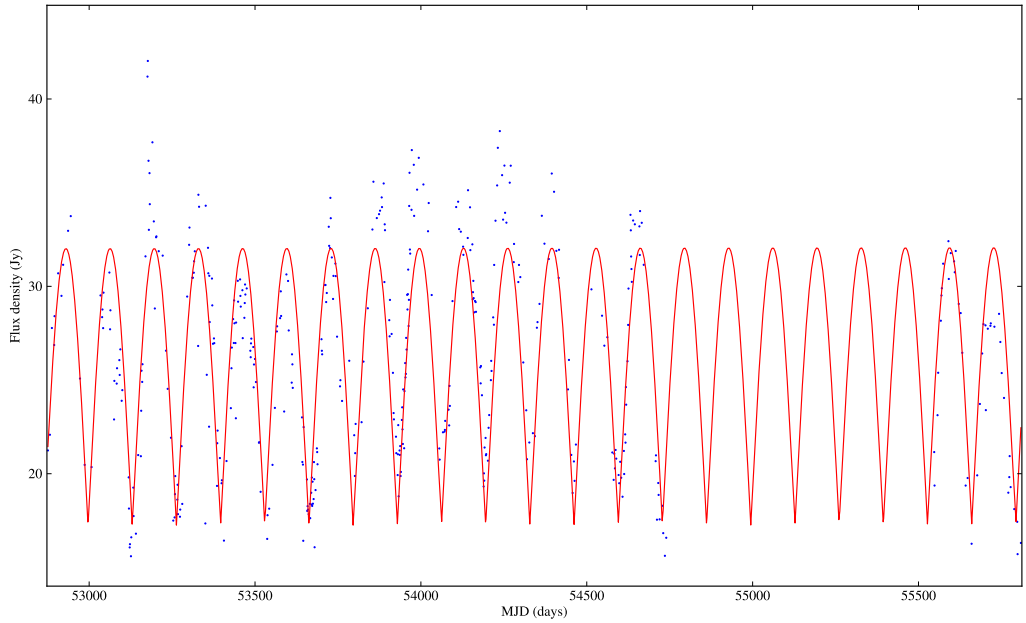

Figure 6.9: An absolute cosine function fitted to the waveform of the G338.93-0.06 time series at 6668 MHz.

there could be more to be observed - which suggest a diversity of star forming environments. Could these diverse waveforms be due to different orientations with respect to an observer? This has been observed in Active Galactic Nuclei (AGN) and quasars (Antonucci, 1993). If the surroundings of a masing cloud (or masing cloud) were changed, how would a waveform evolve?

6.3 New methanol maser sources

From the 6668-MHz Methanol Multi-Beam maser (MMB) catalogues I and II, seven new methanol maser source regions which had never been monitored before were selected for monitoring based on their emission strength. Two sources (G8.872-

0.493 and G358.460-0.391 at 6668-MHz) were found to be variable.

The Lomb-Scargle method was used to search for and test the significance of the periodicity in their time series. The period determined for G8.872-0.493 was 76 days and G358.460-0.391 has a 187-day period. The number of cycles are not sufficient to conclude whether these time series are periodic or not. However, it is certain that they are variable sources. To confirm the kind of variability, long-term monitoring is required.

Even though the search was negative for the other sources over our monitoring period, the monitoring should continue since these regions are active and evolving. Monitoring them may help to find the processes which can initiate variability, even if they were not variable over our monitoring window. Monitoring these regions for a longer period could give us enough data to see whether it is a variable source. Determining a lower limit for monitoring a source is harder as seen in the G351.78-0.54 time series (Figure 5.10) which was flat from February to September 2011. If it was observed for that period only, one could have thought that it was not variable.

6.4 Irregularly varying methanol maser sources

G351.42+0.64 shows weak variations at both 6668 MHz (Figure 5.2) and 12178 MHz (Figure 5.7). The weaker peaks show two flares.

The variations in G351.78-0.54 at 6668-MHz appear to be random and there is no simple pattern which they follow. The time series for each of the four spatially distinct maser regions (A, B, C and D in Figure 5.12, Norris et al. (1993)) were divided by each maximum. The resulting normalised time series are shown in Figure

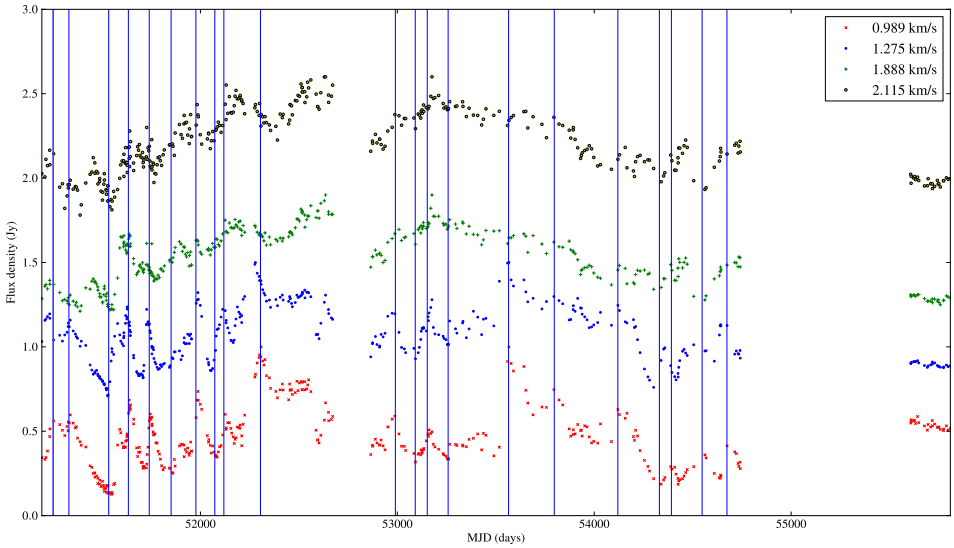

Figure 6.10: Normalised time series for G351.78-0.54 at 6668-MHz. The vertical lines show time delays in the time series. The 0.989 km.s^{-1} time series was used to provide the reference markers for maximum and minimum.

6.10. The D (0.989 km.s^{-1}) and C (1.275 km.s^{-1}) spots are strongly correlated, and they show peaks with small width. The B (1.888 km.s^{-1}) and A (2.115 km.s^{-1}) spots are strongly correlated, with wider peaks. Around 53550 MJD, spots D and C show a significant jump that is not observed in the time series for the B and A maser spots. The long-term variations are correlated to all time series suggesting a common source.

By drawing vertical lines at some of the local maxima and minima in the normalised time series, we show that sometimes there are time delays in the local maxima and minima of the time series at 0.989 and 1.275 km.s^{-1} (D and C, respectively). For example, around 51720 and 52265 MJD there are clear time delays between 0.989 and 1.275 km.s^{-1} time series. This behaviour suggests possible movements in either the masing environments or the background radiation. This was also noted by Macleod & Gaylard (1996). The B and A maser spots show no clearly

visible time delays yet they are not in the same position.

we show that the local maxima and minima of the 0.989 and 1.275 km.s^{-1} (D and C) time series (Figure 6.10)

The A, B maser spot time series and C, D maser spot time series are correlated in their long-term variations. The short-term variations sometimes show correlations. For an example, at around 51534, 51781 and 52426 MJD there are local minima for all time series (Figure 6.10). The waveforms of the A, B maser spots and the C, D maser spots are significantly different. There are clear correlations in some of the activities suggesting that some things are common to these maser spots. Macleod & Gaylard (1996) concluded that these two maser spot groups are not correlated. The variation range of the C, D maser spots make it hard to see the short-term activities in their time series.

During star-formation, jets are formed at irregular intervals (Burrows et al., 1996), and the interaction between the magnetosphere of a rotating protostellar object and a circumstellar accretion disk drives the collimated outflow (Matt et al., 2002). This could be the possible explanation of the episodic variations in G351.78-0.54.

Flaherty & Muzerolle (2010) modelled the mid-infrared variability of a circumstellar disk with non-axisymmetric structure and concluded that inner disk changes could be the source of mid-infrared variations. Variations in the dust temperature could result in the observed variations (Sobolev et al., 2007).

6.5 long-term variability

Most of the time series show long-term variations. In some of the time series, the long-term increases in intensity are well fitted by first-order polynomials. The sources which show clear long-term linear growth are: G9.62+0.20E, G188.95+0.89 and G328.24-0.55.

On the other hand, G188.95+0.89 and G339.62-0.12 show long-term decays which can be well fitted by exponential functions. The e-folding times for each time series are given in Table 6.7. This behaviour was first noticed by van der Walt (2011). It is thought to be due to recombination of ionised gas around the masing region (van der Walt, 2011).

Vel. ($km.s^{-1}$)	Freq. (MHz)	e-folding time (days)
10.192 (G188.95+0.89)	12178	1515
11.394 (G188.95+0.89)	12178	1064
11.404 (G188.95+0.89)	6668	1271
-33.533 (G339.62-0.12)	6668	1030

Table 6.7: G188.95+0.89 and G339.62-0.12 e-folding time.

The trends in the time series could characterise the changing local environment of the maser and the other variations such as episodic, periodic and quasi-periodic variations could be due to background radiation.

6.6 Flaring behaviour

Some of the methanol sources in our monitoring program showed a flare or flares. G9.62+0.20E had periodic flares in some of its time series at both 6668 MHz and

12178 MHz (Figures 5.14 and 5.18). The selected flare in Figure 6.11 ranges from 55500 to 55800 MJD. The other non-periodic flare sources are shown in Table 6.8.

Source	Freq. (MHz)	Time range (MJD)	Duration (days)
G188.95+0.89	6668	53960-54000	40
G328.24-0.55	6668	53100-53300	200
G338.93-0.06	6668	53100-53300	200
G328.24-0.55	12178	53700-53930	230
G331.13-0.24	6668	53900-54300	400
G339.62-0.12	6668	51670-52200	530

Table 6.8: Some of the methanol maser sources which had flares in their time series.

The flares for all methanol maser sources in the sample are compared in Figure 6.11. For most flares, the rate of increase to the local maximum is greater than the decay rate. These rates characterise the observed shape. The longest flare occurred for about 530 days in G339.62-0.12. This source had a slow rise compared to its decay rate (Figure 6.11). The flare in G188.95+0.89 is the shortest and it lasted for 40 days and is very different to the others (Figure 6.11). It rises very fast but afterwards, it appears to return to its quiescent state.

Fujisawa et al. (2011) explained the observed flare in G33.64-0.21 as an impulsive energy release. It can be used to explain the flares observed in some of our sources. The flares are common in all kinds of methanol maser variability (weak or strong, regular or irregular). This fits well with the massive star formation theory because they are evolving energetic young stellar objects, and energy burst activities are more likely to occur.

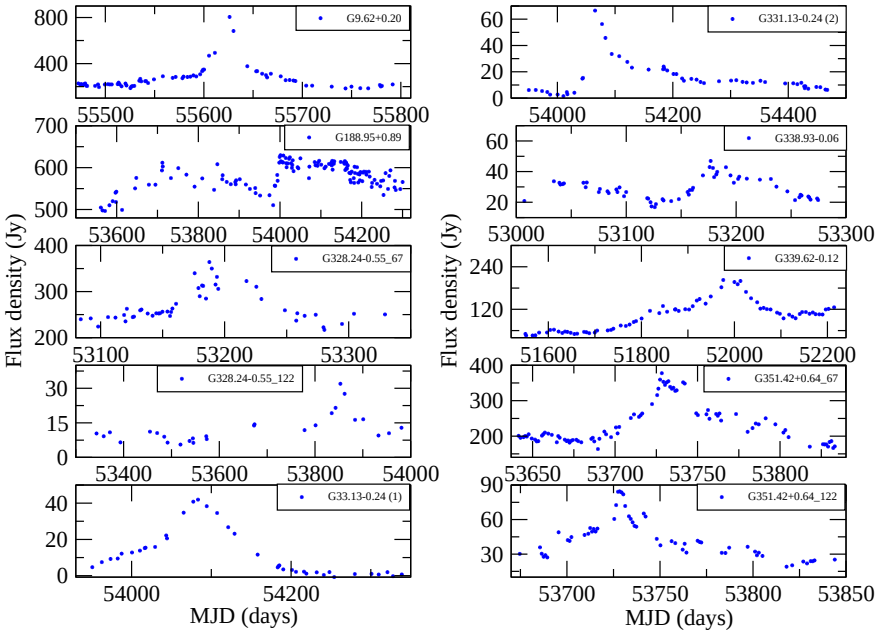

Figure 6.11: Some of the flares in the methanol maser source sample.

6.7 Some unresolved questions

In general, observed variability argues against originating within individual maser clouds or caused by background environments. Some of the methanol maser sources have been observed to show similar behaviour in different masing clouds, suggesting a common origin for the variability. This argument falsifies the maser spots as the source of the observed variability. It could be background sources or the environment surrounding the masers.

Why are class II methanol masers not associated with young low mass protostars or dying stars, etc? This could be due to the way in which methanol is formation in star forming regions. Goumans et al. (2007) proposed that methanol is formed as ice on grain surfaces, then change directly into vapour when heated during star formation (also see Das et al. (2008)). Water vapour masers appear in both low

and high mass star forming regions. One possibility is that methanol masers are formed by a process which only occurs in massive star forming regions - it could be a unique density distribution. Monitoring these maser sources, and new sources, will put better constraints on the maser models.

Chapter 7

Conclusion and future prospects

7.1 Conclusion

The two brightest class II methanol masers (6668-MHz and 12178-MHz emission lines) in massive star forming regions were successfully monitored using the 26-m HartRAO radio telescope. The monitoring programme consisted of one control source, one irregular source, seven known periodic and quasi-periodic sources, and seven new methanol maser sources from the 6668-MHz Methanol Multi-Beam maser (MMB) catalogues I and II.

The two brightest class II methanol masers show aperiodic, quasi-periodic and periodic variability over the monitoring periods.

- G351.42+0.64 at 6668 MHz and 12178 MHz was a control source due to its weak variation range. It shows two flares but it served its purpose to check the consistency of the Point Source Sensitivity (PSS) determined from the calibrators (Hydra A and 3C123).

- In contrast to the known periodic and quasi-periodic source, G351.78-0.54 shows episodic variations. The long-term variations are strongly correlated in all the peaks. The short-term variations show weak correlation between the

east and west groups of maser peaks. The left maser spot group is strongly correlated and this also applies to the right maser spot group. These two groups are approximately 0.82 megaparsec (Mpc) apart. Time delays between the time series appear, disappear and reappear.

- The seven periodic and quasi-periodic methanol masers are: G12.89+0.49 (29.40 ± 0.11 day period), G338.93-0.06 (132.8 ± 0.7 day period), G339.62-0.12 (200.6 ± 1.4 day period), G328.24-0.55 (221.4 ± 1.9 day period), G9.62+0.20E (243.5 ± 1.2 day period), G188.95+0.89 (389.4 ± 4.2 day period), and G331.13-0.24 (511.0 ± 7.6 day period). Their periods range from 29.4 to 511.0 days. G188.95+0.89 and G331.13-0.24 are quasi-periodic sources and the rest are periodic.

- The flares are common and they appear to be independent of the type of variability (weakly varying, episodic, periodic and quasi-periodic) in the source. From the sample of eight sources excluding irregular varying source, seven had at least flare over a thirteen-year period.

- The long-term variations are also common to the weakly varying, episodic, periodic, and quasi-periodic sources. Some of the sources show a decay which can be fitted by an exponential function. Maser peaks can be created and destroyed as observed in the G328.24-0.55 6668 MHz spectra.

- Two new sources were found to be variable and they are possible new candidates for the periodic or quasi-periodic family. These sources are G8.872-0.493 (76 day period) and G358.460-0.391 (187 day period) at 6668-MHz.

- The source of the observed regular variations is not yet understood.

7.2 Future prospects

The challenge with current interferometry is a detailed resolution of these compact massive star forming regions. However, the Square Kilometer Array (SKA) and African Very Long Baseline Interferometry (VLBI) Network (AVN) combined with other VLBI Networks will be vital in terms of their capabilities in filling up the gaps in the UV plane, and this will give new insights on and detailed images of these compact regions.

It will be important to make high angular resolution interferometry images of the maser spots at the maxima and minima of the regularly varying methanol maser sources. With our current arrays such as the Multi-Element Radio-Linked Interferometer Network (MERLIN), the Very Large Array (VLA), the Australia Telescope Compact Array (ATCA), etc, continuum sources can be monitored at local minima and maxima of periodic or quasi-periodic sources provided such a continuum source exists in the region. This gives information on what the continuum source is doing when the methanol masers are at local minimum and maximum. It also gives information as to whether the continuum sources and the methanol masers are correlated. Observing a continuum source requires very high sensitivity which implies longer integration times on source.

In some of the class II methanol maser emission regions which show periodic behaviour there are water vapour and hydroxyl masers. They should also be monitored to check their behaviour as the methanol masers are regularly varying, even though the water vapour masers are thought to be collisionally pumped (see pp. 262-279: Elitzur, 1992) and are associated with molecular bipolar outflow (Chibueze et al., 2012; Patel et al., 2000). One of the questions to be answered is: what is the corre-

lation between the time series of water vapour masers, hydroxyl masers and known regularly varying methanol masers in massive star forming regions?

The model proposed by Sobolev et al. (2007) shows that it is possible to amplify masers from the varying surroundings of the masers. In contrast, van der Walt (2011) proposed background radiation as the source variability. Both models should be revisited and modified to try to advance the explanation of the source of the variability. Perhaps coupling these models could bring about a complete model of masers or a complete model of the source of the observed variability in these massive star forming regions. The CWB model (see Section 2.6) could be tested by other observations, e.g. water masers; high-resolution continuum and thermal line images from Atacama Large Millimeter Array (ALMA).

Bibliography

Alexander T., 1997, in Astronomical Time Series, Maoz D., Sternberg A., Leibowitz E. M., eds., Vol. 218, Kluwer Academic, Dordrecht, p. 163

Antonucci R., 1993, *ARA&A*, 31, 437

Batrla W., Matthews H. E., Menten K. M., Walmsley C. M., 1987, *Nat*, 326, 49

Blandford R., 1993, in Astrophysical Jets, Burgarella D., Livio M., O'Dea C. P., eds., Cambridge University Press, Cambridge, p. 15

Blandford R. D., McKee C. F., 1982, *ApJ*, 255, 419

Boss A., 1988, *ApJ*, 331, 370

Burrows C. J. et al., 1996, *ApJ*, 473, 437

Caswell J. L., 1997, *MNRAS*, 289, 203

Caswell J. L. et al., 2010, *MNRAS*, 404, 1029

Chibueze J. O., Imai H., Tafoya D., Omodaka T., Kameya O., Hirota T., Chong S., Torrelles J. M., 2012, *ApJ*, 748, 146

Condon J. J., Ransom S. M., 2010, Antenna Fundamentals. Website, `http://www.cv.nrao.edu/course/astr534/AntennaTheory.html`

Cragg D. M., Johns K. P., Godfrey P. D., Brown R. D., 1992, *MNRAS*, 259, 203

Cragg D. M., Sobolev A. M., Godfrey P., 2002, *MNRAS*, 331, 521

Cragg D. M., Sobolev A. M., Godfrey P. D., 2005, *MNRAS*, 360, 533

Das A., Acharyya K. A., Chakrabarti S. K., 2008, *A&A*, 486, 209

Davies S. R., 1990, *MNRAS*, 244, 93

de Buizer J. M., 2000, PhD thesis, Graduate school of the University of Florida, Florida, USA

de Buizer J. M., Pina R. K., Telesco C. M., 2000, *ApJS*, 130, 437

De Cat P., 2001, PhD thesis, Katholieke Universiteit Leuven, Leuven

De Loore C. W. H., Doom C., eds., 1992, Structure and Evolution of Single and Binary Stars. Kluwer Academic, Dordrecht, Netherlands, p. 194

Edelson R. A., Krolik J. H., 1988, *ApJ*, 333, 646

Einstein A., 1917, *Pysikalische Zeitschrift*, 18, 121

Elitzur M., 1992, Astronomical Masers, Vol. 170. Kluwer Academic Inc., Dordrecht, Netherlands, pp. 1–112

Eyer L., Mowlavi N., 2008, *J. Phys.: Conf. Ser*, 118, 012010

Fabian A. C., Pringle J. E., Reese M. J., 1975, *MNRAS*, 175, 15

Fano U., 1985, *Phys. Rev. A*, 32, 617

Fisher R. A., 1921, *Metron*, 1, 1

Flaherty K. M., Muzerolle J., 2010, *ApJ*, 719, 1733

Foot C. J., 2005, Atomic Physics. Oxford University Press, New York, pp. 80–96

Forster J. R., Caswell J. L., 1989, *A&A*, 213, 339

Foster P., 1994, in Clouds, Cores, and Low Mass Stars, Clemens D. P., Barvains R., eds., Vol. 65, *ASP Conf. Ser.*, San Francisco: ASP, p. 105

Frescura F. A. M., Engelbrecht C. A., Frank B. S., 2008, *MNRAS*, 388, 1693

Fujisawa K. et al., 2011, *PASJ*, 1

Garay G., Rodriguez L. F., Moran J. M., Churchwell E., 1993, *ApJ*, 418, 368

Gaskell C. M., Peterson B., 1987, *ApJ*, 65, 1

Gaume R. A., Mutel R. L., 1987, *ApJS*, 65, 193

Gaylard M. J., 2012, HartRAO 26m Radio Telescope Details. Website, `http://www.hartrao.ac.za/factsfile.html`

Goedhart S., Gaylard M. J., van der Walt D. J., 2004, *MNRAS*, 355, 553

Goedhart S., Langa M. C., Gaylard M. J., van der Walt D. J., 2009, *MNRAS*, 398, 995

Goedhart S., Minier V., Gaylard M. J., van der Walt D. J., 2003, *MNRAS*, 356, 839

Goedhart S., Minier V., Gaylard M. J., van der Walt D. J., 2005, *MNRAS*, 356, 839

Goumans T. P. M., Wander A., Catlow C. R. A., Brown W. A., 2007, *MNRAS*, 382, 1829

Green J. A. et al., 2010, *MNRAS*, 409, 913

Harris F. J., 1978, *Proc. IEEE*, 66, 51

Hart J. D., Koen C., Lombard F., 2007, *Journal of the Royal Statistical Society: Series C (Applied Statistics)*, 56, 587

Hines W. W., Montgomery D. C., 1972, Probability and Statistics in Engineering and Management Science. Ronald Press, New York

Hosokawa T., Yorke H. W., Omukai K., 2010, *ApJ*, 721, 478

Karmakar P. K., Sengupta L., Maiti M., Angelis C. F., 2010, *Am. J. Sci. Ind. Res.*, 1(2), 350

Kraus A. L., 2010, PhD thesis, California Institute of Technology, Pasadena, California

Kraus J. D., 1986, Radio Astronomy, 2nd edn. Cygnus-Quasar Book, Powell, Ohio, pp. 7:0–74

Larsson S., 1995, *A&A*, Suppl. Ser. 117, 197

Leahy D. A., Darbo W., Elsner R. F., Weisskopf M. C., Sutherland P. G., Kahn S., Grindlay J. E., 1983, *ApJ*, 266, 160

Lees R. M., Haque S. S., 1974, *Can. J. Phys.*, 52, 2250

Lo K. Y., 2005, *ARAA*, 43, 625

Lomb N. R., 1976, *ApSS*, 39, 447

M. J. McCaughrean and C. R. O'Dell, 1996, *AJ*, 111, 1977

Mac Low M.-M., Klessen R. S., 2004, *Rev. Mod. Phys*, 76, 92

Machida M. N., Matsumoto T., Hanawa T., Tomisaka K., 2005, *MNRAS*, 362, 382

Macleod G. C., Gaylard M. J., 1996, *MNRAS*, 280, 868

Mangum J., 2006, Observing Modes Used in Radio Astronomy, NRAO Technical notes

Matt S., Goodson A. P., Winglee R. M., Bohm K., 2002, *ApJ*, 574, 232

Menten K. L., 1991, *ApJ*, 380, L75

Minier V., Burton M. G., Hill T., Pestalozzi M. R., Purcell C. R., Garay G., J.Walsh A., Longmore S., 2005, *A&A*, 429, 945

Murray N., Quataert E., Thompson T. A., 2010, *ApJ*, 709, 191

Norris R. P., Whiteoak J. B., Caswell J. L., Wieringa M. H., Gough R. G., 1993, *ApJ*, 412, 222

Nunez M., 2006, *J. Phys. A: Math. Gen.*, 39, 6097

Osterbrock D. E., Ferland G. J., eds., 2006, Astrophysics of Gaseous Nabulae and Active Galactic Nuclei. University Science Books

Ott M., Witzel A., Quirrenbach A., Krichbaum T. P., Standke K. J., Schalinski C. J., Hummel C. A., 1994, *A&A*, 284, 331

Palla F., 2005, in Massive Star Birth: A Crossroads of Astrophysics, Cesaroni R., Felli M., Churchwell E., Walmsley M., eds., Cambridge University Press, Cambridge, p. 196

Panagia N., 1973, *ApJ*, 78, 9

Patel N. A., Greenhill L. J., Herrnstein J., Zhang Q., Moran J. M., Ho P. T. P., Goldsmith P. F., 2000, *ApJ*, 538, 268

Phillips C. J., Norris R. P., Ellingsen S. P., McCulloch P. M., 1998, *MNRAS*, 300, 1131

Pottage J. T., Flower D. R., Davis S. L., 2001, *J. Phys. B*, 34, 3313

Pottage J. T., Flower D. R., Davis S. L., 2002, *J. Phys. B*, 35, 2541

Pottage J. T., Flower D. R., Davis S. L., 2004a, *J. Phys. B*, 37, 165

Pottage J. T., Flower D. R., Davis S. L., 2004b, *MNRAS*, 352, 39

Press W. H., Rybicki G. B., 1989, *ApJ*, 338, 277

Press W. H., Teukolsky S. A., 1977, *ApJ*, 213, 283

Prialnik D., 2000, An Introduction to the Theory of Stellar Structure and Evolution. Cambridge University Press, New York, pp. 1–245

Pudritz R. E., 2002, *Science*, 295, 68

Ramsay G., Napiwotzki R., Barclay T., P.Hakala, Potter S., Cropper M., 2011, *MNRAS*, 417, 400

Rybicki G. B., Lightman A. P., eds., 2004, Radiative Processes in Astrophysics. University Science Books

Scargle J. D., 1982, *ApJ*, 263, 835

Schwarzenberg-Czerny A., 1998, *MNRAS*, 301, 831

Shu F., 1982, The Physical Universe: An Introduction to Astronomy. University Science Books, California, pp. 225–285

Shu F. H., 1992, The Physics of Astrophysics Volume II: Gas Dynamics, Vol. 2. University Science Books, Mill Valley, California, pp. 241–251

Shu F. H., Adams F. C., Lizano S., 1987, *ARAA*, 25, 23

Sinclair M. W., Gough R. G., 1991, *IREECON'91, International Proceedings*, 381

Sobolev A. M. et al., 2007, in Astrophysical Masers and their Environments, Vazdekis A., Peletier R., eds., Cambridge University Press, Cambridge, p. 81

Stahler S. W., Palla F., 2004, The Formation od Stars. Wiley-VCH, Weinheim, pp. 701–707

Stellingwerf R. F., 1978, *ApJ*, 224, 953

Szymczak M., Wolak P., Bartkiewicz A., van Langevelde H. J., 2011, *A&A*, 531, L3

Taylor J. R., 1997, An Introduction To Error Analysis: The Study Of Uncertainties In Physical Measurements, 2nd edn. University Science Books, Sausalito CA94965, USA, pp. 45–92

ter Haar D., 1967, The Old Quantum Theory. Pergamon Press, Elmsford, New York, p. 167

van der Walt D. J., 2011, *A&A*, 141, 152

Vaníček P., 1971, *ApSS*, 12, 10

Walsh A. J., Burton M. G., Hyland A. R., Robinson G., 1998, *MNRAS*, 301, 640

Walsh A. J., Hyland A. R., Robinson G., Burton M. G., 1997, *MNRAS*, 291, 261

Woodward P. R., 1953, *ApJ*, 118, 513

Xu Y., Moscadelli L., Reid M. J., Menten K. M., Zhang B., Zheng X. W., Brunthaler A., 2011, *ApJ*, 733, 25

Xu Y., Voronkov M. A., Pandian J. D., Li J. J., Sobolev A. M., Brunthaler A., Ritter B., Menten K. M., 2009, *A&A*, 507, 1117

Zinnecker H., Yorke H. W., 2007, *ARAA*, 45, 481